TUDelft

Delft University of Technology

Snooping on cells in worms and mini-organs

Huelsz Prince, Guizela

DOI

Publication date
2019

Document Version
Final published version

Citation (APA)

Important note
To cite this publication, please use the final published version (if applicable).
Please check the document version above.

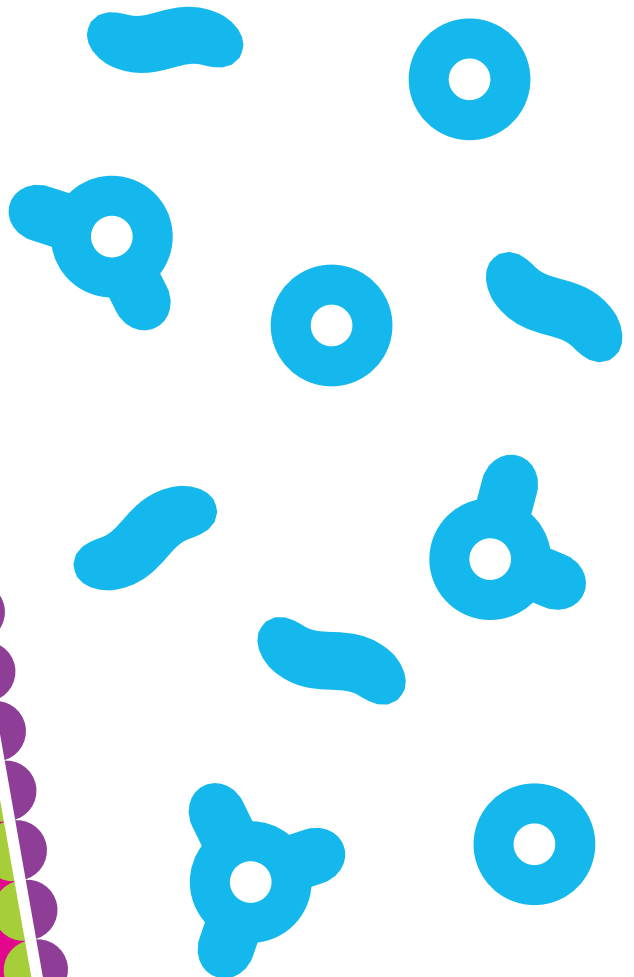# Snooping on cells in worms and mini-organs

Guizela Huelsz Prince

Snooping on cells in worms and mini-organs

Guizela HUELSZ PRINCE

Snooping on cells in worms and mini-organs

Dissertation

for the purpose of obtaining the degree of doctor
at Delft University of Technology
by the authority of the Rector Magnificus prof.dr.ir. T.H.J.J. van der Hagen
chair of the Board for Doctorates
to be defended publicly on
Monday 14 October 2019 at 15:00 o'clock

by

Guizela HUELSZ PRINCE

Master of Science in Physics of Life and Health
University of Amsterdam, The Netherlands
born in Mexico City, Mexico

This dissertation has been approved by the promotors.

An electronic version of this dissertation is available at `http://www.amolf.nl/` and at `http://repository.tudelft.nl/`.

Table of contents

1

General introduction

Throughout their lifetime, animals face enormous and numerous biological challenges. The very first of these challenges is development: becoming a fully grown and functional adult from just a single, tiny cell. This process requires millions of timely planned cell divisions and cell differentiation events that are crucial for the organism to develop correctly. But becoming an adult is not enough; animals need to remain being functional adults for long enough in order to reproduce and to raise their offspring. Even though this might not seem quite as impressive as the millions of cells that need to be created during development, maintaining a functional adult comes with its own set of challenges. Animals often have to fight off disease, their tissues have to be repaired after injuries, and many of their cells have to be constantly renewed due to the wear and tear that result from performing their daily functions.

The mechanisms that animals use to face and overcome these challenges have been the topic of biological and medical research for centuries; yet, we are still far from uncovering many of them. We do have some clues, though, about essential aspects of these mechanisms. Decades of studies, performed using mostly model systems, have revealed plenty of information about the inner workings of cells as well as the ways in which cells communicate with each other. However, biology is often complex, with many coupled intra- and inter-cellular processes occurring at once, making it extremely difficult to understand even small multicellular systems as a whole, let alone understand a complete organism.

In this thesis, we aim to uncover a few examples of how animals cope with some biological challenges. In the first part, we begin by tackling development, with a particular focus on how *C. elegans* nematodes are able

1

to become relatively identical adults despite the huge variability in the conditions that they can encounter during their journey through development (Chapter 3). In the second part, we turn our interest to how adult tissues deal with disease and how they are able to renew and maintain homeostasis. For this purpose, we make use of a recently developed technology which allows the in vitro culture of organoids: three-dimensional, multicellular arrangements that resemble and recapitulate essential features of organs. In particular, we will study how human airway organoids respond to infection by the respiratory syncytial virus (Chapter 5), as well as how murine intestinal organoids react to storage under hypothermic conditions (Chapter 6), and how their cells behave as they grow and mature (Chapter 7).

Even though the topics in this thesis vary widely, the approaches that we use for their study have many similarities. In particular, in Chapters 3, 5 and 7, we use three different systems to study three very different questions; yet, in all cases, it was a combination of quantitative measurements of single-cell dynamics and mathematical/computational modeling that allowed a novel perspective on the questions, and therefore yielded novel results.

Part I

C. elegans as a model system for development

2

Introduction

The nematode *Caenorhabditis elegans* (Figure 2.1) is a tiny, 1.5mm-long roundworm that has become an important model system in many fields within biology since its introduction by Sydney Brenner in the 1970s as the ideal organism to study animal development and behavior [1, 2]. These animals possess numerous desirable traits that make them easily amenable to experimentation. They can be easily cultivated in the laboratory, they have a rapid, three-day life cycle, they can self-fertilize to produce approximately 300 offspring, and they are completely transparent from embryogenesis to adulthood [2, 3]. This latter quality has made *C. elegans* a particularly interesting model organism for the study of animal development.

Figure 2.1 Adult hermaphrodite *C. elegans* and two eggs.
Image taken from [4].

C. elegans transparency allows individual cells within their body to be observed by simple microscopy techniques, and thus, researchers have been

able to track every cell throughout their development and to reconstruct their entire cell lineage, from zygote to adult, since the 1980s [3, 5]. This led to the remarkable finding that every worm develops by following mostly identical patterns of cell division and differentiation, resulting in all adults containing exactly the same types and numbers of somatic cells [4].

The strikingness of such an invariant developmental pattern has been further highlighted by more recent findings showing that even genetically identical cells are inherently variable at the molecular level due to the stochastic nature of gene expression [6]. Many efforts have been made in an attempt to understand how every worm follows such a stereotypical journey through development despite intrinsic variability, from the first division after fertilization [7] to organogenesis during the late larval stages [8]. In the next chapter, we present our contribution to these efforts by suggesting a mechanism through which a component of the *C. elegans* reproductive system – the vulva – develops in an extraordinarily reproducible manner.

3

Canalization of *C. elegans* vulva induction against anatomical variability

It is a fundamental open question how embryos develop into complex adult organisms with astounding reproducibility, particularly since cells are inherently variable on the molecular level. During C. elegans vulva induction, the anchor cell induces cell fate in the vulva precursor cells in a distance-dependent manner. Surprisingly, we found that initial anchor cell position was highly variable and caused variability in cell fate induction. However, we observed that vulva induction was canalized, i.e. the variability in anchor cell position and cell fate was progressively reduced, resulting in an invariant spatial pattern of cell fates at the end of induction. To understand the mechanism of canalization, we quantified induction dynamics as a function of anchor cell position during the canalization process. Our experiments, combined with mathematical modeling, showed that canalization required a specific combination of long-range induction, lateral inhibition and cell migration that is also found in other developmental systems.

3.1 Introduction

In a developing embryo, each cell has to assume the correct cell fate in order to give rise to a viable adult organism. Embryonic development is highly reproducible on the organismal level, as is evident in the strikingly similar appearance of identical twins. Yet, it has become clear that many fundamental biological processes, such as gene expression and cell signaling, are stochastic, causing significant variability between otherwise identical cells [6]. How highly complex bodies can be built in such a robust manner (i.e., without errors) out of cells that individually show strong intrinsic variability is a fundamental and unresolved question.

An important concept to explain the robustness of development is canalization [9, 10]. Whereas there exist many ways in which biological systems exhibit robustness [11], canalization refers to a specific form of robustness, namely to variability in initial conditions. In this picture, canalization is an active mechanism that causes a decrease in the variability of developmental processes as development progresses, thereby ensuring an identical outcome despite initial variation between individuals. This decrease in variability over time is thought to be due to the action of the gene regulatory networks that underlie development [10, 12, 13]. However, it is an open question whether variability in initial conditions is indeed a strong source of variability in developmental systems and, hence, to what extent canalization is responsible for the exceeding robustness of development. Moreover, due to the limited number of systems where canalization has been studied on the molecular level [14–16], it is not known what molecular and cellular mechanisms give rise to it.

A prime example of a robust developmental process is vulva induction in the nematode *C. elegans* [8]. The *C. elegans* vulva forms from a row of vulva precursor cells (VPCs), labeled P3.p – P8.p. During vulva induction, a specific spatial pattern of cell fates, distinguishable by lineage, is induced in a manner that depends only on the relative distance of each VPC to the anchor cell (AC) (Figure 3.1A): P6.p, the cell adjacent to the AC, assumes 1°fate, the more distant P5.p and P7.p cells assume 2°fate, and the remaining P3.p, P4.p, and P8.p cells assume 3°fate. The resulting cell fate pattern is extremely robust. Under standard laboratory conditions, < 1% of animals show minor deviations [17, 18]. Such deviations include centering shifts, in which the correct 2°– 1°– 2°pattern is still induced and results in a functional vulva, but with 1°assumed by either P5.p or P7.p

rather than P6.p. How this observed robustness of the vulva cell fate pattern arises is much-studied but not yet understood [19].

The signaling network that controls VPC fate induction is well characterized, making it uniquely suited to study the molecular mechanisms underlying its robustness [8]. VPC fate is determined by a LIN-3/epidermal growth factor (EGF) signal produced by the AC, in combination with Notch signaling between neighboring VPCs. It is thought that LIN-3/EGF forms a long-range spatial gradient and induces Ras signaling in VPCs in a graded manner, with Ras activation being strongest in P6.p and weaker in the neighboring P5.p and P7.p cells [20, 21]. These activate Notch receptors in neighboring VPCs, causing an inhibition of Ras signaling. Hence, P6.p, the VPC that receives the strongest EFG input, will come to fully inhibit the response to EGF in P5.p and P7.p. As a result, the EGF gradient is amplified into an all-or-none difference in cell signaling and cell fate between VPCs, with high Ras activity in P6.p (1°fate) and high Notch activity in P5.p and P7.p (2°fate).

In this model, the position of the AC is crucial for the establishment of the VPC fate pattern: it is thought that P6.p assumes 1°fate and induces 2°fate in P5.p and P7.p because it is located directly adjacent to the AC. Surprisingly, we found that at the start of vulva induction the position of the AC relative to the VPCs showed strong animal-to-animal variability, with the AC often positioned between P5.p and P6.p. In addition, we found that variability in AC position gave rise to significant variability in expression patterns of 1°fate markers between animals, with adjacent VPCs often showing similar 1°fate induction levels in animals with a misplace AC. Yet, we found that vulva induction was canalized: the initial variability in AC position and 1°fate induction decreased over time, ultimately resulting in the same stereotypical cell fate pattern for all animals, with a single 1°fate cell directly adjacent to the AC. By quantifying Notch ligand expression as a measure of 1°fate induction and Notch signaling, and by comparing our results to mathematical models of the induction process, we identified the combined action of (1) graded EGF signaling, (2) lateral Notch inhibition, and (3) EGF-induced VPC movement toward the AC as the key requirements for the observed canalization of AC misplacement and 1°fate induction.
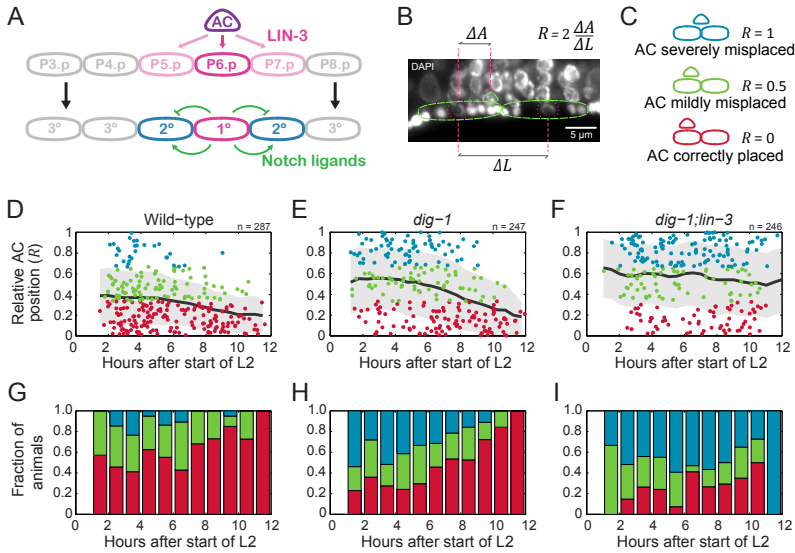
Figure 3.1 Correction of AC misplacement

A Overview of vulva induction. LIN-3 from the AC (magenta arrows) induces 1°fate and expression of the Notch ligands *lag-2* and *apx-1* in P5.p – P7.p. Subsequent Notch signaling (green arrows) inhibits 1°and induces 2°fate in P5.p and P7.p.

B Definition of the relative AC position R. Cell positions are given by the position of the cell nuclei, which are visualized by DAPI. Green lines show the approximate outlines of the AC and VPCs, and magenta circles indicate the VPC nuclei. The other nuclei inside the outline of the VPC belong to adjacent neurons.

C Examples of different observed classes of AC position: correctly placed (red, $0 \leq R < 1/3$), mildly misplaced (green, $1/3 \leq R < 2/3$), and severely misplaced (blue, $2/3 \leq R \leq 1$).

D – F Relative AC position R as a function of time during vulva induction in wild-type animals (**D**), *dig-1* mutants (**E**), and *dig-1;lin-3(e1417)* mutants (**F**). Each marker corresponds to the relative AC position in an individual animal and the color of the marker corresponds to the degree of AC misplacement as defined in panel **C**. The black line indicates the moving average of the relative AC position and the gray area indicates the standard deviation, both with a window size of 2 hours.

G – I The fraction of animals with a correctly placed AC (red), mildly misplaced AC (green), and severely misplaced AC (blue) as a function of time for wild-type animals (**G**), *dig-1* mutants (**H**), and *dig-1;lin-3(e1417)* mutants (**I**). The difference between *dig-1* and *dig-1;lin-3(e1417)* animals is significant (Kolmogorov-Smirnov test, $p < 10^{-5}$).

3.2 Results

3.2.1 Variability in AC position and 1°fate induction is corrected during vulva induction

We measured the position of the AC relative to the VPCs in fixed wilt-type (N2) animals using DAPI staining to visualize cell nuclei. We defined the relative AC position as $R = 2\Delta A/\Delta L$, where ΔA is the distance between the AC and the closest VPC, and ΔL is the distance between the two closest VPCs (Figure 3.1B). Distances were measured along the body axis of the animals and cell positions were defined as the center of their nuclei. A relative AC position of $R = 0$ corresponded to an AC correctly positioned adjacent to the closest VPC, whereas $R = 1$ corresponded to a maximally misplaced AC, i.e. equidistant to the two closest VPCS (Figure 3.1C). We chose a definition of R that does not depend explicitly on the position of P6.p, as the variability in AC position caused the exact identity of the closest and the second closest VPCs to vary between individuals, particularly in the mutants studied further below. For each fixed animal, we determined the sage of vulva induction by measuring the gonad length, defined as the distance between the two distal tip cells (DTCs). Gonad length increases during vulva induction [22] and serves as a reliable measure of the time relative to the start of the L2 larval stage [21] (see methods in section 3.4). We found that in wild-type animals during the early induction stage ($<$ 3 hours into the L2 stage) the AC position was highly variable with a significant fraction of animals showing a severely misplaced AC ($2/3 \leq R \leq 1$, Figures 3.1D, 3.1G (blue), and Figure 3.2B). In those cases, the AC was often positioned between P5.p and P6.p (Figure S3.1). However, during induction the variability in AC position and the average degree of AC misplacement decreased, with all animals having $R \leq 1/3$ at the end of induction (Figures 3.1D, 3.1G (red)). These observations suggested that the process of vulva induction is able to correct for significant deviations in the AC position. Similar correction of AC misplacement was observed recently in [23], both in *C. elegans* and other nematode species, suggesting it is crucial for vulva induction.

To examine the mechanism underlying the correction of AC misplacement, we quantified the expression level of the Notch ligands *apx-1* and *lag-2* in the VPCs as a function of the degree of AC misplacement. Expression of these two Notch ligands is induced by the EGF/Ras signaling pathway and is a measure of 1°fate induction [21, 24, 25]. We quantified

Notch ligand expression using single-molecule fluorescence in situ hybridization (smFISH) to visualize and count individual mRNA molecules in fixed animals [26, 27]. In general, we observed different patterns of Notch ligand expression depending on the degree of AC misplacement. For animals with a correctly place AC ($R \approx 0$) we saw *apx-1* expression predominantly in P6.p and at low levels (Figure 3.2A, left and middle panels). At this early stage *lag-2* expression was very low. At the late induction stage both *apx-1* and *lag-2* were expressed in P6.p at much higher levels (Figure 3.2A, right panel). We observed a strikingly different expression pattern in animals with a severely misplaced AC ($R \approx 1$). Here, at the early induction stage we frequently observed animals with nearly equal levels of *apx-1* expression in the two closest VPCs (Figure 3.2B, left panel), likely reflecting that they received similar levels of EGF input. However, in older animals with $R \approx 1$ we observed that *apx-1* expression was restricted to only one of the two VPCs (Figure 3.2B, right panel). Finally, we did not observe older animals with misplaced ACs ($R \geq 2/3$, Figures 3.1D, 3.1G).

During wild-type development, severe AC misplacement occurred in a significant but still limited fraction of animals. To analyze the response of vulva induction to severe AC misplacement, we therefore sought to increase variability in AC position. In most *dig-1(n1321)* animals, the gonad, which contains the AC, is shifted anteriorly with the AC most closely to P5.p [28]. In such cases, the vulva is properly induced, but often centered on P5.p instead of P6.p (Figure S3.1 s1). We found that AC position was highly variable in *dig-1* mutants during early induction, with many animals having $R \geq 2/3$ (Figures 3.1E, 3.1H (blue)). In *dig-1* animals with P5.p correctly aligned with the AC, *apx-1* and *lag-2* were typically expressed only in P5.p, with dynamics similar to those observed for P6.p in wild-type animals (Figure S3.2). We found that in *dig-1* mutants, despite the increased frequency of animals with a severe AC misplacement at early induction, the degree of AC misplacement decreased as vulva induction progressed, similar to wild-type animals (Figures 3.1E, 3.1H). In particular, we found no animals with $R \geq 2/3$ at the end of induction (> 10 hours after the start of L2). Additionally, we found for *dig-1* animals the same progression of Notch ligand expression patterns as a function of AC misplacement that we observed in wild-type animals (Figures 3.2C, 3.2D). Therefore, we analyzed the response to AC misplacement in *dig-1* rather than wild-type animals, focusing on *apx-1* , the earliest expressed Notch ligand.

To systematically examine the time dynamics of *apx-1* expression as a function of the relative AC position R, we quantified the relative *apx-*
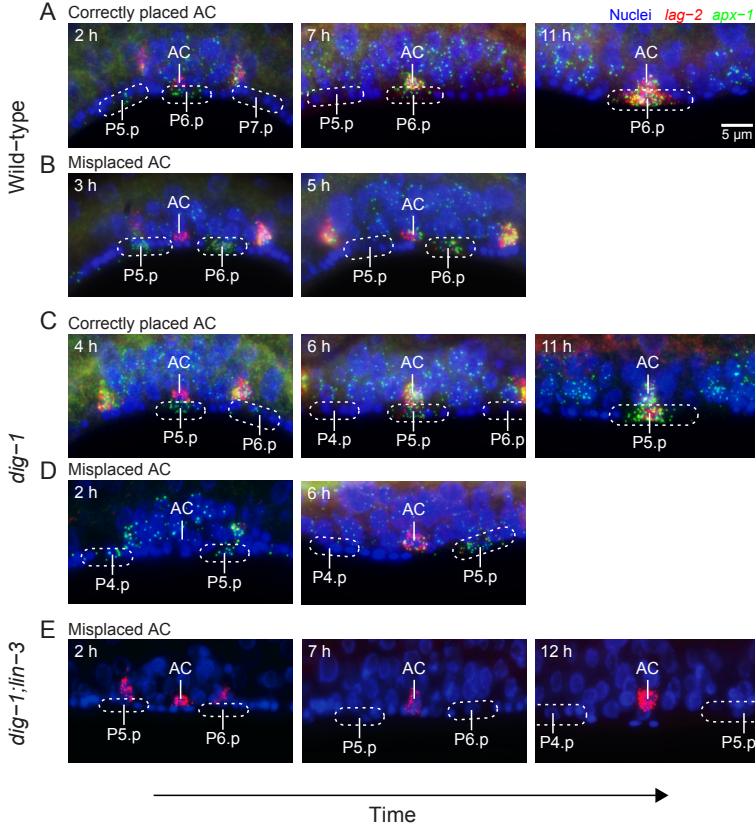
Figure 3.2 Examples of AC position and Notch ligand expression during vulva induction

A – B Representative examples of expression patterns of Notch ligands *apx-1* (green) and *lag-2* (red) in VPCs for wild-type animals with a correctly placed AC (**A**) and a severely misplaced AC (**B**), at different stages of vulva induction. Single *apx-1* and *lag-2* mRNA molecules are visualized as diffraction-limited spots using single-molecule fluorescence in situ hybridization (smFISH) and cell nuclei are stained by DAPI (blue). Time corresponds to hours after the start of L2. For the late induction stage ($<$ 9 hours), we did not observe animals with a severely misplaced AC. Notch ligands are not only visible in VPCs, but also in other cells in the gonad including the AC.

C – D Typical expression patterns in *dig-1* mutants with a correctly positioned AC (**C**) and a severely misplaced AC (**D**).

E Typical expression patterns in *dig-1;lin-3(e1417)* mutants with a severely misplaced AC. Due to the lack of vulva induction in this mutant, *apx-1* and *lag-2* expression in VPC is strongly reduced and hence not visible.

1 expression level E defined as $E = (M_1 - M_2)/(M_1 + M_2)$. Here, M_i indicates the number of *apx-1* mRNAs in the closest (M_1) and the second closest (M_2) VPCs with respect to the AC. With this definition, $E = 1$ corresponds to an animal in which all *apx-1* mRNAs are expressed in the closest VPC, $E = -1$ corresponds to all *apx-1* mRNAs expressed in the second closest VPC, and $E = 0$ corresponds to equal *apx-1* mRNA levels. In Figure 3.3A, we plot for each animal the relative *apx-1* expression level as a function of time, with the color of the marker indicating the degree of AC misplacement as shown in Figure 3.1C. For animals at the start of induction, we frequently observed equal levels of *apx-1* expression in both closest VPCs ($-1/3 \leq E < 1/3$, Figure 3.3A). This symmetric *apx-1* expression pattern correlated with R, occurring more frequently in animals with severely misplaced ACs ($2/3 \leq R \leq 1$, Figure 3.3C). However, the fraction of animals exhibiting *apx-1* expression in both VPCs decreased rapidly over the course of induction, with *apx-1* expression restricted to the closest VPCs in all animals at the end of induction ($1/3 \leq E \leq 1$, Figures 3.3A, 3.3B).

We compared the relative timing of the decrease in AC misplacement with that of the restriction of *apx-1* expression to a single VPC by plotting the fraction of animals found for each combination of R and E at the early, middle and late stages of vulva induction (Figures 3.3C – 3.3E and Figure S3.3). In general, restriction of *apx-1* expression appeared to precede the correction of AC misplacement, particularly for animals with misplaced ACs ($R \approx 1$, $E \approx 1$, Figures 3.3C, 3.3D), with full correction of AC misplacement only observed subsequently at the late induction stage (Figure 3.3E). However, we also observed a significant simultaneous decrease in AC misplacement from the early to the middle induction stages (Figures 3.1H, 3.3C, 3.3C), suggesting that the correction of AC position itself could also contribute to canalization of 1° fate induction by bringing one VPC closer to the AC and thereby increasing the amount of LIN-3/EGF signal it receives.

3.2.2   Induced 1° fate VPCs move towards the AC

The expression dynamics in Figure 3.3 suggested that active correction of AC position could be important for the canalization of the observed variability in 1° induction. However, animals grow significantly during vulva induction and the observed change in AC position could instead be due to divisions and rearrangement of cells surrounding the AC, independent
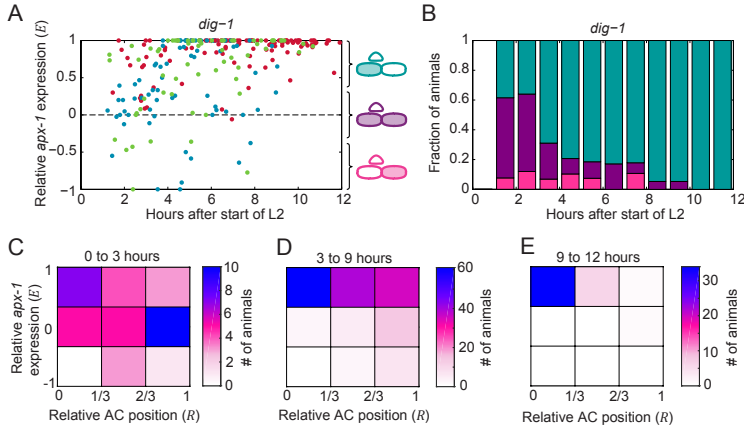
Figure 3.3 Notch ligand expression dynamics as a function of AC position

A Relative *apx-1* expression level E as a function of time in *dig-1* animals. Each marker represents the *apx-1* expression pattern in an individual animal and is colored according to the degree of AC misplacement as shown in Figure 3.1C.

B Fraction of animals exhibiting the different classes of *apx-1* expression patterns indicated schematically in **A**: most *apx-1* expression in the closest VPC (cyan, $1/3 \leq E \leq 1$), symmetric *apx-1* expression in the two closest VPCs (purple, $-1/3 \leq E < 1/3$), and most *apx-1* expression in the more distant VPC (magenta, $-1 \leq E < -1/3$), as a function of the time of induction.

C – E Number of animals with relative *apx-1* expression level E and relative AC position R for the early (**C**, $0 - 3$ h), intermediate (**D**, $3 - 9$ h), and late (**E**, $9 - 12$ h) induction stages.

of the induction process. To test whether the correction of AC position depended on vulva induction, we measured the relative AC position in *dig-1;lin-3(e1417)* mutant animals. In *lin-3*(e1417) mutants, *lin-3* expression is reduced specifically in the AC, leading to loss of 1° and 2° fate induction [29] and to the absence of *apx-1* and *lag-2* expression in the VPCs (Figure S3.2). In *dig-1;lin-3(e1417)* animals, we observed the same distribution of R during early induction as in *dig-1* animals, but we did not see a significant reduction in AC misplacement over time (Figures 3.1F, 3.1I). In particular, we found many *dig-1;lin-3(e1417)* animals with $R \geq 2/3$ at the end of induction (Figure 3.2E). Hence, the observed correction of AC misplacement was the result of an active process that depended on the presence of the LIN-3/EGF signal. This link between the AC position and LIN-3/EGF signaling was also found independently in [23]. In addition, our experiments indicated that this is controlled upstream of the Ras target LIN-1 (Figure S3.4).

The observed alignment between a single 1°fate VPC and AC at the late induction stage raised the question whether this alignment depended specifically on 1°induction and if so, whether the 1°fate VPC moved towards the AC or, instead, the AC moved towards the 1°fate VPC. To address this question, we examined the positions of 1° fate VPCs with respect to the AC in a *lin-12*(0) mutant, where multiple VPCs assume 1°fate [30]. In this mutant, the LIN-12/Notch receptor that mediates Notch signaling between adjacent VPCs is not functional. In addition, as *lin-12* is also involved in the specification of the AC, *lin-12*(0) mutants often have two ACs [30], likely leading to increased LIN-3/EGF levels. These combined effects cause not only P6.p but also P5.p and $\sim$ 60% of P7.p cells to assume 1°fate [31]. We measured the position of P(5 − 7).p along the body axis as a function of time, in both wilt-type and *lin-12*(0) animals (Figure 3.4C). We observed that in *lin-12*(0) mutants during the late vulva induction stage, $\sim$ 90% of P5.p cells and $\sim$ 60% of P7.p cells were located significantly closer to the ACs ($< 9h$, Figures 3.4A − 3.4C) and P6.p (Figure S3.5G) compared with wild-type animals. We examined whether this displacement of P5.p and P7.p depended on 1°induction. Indeed, we found that displacement towards the AC correlated strongly with the expression level of the 1°fate marker *apx-1* (Figure 3.4I). This correlation was particularly striking for P7.p: cells with low *apx-1* expression were often observed at wild-type distances to the AC (Figures 3.4A, 3.4I), while cells with high expression were positioned much closer (Figures 3.4B, 3.4I). Moreover, in *lin-12*(0) animals ectopic expression of *apx-1* was observed in P5.p hours before that cell moved closer to P6.p, showing that 1°induction preceded VPC migration (Figures S3.4D, S3.4E).

The general observation that in animals with multiple 1°fate VPCs these cells are located closer to another (Figures 3.4C, S3.5G) can only be explained by 1°fate VPCs moving towards the AC rather than the reverse. This is consistent with previous observations in which the AC showed no movement with respect to seam cells and body muscles during the course of induction [23, 28], and when the proximal VPCs (P(5–7).p) are ablated, distal VPCs such as P8.p can assume 1° and move towards the AC [23, 32]. Surprisingly, we observed that in *lin-12*(0) animals in which two VPCs were induced, these were often positioned equidistant to the ACs. This shows that VPC movement by itself does not necessarily result in configurations with a single VPC aligned with the AC.
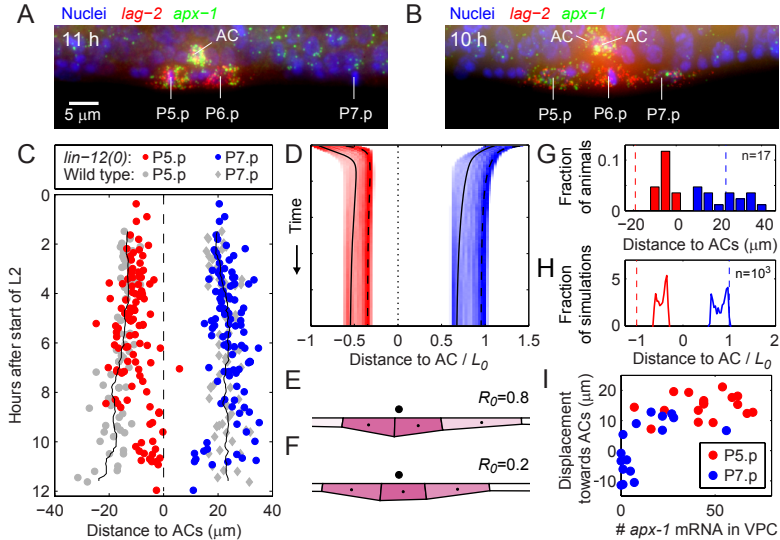
Figure 3.4 Movement of 1° fate VPCs to the AC

A Example of a *lin-12(0)* mutant animal with two induced VPCs at the late vulva induction stage. Expression of *apx-1* (green) and *lag-2* (red) is visualized using smFISH. Nuclei (blue) are stained with DAPI. *lin-12(0)* animals usually have two ACs. The positions of the ACs and VPC nuclei are indicated.

B Example of a *lin-12(0)* mutant animal with three induced VPCs at the late induction stage.

C Distance of the P5.p and P7.p cells to the ACs in wild-type animals ($n = 287$, grey squares for P5.p and grey diamonds for P7.p) and *lin-12(0)* mutant animals ($n = 112$, red circle for P5.p and blue circle for P7.p) as a function of the time of induction. Each marker corresponds to an individual animal. Also shown are the moving averages, with a window size of 1 hour, of the distance of P5.p and P7.p to P6.p for wild-type animals (black lines).

D Distribution of distance of P5.p (red) and P7.p (blue) to the AC as a function of time of the gradient-sensing (G-S) model without Notch signaling. The distribution was calculated for $n = 10^3$ simulations with LIN-3/EGF level $p_0 = 1.37$ and a random initial relative AC position between $R_0 = 0$ (centered on P6.p) and R_1 (equidistant to P5.p and P6.p.). Also shown are trajectories for individual simulations with $R_0 = 0.2$ (solid line) and $R_0 = 0.8$ (dashed line). Distances are given in units of the length L_0 of undeformed VPCs.

E and **F** Steady-state model configuration for the trajectories shown in **D** with $R_0 = 0.8$ (**E**) and $R_0 = 0.2$ (**F**). Also shown are the AC position (black circle) and induction level (indicated in magenta).

Figure 3.4

G and **H** Distribution for steady-state distance of P5.p (red) and P7.p (blue) to the AC for the *lin-12*(0) mutant at the late induction stage (**G**) and the G-S model without Notch signaling (**H**). Dashed lines indicate the mean distance of P5.p (red) and P7.p (blue) in wild-type animals (**G**< 9 h) and in the G-S model with no induction (**H**, $p_0 = 0$).

I Displacement of P5.p (red) and P7.p (blue) towards the ACs as a function of *apx-1* expression level in each VPC. All animals are at the late induction stage (< 9 h, $n = 34$). The displacement is defined as the distance between each VPC and the ACs minus the average distance for wild-type animals at the same time of induction, as given by the black line in **C**.

3.2.3 Distinct spatial VPC configurations in a mathematical model of LIN-3-induced VPC movement

The above results suggested that the variability in AC position relative to the VPCs is canalized by the movement of 1° fate VPCs towards the AC. To examine whether VPC movement could also contribute to the canalization of variability in 1° fate induction or whether Notch signaling is required for this, we constructed a mathematical model of LIN-3/EGF-induced VPC movement without Notch signaling. To implement movement and deformation of VPCs we used a two-dimensional "vertex model" where cells are represented by edges that are connected in vertices (Figure 3.5A, equations 5.1 and 5.2 in section 3.4). Such models accurately describe movement and rearrangement of cells in epithelial tissues and allow for cell deformation due to internal and external forces [33].

Little is known about the molecular mechanisms that control VPC movement. However, two qualitatively different general mechanisms have been proposed to explain cell migration in a chemoattractant gradient: "attractant-maximization" (A-M, equation 5.3 in section 3.4) where cells change their position and shape to maximize the amount of attractant integrated over their surface [34], and "gradient-sensing" (G-S, equation 5.4 in section 3.4) where cells measure the external chemoattractant gradient and move in the direction of the largest increase in attractant concentration [35]. To implement A-M and G-S models of VPC movement, we assumed that an exponential LIN-3/EGF gradient $p(x)$, centered at the AC, acts as a chemoattractant to provide the directional cue (Figure 3.5B, black line; equation 3.5 in section 3.4). In addition, we assumed LIN-3/EGF plays a second role in controlling VPC movement. Following the experimentally observed correlation between VPC movement and 1° induction (Figure 3.4I) we assumed that the propensity to migrate increases with the Ras activation level ϕ (Figure 3.5B, magenta line; equation 3.6 in section 3.4), which

itself depends on the absolute level of external LIN-3/EGF.

When varying the total LIN-3/EGF level $p_0 = \int_{-\infty}^{\infty} p(x)dx$, both models generate steady states that cluster around a small number of distinct VPC configurations, with sudden transitions between configurations as p_0 increases (Figures 3.5C, 3.5D and Figure S3.5). These configurations resemble those observed experimentally in mutants that differ in LIN-3/EGF level: for low p_0 there is neither induction nor correction of AC misplacement (Figures 3.5C, 3.5D, configuration 4), similar to the *lin-3*(e1417) mutant. For intermediate p_0, a single VPC is induced and aligns with the AC (Figures 3.5C, 3.5D, configuration 3) as in wild-type animals. For high p_0 we observe two configurations seen in the *lin-12*(0) mutant with two LIN-3-expressing ACs (Figures 3.5C, 3.5D, configurations 1 and 2), with either P5.p and P6.p induced and equidistant to the AC, or P(5–7).p induced and P6.p aligned with the AC. The steady-state configurations depend on the initial degree of AC misplacement (Figure 3.5D), reflecting that stronger VPC deformation and, hence, larger forces are required to correct for more severe AC misplacement.

To gain insight into the origin of the different configurations, we calculated the total migration force produced by each VPC as a function of distance to the AC. Even though the A-M and G-S models differ strongly in cell shape dynamics (Figure S3.5), the expressions for their force-distance curves are identical (equation 3.5 in section 3.4) and have a characteristic shape (Figure 3.5B): at sufficiently large distances from the AC, the magnitude of the force increases with the Ras activation level ϕ However, the force peaks once either the anterior or posterior edge of the VPC aligns with the AC. When the VPC is positioned closer to the AC, the two sides of the VPC body are exposed to opposing gradients, causing the force to decrease and ultimately vanish when the VPC is aligned with the AC. For intermediate p_0 when only P6.p is induced, this decrease in force ensures that the cell comes to rest when aligned with the AC. However, this property of the force-distance curve also leads to stability of the misaligned configuration with two induced cells (Figure 3.5C, configuration 2) for larger p_0. In this case, even when the AC is positioned much closer to P6.p than P5.p, P6.p will produce a lower migratory force than P5.p due to its proximity to the AC. As a result, P5.p will push P6.p away from the AC until they are equidistant and produce equal but opposite migration forces. For even larger p_0, this configuration becomes unstable: as P6.p contracts towards the AC, P7.p is pulled closer and is also induced. P6.p and P7.p together produce sufficient force to push P5.p away from the AC, leading to a con-
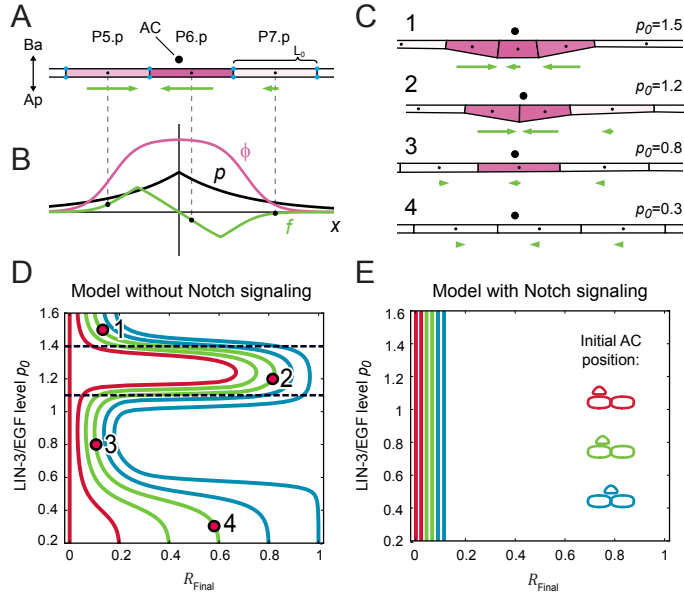
Figure 3.5 Mathematical model of canalized vulva induction

A Overview of the model without Notch signaling (equations 5.1–3.6 in section 3.4). VPC geometry is determined entirely by the position of the vertices where cell edges meet (blue dots). The forces produced by the VPCs (green arrows) depend on both their position relative to the AC (black circle) and their level of Ras signaling (indicated in magenta). Also shown is the apical-basal axis (Ap-Ba). L_0 corresponds to the length of the undeformed VPC body along the A-P axis.

B The LIN-3/EGF gradient p (black line), Ras activation ϕ (magenta line), and force f (green line) as a function of the distance to the AC. Black markers indicate values for the configuration in **A**.

C Examples of different steady state configurations obtained with the model when varying the total LIN-3/EGF level $p_0 = \int_{-\infty}^{\infty} p(x)dx$. Configurations 1 and 2 coincide with those observed in the *lin-12*(0) mutant, while configurations 3 and 4 match those in wild-type and *lin-3*(e1417) animals respectively.

D Diagram representing the final relative AC position R_{final} as a function of the LIN-3/EGF level p_0. Lines correspond to different initial AC positions $R_0 = 0, 0.2, 0.4, 0.6, 0.8, 1.0$ and are colored according to the initial degree of AC misplacement as shown in **E**. Points labeled $1-4$ correspond to the configurations in **C**. The dashed lines indicate the transition regions where the final cell configuration depends strongly on the initial AC position.

E Similar to **D** but for the model that includes Notch signaling. The system evolves towards the desired VPC configuration with $R \approx 0$ for all initial AC positions and LIN-3/EGF levels. The colored cell diagrams correspond to the different degrees of initial AC misplacement R_0 as described in Figure 3.1C.

figuration with P6.p aligned by the AC and compressed by the opposing forces of P5.p and P7.p. Additional modeling showed that the shape of the force-distance curve in Figure 3.5B, with the magnitude of the force peaking at a distance to the AC comparable to the size of a VPC, is essential for reproducing the experimentally observed configuration with two VPCs equidistant to the AC (Figure S3.6).

For LIN-3/EGF levels at the transition between different stable cell configurations, the steady-state configuration depends strongly on the initial AC position (Figure 3.5D, dashed lines). Interestingly, the VPC induction and migration dynamics in these regimes can provide an appealing explanation for the broad range of VPC configurations we observed in *lin-12*(0) mutants (Figures 3.4A – 3.4C). For instance, for $p_0 = 1.4$ the model evolves towards the configuration with two induced VPCs equidistant to the AC for a sufficiently misplaced AC, but generates the configuration with P(5 – 7).p induced and P6.p aligned with the AC for more correctly positioned ACs (Figures 3.4D – 3.4F). In *lin-12*(0) mutants, we also observed that induced P5.p and P7.p cells were more closely positioned to the ACs (Figures 3.4C, 3.4I) and P6.p (Figure S3.5G) than when not induced. Based on this observation, we can rule out the A-M model in favor of the G-S model. In the A-M model, where cells elongate along the A-P axis to maximize overlap with the LIN-3/EGF gradient, induced P5.p and P7.p cells were positioned further part (Figure S3.5I). In contrast, in the G-S model P5.p and P7.p moved closer to the AC and to P6.p upon induction (Figures 3.4H, S3.5H). Moreover, when we assumed that the initial AC position was distributed uniformly between P5.p and P7.p, the G-S model reproduced both the average P5.p and P7.p positions and the broad distribution of P7.p positions relative to the AC that we observed experimentally (Figures 3.4G, 3.4H), with the main difference that the experimentally observed VPC positions were more widely distributed. Together, these results show that the experimentally observed variability in initial AC position alone could be sufficient to explain the intrinsic variability in VPC configuration observed in the *lin-12*(0) mutant. In addition, the overall agreement between the gradient-sensing model and the experiments suggests that it captures the essential features of LIN-3/EGF-induced VPC migration.

3.2.4 Notch signaling is essential for correction of errors in AC position and 1° fate induction

The results of the model showed that in principle LIN-3/EGF-induced VPC movement alone could correct for AC misplacement (Figures 3.5C, 3.5D, configuration 3). However, this is only achieved for a narrow range of LIN-3/EGF level p_0. Notch signaling, by restricting 1° fate to a single VPC, could drastically expand the range of LIN-3/EGF levels over which canalization would occur. Indeed, when we added Notch signaling to our mathematical model (equations 3.7 and 3.8 in section 3.4), we found that now the correct expression pattern and position of the AC was realized for the full range of p_0 (Figure 3.5E). To examine the contribution of Notch signaling to canalization, we sought to inhibit the Notch pathway without affecting AC specification, as the additional ACs in the *lin-12*(0) mutant likely increase the amount of secreted LIN-3/EGF. We shifted a *dig-1* mutant carrying a temperature-sensitive *lin-12* mutation, *dig-1;lin-12*(n676n930ts), to 25°C at the start of vulva induction. Indeed, these animals possessed a single AC (Figure 3.6B), even though *lin-12* animals have multiple ACs when grown at 25°C during the L1 and L2 larval stages [36]. The model made a strong prediction for the effect of loss of Notch signaling: if LIN-3/EGF-induced VPC movement alone were sufficient to correct for AC misplacement and variability in 1° fate induction, corresponding to the model at low LIN-3 level, then *dig-1;lin-12*(ts) animals with inhibited Notch signaling would correct this as efficiently as *dig-1* animals. However, for higher LIN-3 levels, the model predicted that inhibition of Notch signaling would result in multiple 1° fate cells with aberrant spatial configurations, similar to the *lin-12*(0) mutant (Figure 3.4).

We found that during early induction (0−−3 h, Figure 3.6A) the relative AC position in *dig-1;lin-12*(ts) at 25°C showed a wide distribution, similar to *dig-1* animals (Figure 3.1E). Whereas *dig-1* animals efficiently canalized the variability in AC position and 1° fate induction, we found that *dig-1;lin-12*(ts) animals at 25°C showed a wide range of relative AC positions and *apx-1* expression patterns (Figures 3.6A – 3.6C). Moreover, animals with a misplaced AC also typically showed equal expression of Notch ligands in the two closest VPCs ($E = 0$, Figures 3.6B, 3.6C and Figure S3.3). At the same time, *dig-1;lin-12*(ts) animals at 15°C corrected AC misplacement and restricted Notch ligand expression almost as well as *dig-1* animals (Figure S3.3). These observations differ from those in [23] where the correction of AC misplacement was not impacted by RNAi knockdown of *lin-12*. This could be due to a weaker effect of RNAi compared to the *lin-12(ts)* mutant
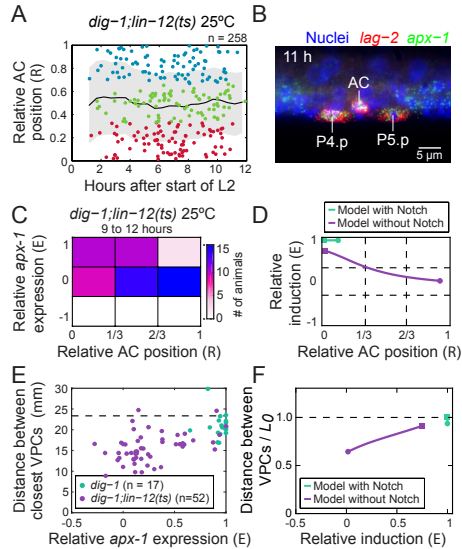
Figure 3.6 Vulva induction in the absence of Notch signaling

A Relative AC position R as a function of time during vulva induction in *dig-1;lin-12*(ts) animals shifted to 25°C after AC specification. The difference with *dig-1* animals in Figure 3.1E is significant (Kolmogorov-Smirnov test, $p = 10^{-5}$).

B *dig-1;lin-12*(ts) animal with misplaced AC and Notch ligand expression in two VPCs. Expression of *apx-1* (green) and *lag-2* (red) is visualized using smFISH. Nuclei (blue) are stained with DAPI.

C Number of animals with relative *apx-1* expression level E and relative AC position R for the late induction stage (< 9 h). The difference with *dig-1* animals in Figure 3.3E is significant (Kolmogorov-Smirnov test, $p, 10^{-5}$).

D Steady-state relation between relative position R and relative induction level E for the model with Notch signaling (green line) and without Notch signaling (purple line). The relative induction level is given by $E = (\phi_1 - \phi_2)/(\phi_1 + \phi2)$ where ϕ_1 and ϕ_2 are the induction levels in the closest and second closest VPCs. Both models were evaluated at LIN-3/EGF level $p_0 = 1.1$, and with an initial relative AC position R varying from equidistant to P5.p and P6.p ($R = 1$, indicated by the circle), to centered on P6.p ($R = 0$, square).

E Distance between the closest and the second closest VPC as a function of the relative *apx-1* expression level, both for *dig-1* (green) and *dig-1;lin-12*(ts) (purple) animals at the late induction stage (< 9 h). The dashed line corresponds to the average distance in the *dig-1;lin-3(e1417)* mutant without induction. Only animals in which the AC is position between P4.p and P5.p are shown.

F Distance between the closest and second closest VPC as a function of the relative induction level, both for the model with Notch signaling (green) and without (purple), for the same range of initial AC positions as in **D**. The dashed line corresponds to the distance between VPCs in the absence of induction ($p_0 = 0$).

and to the fact that it was performed in wild-type animals, where severe AC misplacement is infrequent compared to *dig-1* mutants. We also observed a high fraction of animals with a single aligned 1° fate VPC at the end of induction in the *lin-12(ts* single mutant at 25°C (Figure S3.7).

We found that the wide distribution of configurations with either one or two induced VPCs observed in *dig-1;lin-12*(ts) animals resemble the steady states generated by the model without Notch signaling at the transition regime $p_0 = 1.1$ (Figure 3.5D). Specifically, the model reproduced the experimental observation that in configurations with two induced VPCs, the cells are equidistant to the AC ($E \approx 0$, $R \approx 1$, Figures 3.6C, 3.6D), whereas in configurations with a single induced VPC, the cell is aligned with the AC ($E \approx 1$, $R \approx 0$). The model also predicted a correlation between induction pattern and VPC deformation: as two induced VPCs will migrate toward another, the distance between them should be smaller than that of a single induced VPC to its neighbors (Figure 3.6F). Indeed, we confirmed experimentally that VPCs were positioned closer together if they exhibited more similar *apx-1* expression levels ($E = 0$) when compared to VPC positions both in *dig-1* animals that have a single 1° fate VPC and *lin-3*(e1417) animals with no induced VPCs (Figure 3.6E). Taken together, these results show that for wild-type animals VPC movement alone is insufficient to produce the correct 1° fate pattern and that Notch signaling between VPCs is essential to restrict 1° fate induction and VPC migration to a single VPC.

3.2.5 VPC movement helps Notch signaling correct errors in 1° fate induction

Given that VPC movement alone can generate the correct 1° fate pattern for the full range of initial AC positions but a narrow range of low LIN-3/EGF levels ($0.7 < p_0 < 1$; Figures 3.5C, 3.5D, configuration 3), we examined whether VPC movement could support Notch signaling in restricting 1° fate to a single VPC for $p_0 = 1.1$, the higher level consistent with the *dig-1;lin-12*(ts) mutant. Indeed, we found that adding a small amount of VPC movement to the model with Notch signaling dramatically increased the difference in steady-state induction level between the closest and the second closest VPCs (Figure 3.7A). Increasing the amount of VPC movement further did not impact the steady-state induction level, but it did significantly increase the speed of 1° fate restriction (Figure 3.7B). While
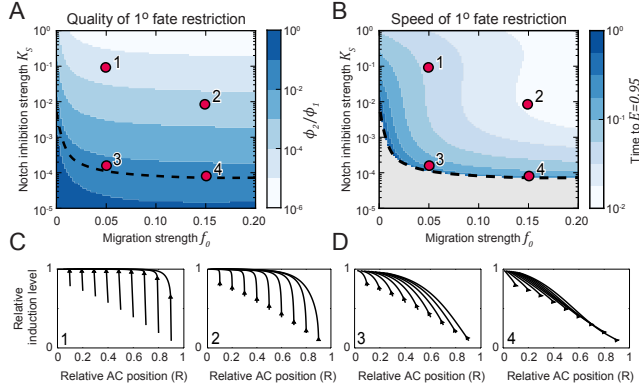
Figure 3.7 Cooperation between Notch signaling and cell migration in canalization of 1° fate induction

A Restriction of 1° fate induction to a single VPC for the model with Notch signaling (equations 5.1–3.7 in section 3.4), as a function of the Notch inhibition strength K_S and cell migration strength f_0. Simulations were started with two VPCs approximately equidistant to the AC ($R_0 = 0.9$). Color indicates the quality of restriction at steady state, given by ϕ_2/ϕ_1. Here, ϕ_1 and ϕ_2 are the induction levels in the closest and the second closest VPCs, and complete restriction of 1° fate to the closest VPC corresponds to $\phi_2/\phi_1 = 0$. The dashed line corresponds to a steady-state relative induction level $E = 0.95$, where $E = (\phi_1 - \phi_2)/(\phi_1 + \phi_2)$. Red markers correspond to the simulations highlighted in **C** and **D**.

B Time required to restrict 1° fate induction to a single VPC. Simulations were performed as in **A**, and the time was measured until the relative induction level reached the value $E = 0.95$. The color indicates the time normalized to the longest time encountered for the ranges of K_S and f_0 examined here. For the grey region below the dashed black line, $E < 0.95$ in steady state and hence the time was not recorded. Red markers correspond to the simulations highlighted in **C** and **D**.

C, **D** Time dynamics of relative AC position R and relative induction level E for strong (**C**) and weak (**D**) Notch signaling and different levels of cell migration. Each trajectory corresponds to a different initial AC position, ranging from $R_0 = 0.1$ and $R_0 = 0.9$. Note that in this deterministic model the relative induction level is always positive. Numbers correspond to the markers in **A** and **B**.

the model dynamics for weak Notch signaling and strong VPC movement was inconsistent with the experiments (Figures 3.3C – 3.3E and Figure 3.7D), for strong Notch signaling the model reproduced the experimentally observed dynamics also in the limit where VPC movement strongly contributes to the speed of 1° fate restriction (Figure 3.7C). These results show that, during 1° fate induction, VPC movement and Notch signaling might be highly intertwined: in this picture, Notch signaling is required for correction of AC misplacement by restricting VPC movement to a single cell, but VPC movement in turn helps Notch signaling by bringing one cell closer to the AC and thereby increasing its level of Ras activation and Notch ligand expression. As a result, even though in the model VPC movement (Figure 3.5D) and Notch signaling (Figure 3.7A) alone can produce the correct 1° fate induction pattern, albeit for a limited range of parameters, the combination of both mechanisms canalizes variability in AC position and 1° fate induction much more efficiently and over a much wider range of biochemical parameters such as the LIN-3 level.

3.3   Discussion

How development always results in the same adult structures despite strong genetic, environmental, and intrinsic variability is a fundamental unsolved question. In *C. elegans* vulva induction, the AC induces vulva cell fate in the VPCs in a distance dependent manner, resulting in an invariant cell fate pattern with 1° fate only induced in the closest VPC, P6.p. Surprisingly, we found that the initial position of the AC with respect to the VPCs showed strong variability, with the AC located equidistant to two VPCs, typically P5.p and P6.p, in $\sim$ 20% of wilt-type animals. A strong initial variability, correlated with AC position, was also observed in 1° fate induction as measured by expression of the Notch ligand *apx-1*. Specifically, if the AC was equidistant to two VPCs, 1° fate was often initially induced at equal levels in both VPCs (Figure 3.3). However, we observed that vulva induction was canalized, i.e. both the variability in AC position and 1° fate induction decreased in time, resulting in the same configuration with a single 1° fate cell aligned with the AC in all animals (Figure 3.3).

We found that AC misplacement was corrected by movement of the 1° fate VPC that depended on LIN-3/EGF from the AC (Figures 3.1, 3.4).

31

Canalization of 1° fate induction was achieved by the progressive restriction of 1° fate to a single VPC, which occurred simultaneously with correction of AC misplacement (Figure 3.3). A mathematical model of LIN-3/EGF-induced movement of VPCs towards the AC showed that VPC movement alone, by bringing one cell closer to the AC, could be sufficient to restrict 1° fate to a single VPC (Figure 3.5). However, we found that Notch signaling between VPCs was crucial for 1° fate restriction: upon inhibiting Notch signaling, most animals failed to canalize variability in AC position and 1° fate induction, and instead exhibited a range of configurations with one or two 1° fate VPCs at varying positions to the AC (Figure 3.6). Yet, modeling showed that VPC movement can significantly improve 1° fate restriction by Notch signaling, leading to stronger and faster amplification of differences in 1° fate induction between adjacent VPCs (Figure 3.7). This shows that even though VPC movement (Figure 3.5D) and Notch signaling (Figure 3.7) alone can generate the correct 1° fate induction pattern, both mechanisms combined do so in a highly improved manner and for a much wider range of parameters.

The above mechanism acts by restricting 1° fate to the closest VPC rather than to P6.p specifically, raising the question of how 1° fate is invariably induced in P6.p. We found that in wild-type animals, severely misplaced ACs can be shifted towards either P5.p or P7.p (Figure S3.1). Yet, wild-type animals under normal growth conditions only rarely exhibit a VPC fate pattern that is shifted so that P5.p or P7.p assume 1° fate instead of P6.p [17, 18]. As a possible solution to this paradox, however, we observed no wild-type animals where the AC was positioned closer to P5.p or P7.p than to P6.p (Figure S3.1). This suggests the AC might be positioned just accurately enough that 1° fate is restricted to P6.p in almost all animals, even when using a mechanism that purely selects the closest VPC.

The observed alignment of the AC and the 1° fate VPC is likely also important for many aspects of vulva cell fate patterning morphogenesis that occur after 1° fate induction. First, the AC is responsible for induction of VulE and VulF fate in P6.p descendants by LIN-3/EGF signaling [37]. Second, a Wnt signal originating from the AC controls the proximal-distal orientation of the asymmetric divisions of the 1° and 2° fate lineages, with the daughter cell closest to the AC assuming a different pattern than the more distant daughter [38]. In both these cases, a misplaced AC could result in incorrect cell fate assignment. Finally, the AC is also instrumental in patterning the ventral uterus and connecting the uterus with the vulva

[39, 40], the success of which likely requires the precise alignment of the uterine cells, the AC and the cells of the P6.p lineage.

We have constructed the first model of vulva induction that takes into account VPC movement and deformation. The model did not only generate the qualitatively different induction patterns observed in wild-type animals and mutants with different numbers of 1° fate VPCs (Figure 3.5), but also correctly reproduced the quantitative changes in VPC configurations observed in these mutants (Figures 3.4, 3.6). In general, the model shows that LIN-3/EGF-induced movement is a potent force for establishing robust patterns, even in the absence of Notch signaling. As such, it might have implications for vulva induction in other nematode species. For instance, in the Panagrolaimidae both P6.p and P7.p assume 1° fate in an AC-dependent manner and are positioned equidistant to the AC [41, 42], a stable configuration naturally generated by our model (Figure 3.5C, configuration 2). Moreover, it shows that nematode species with the same 1° fate pattern as *C. elegans* might vary substantially in the relative importance of VPC movement and Notch signaling in restricting 1° fate to a single VPC. In general, the combination of long-range induction followed by Notch inhibition between and migration of the induced cells occurs more widely, for instance during development of the *Drosophila* tracheal system [43–45] and blood vessel formation in vertebrates [46]. Our results suggest that these common mechanisms might provide robustness, in particular to intrinsic variability in the position of the source of the inductive signal relative to the induced cells.

Finally, our observation that Notch signaling is required to canalize variability in 1° fate induction, caused in turn by variation in AC position, represents a significantly different role for Notch signaling than has been assumed so far. Specifically, this result could clarify a long-standing debate on the role of Notch signaling in vulva induction, namely whether 1° fate is induced in multiple VPCs and Notch signaling is required to restrict 1° fate to a single VPC (the "graded model") [20], or whether 1° fate is induced exclusively in P6.p and Notch signaling is only required subsequently to induce 2° fate in P5.p and P7.p (the "sequential model") [47]. When the AC is initially correctly placed relative to P6.p, the LIN-3/EGF gradient might be narrow enough to induce 1° fate only in P6.p, even without Notch signaling. Indeed, we often observed 1° fate induction in a single VPC in the absence of Notch signaling in *lin-12(ts)* mutants (Figure S3.7), where the initial variability in AC position is reduced compared to *dig-1;lin-12*(ts) mutants. However, in animals where the AC is severely misplaced, Notch signaling is

indeed essential to restrict 1° fate to a single VPC (Figure 3.6). Hence, this role of Notch signaling might exist as an insurance policy against the relatively infrequent cases of AC misplacement. Thus, it suggests that some aspects of signaling networks make sense as adaptations only when viewed in the light of the variability encountered during development.

3.4   Materials and methods

3.4.1   *C.elegans* strains and handling

Wild-type nematodes were strain N2. The following mutants were used in this study: LGIII: *lin-12(n941)* [30], *dig-1(n1321)* [28], *unc-32(e189) lin-12(n676n930)* [36]; LGIV: *lin-3(e1417)* [29], *lin-1(n1790)* [48].

All strains were handled according to the standard protocol [49]. Briefly, animals were grown on agar plates containing nematode growth medium (NGM) and *E. coli* strain OP50 as a food source. Unless otherwise indicated, all strains were grown at 20°C.

To inhibit Notch signaling without producing additional ACs, *dig-1(n1321);nc-32(e189) lin-12(n676n930)* eggs were placed on NGM plates at the permissive temperature (15°C), and were allowed to hatch. After 24 to 34 hours of plating the eggs, larvae were shifted to the restrictive temperature (25°C). Animals with two ACs were excluded. We also excluded animals carrying the *dig-1(n1321)* allele that displayed a dorsal gonad. The *unc-32(e189)* allele, which on its own has no vulva development defects, is used to follow the *lin-12(n676n930)* mutation to which it is closely linked.

3.4.2   Single-molecule fluorescence in situ hybridization

To visualize mRNA transcripts, smFISH was performed as previously described [26, 27]. Probes for smFISH were designed for optimal GC content using a web-based program (http://singlemoleculefish.com) and were couple to Cy5 or Alexa594. The sequences of the oligonucleotide probes used in this study have been published previously [21].

Animals were collected by washing plates with M9 and were fixed in 4% formaldehyde in 1x PBS for 25 minutes at room temperature. Fixed

animals were permeabilized in 70% ethanol overnight at 4°C. Subsequently, animals were incubated with the smFISH probes overnight at 30°C in hybridization solution containing 10% formamide. The next day, animals were washed twice with 10% formamide and 2x SS, each time followed by an incubation for 30 minutes at 30°C. To visualize cell nuclei, DAPI was added at $5\mu g/ml$ at the last washing step.

Microscopy images were acquired with a Nikon Ti-E inverted fluorescence microscope, equipped with a 100x plan-apochromat oil-immersion objective and an Andor Ikon-M CCD camera controlled by μManager software [50]. Exact three-dimensional positions of smFISH spots in each animal were detected using a custom MATLAB script, based on a previously published algorithm [26]. Briefly, we first convolved smFISH microscopy images with a Gaussian filter to increase the brightness of spots with the correct size and suppress the background signal. Next, we select candidate spots by thresholding, using a manually determined threshold. We further refined the candidate spots by finding regional intensity maxima within each spot, to separate smFISH spot whose fluorescence signals are partially overlapping. Finally, the resulting spots were manually assigned to individual VPCs.

We converted gonad length G, measured as the distance between the two DTCs, to time using the expression $G(t) = 17.7 + 0.54t$ for $t < 0$ and $G(t) = 17.7 + 0.54t + 0.72t^2$ for $t \geq 0$, where G is in the units of μm, t in units of hours, and $t = 0$ corresponds to the start of the L2 larval stage [21]. Distances between DTCs as well as between the AC and VPCs were all measured along the body axis of the animal.

3.4.3 Mathematical model of vulva induction

Overview

In the model, the position and shape of VPCs is determined by the position of basal vertices $\bar{r}_i^0$ and the apical vertices $\bar{r}_i^1$ (Figure S3.5A). In the absence of migration, we assume that the movement of vertices minimizes an energy function E of the form [33]

$$E(\bar{r}_i^j) = \frac{K}{2} \sum_{\text{cell } \alpha} (A_\alpha - A_\alpha^0)^2 + \sum_{\text{edge } \epsilon} \gamma_\epsilon l_\epsilon, \qquad (3.1)$$

where A_α is the surface area of cell α, K is the cell elasticity, l_ϵ is the length of edge ϵ and γ_ϵ is its line tension. For simplicity, we ignore cell growth and hence each cell has a constant preferred area A_α^0. This leads to the following equation of motion for the vertex model that includes migration

$$\frac{1}{\mu}\frac{d\bar{r}_i^j}{dt} = \bar{F}_A^{ij} + \bar{F}_\gamma^{ij} + \bar{F}_{\text{mig}}^{ij}, \tag{3.2}$$

where we assumed the movement of vertices is overdamped, and where μ is the mobility coefficient, $\bar{F}_A^{ij} = (K/2)(\partial/\partial\bar{r}_i^j)\sum_\alpha (A_\alpha - A_\alpha^0)^2$ is the elastic cell area force, $\bar{F}_\gamma^{ij} = (\partial/\partial\bar{r}_i^j)\sum_\epsilon \gamma_\epsilon l_\epsilon$ is the line tension force and $\bar{F}_{\text{mig}}^{ij}$ is an additional force that is not derived from the energy function in equation 5.1 and describes the cell migration in response to the LIN-3/EGF gradient. In the attractant maximization (A-M) model, cells seek to maximize the amount of attractant integrated over the cell surface [34] leading to

$$\bar{F}_{\text{mig}}^{ij} = \delta_{j0}[(\Phi_{i-1} - \Phi_i)p(x_i^j)]\hat{e}_x. \tag{3.3}$$

In the gradient sensing (G-S) model, cells generate an internal polarity based on the difference in chemoattractant concentration measured over the cell surface [35]. Here, for simplicity we assume a linear relationship between polarity and chemoattractant gradient, leading to

$$\bar{F}_{\text{mig}}^{ij} = \delta_{j0} \sum_{i'=i-1,j} \Phi_{i'}[p(x_{i'+1}^0) - p(x_{i'}^0)]\hat{e}_x. \tag{3.4}$$

For both the A-M and the G-S model, Φ_α is a coupling constant that describes how strongly cell α induces cell migration in response to the LIN-3/EGF signal and $p(x)$ is the local LIN-3/EGF concentration given by

$$p(x) = \frac{p_0}{2\lambda} \exp\left(-\left|\frac{x - x_{AC}}{\lambda}\right|\right), \tag{3.5}$$

where $p_0 = \int_{-\infty}^{\infty} p(x)dx$ is the total amount of LIN-3/EGF secreted by the AC, λ is the decay length of the LIN-3/EGF gradient and x_{AC} is the AC position. Furthermore, for both models we assume that the LIN-3/EGF gradient is sensed and migration forces are produced at the basal VPC surface. We can calculate f_α, the migration force produced by cell α, as $f_\alpha = \Phi_\alpha \delta_{\Phi_\alpha} \sum_{ij}(\bar{F}_A^{ij} + \bar{F}_\gamma^{ij} + \bar{F}_{\text{mig}}^{ij})$. For both the M-A and the G-S models, this yields the same expression

$$f_\alpha = \Phi_\alpha[p(x_P^0) - p(x_A^0)], \tag{3.6}$$

where x_A^0 and x_P^0 are the anterior and posterior basal vertices of cell α. Based on our experimental results in Figures 3.1, 3.4, we assume that Φ_α depends on Ras activation level ϕ_α as $\Phi_\alpha = f_0\phi_\alpha$, where f_0 is the VPC migration strength. Because it is not known how LIN-3/EGF or the Ras pathway control cell migration, we assume that Ras activation depends cooperatively on the external LIN-3/EGF signal $p(x)$ through a standard Hill curve given by

$$\phi_\alpha = \frac{p(R_\alpha)^n}{K_p^n + p(R_\alpha)^n + K_S S_\alpha}, \tag{3.7}$$

where K_p is the dissociation constant, n is the Hill coefficient, and $R_\alpha = (1/2)(\bar{r}_\alpha^0 + \bar{r}_{\alpha+1}^0)$ is the center of the basal surface of the cell. Notch signaling from neighboring VPCs inhibits LIN-3/EGF induction [20, 51] and this is implemented in equation 3.7 by the term $K_S S_\alpha$, with S_α indicating the amount of Notch signal received by cell α and $K_S = 0$ corresponding to a model without Notch signaling. While expression of Notch ligands is induced by LIN-3/EGF signaling, all VPCs express Notch receptors, which can be activated by Notch ligands from neighboring VPCs [8]. Therefore, we assume that the activation of Notch signaling in cell α depends on the level of LIN-3/EGF induction in the neighboring VPCs $\alpha + 1$ and $\alpha - 1$ as

$$\frac{dS_\alpha}{dt} = b_S\left(\frac{\phi_{\alpha-1} + \phi_{\alpha+1}}{2} - S_\alpha\right), \tag{3.8}$$

where b_S is the rate of spontaneous Notch signal deactivation. In this picture, S_α corresponds to the fraction of activated Notch receptors and K_S to the Notch signaling strength, i.e. the amount of inhibition of Ras activation per activated Notch receptor. The full equations of motion of the A-M and G-S models as well as values of all parameters are discussed next.

Vertex model of VPC shape without migration

In the so-called vertex models, cells are represented by polygons with edges corresponding to the cell membrane [33]. In such models, cell deformation and cell movement are described entirely by movement of vertices. Following the standard approach to modeling epithelial sheets, we reduce the complexity of the model by treating cells as two-dimensional entities,

thereby considering only dynamics along the antero-posterior (A-P) and apico-basal (Ap-Ba) axes Figure S3.5A. In this picture, the shape and position of N VPCs are determined by $2(N+1)$ vertices $\bar{r}_i^j = (x_i^j, y_i^j)$ where $i = 0, ..., N$ and $j = 0, 1$ correspond to the basal and apical vertices respectively. In this description, the center of mass $\bar{R}_\alpha$ of cell α is given by

$$\bar{R}_\alpha = \frac{1}{4} \sum_{i=\alpha,\alpha+1} \sum_{j=0,1} \bar{r}_i^j. \tag{3.9}$$

To derive the elastic cell area force $\bar{F}_A^{ij}$ from the energy function in equation 5.1, we calculated the cell area from the positions of the vertices that constitute the cell as

$$A_\alpha = \frac{\bar{r}_\alpha^0 \times \bar{r}_{\alpha+1}^0}{2} + \frac{\bar{r}_{\alpha+1}^0 \times \bar{r}_{\alpha+1}^1}{2} + \frac{\bar{r}_{\alpha+1}^1 \times \bar{r}_\alpha^1}{2} + \frac{\bar{r}_\alpha^1 \times \bar{r}_\alpha^0}{2}, \tag{3.10}$$

where $\bar{a} \times \bar{b} = a_x b_y - a_y b_x$. Using this, we find that

$$\bar{F}_A^{i0} = K(A_{i-1} - A_{i-1}^0)(\bar{r}_{i-1}^0 - \bar{r}_i^1)^\perp + K(A_i - A_i^0)(\bar{r}_i^1 - \bar{r}_{i+1}^0)^\perp, \tag{3.11}$$

and

$$\bar{F}_A^{i1} = K(A_{i-1} - A_{i-1}^0)(\bar{r}_i^0 - \bar{r}_{i-1}^1)^\perp + K(A_i - A_i^0)(\bar{r}_{i+1}^1 - \bar{r}_i^0)^\perp, \tag{3.12}$$

where $\bar{a}^\perp = (-a_y, a_x)$.

To derive the line tension force $\bar{F}_\gamma^{ij}$, we used the following expression for the total line tension calculated

$$\gamma_\alpha = \gamma_\perp \sum_{i=\alpha,\alpha+1} |\bar{r}_i^0 - \bar{r}_i^1| + \gamma_\parallel \sum_{j=0,1} |\bar{r}_\alpha^j - \bar{r}_{\alpha+1}^j|, \tag{3.13}$$

where $\gamma_\perp$ and $\gamma_\parallel$ are the line tensions in the Ap-Ba and A-P directions respectively. Using this, we arrive at

$$\bar{F}_\gamma^{i0} = \gamma_\parallel \left(\frac{\bar{r}_i^0 - \bar{r}_{i-1}^0}{|\bar{r}_i^0 - \bar{r}_{i-1}^0|} + \frac{\bar{r}_i^0 - \bar{r}_{i+1}^0}{|\bar{r}_i^0 - \bar{r}_{i+1}^0|} \right) + \gamma_\perp \frac{\bar{r}_i^1 - \bar{r}_i^0}{|\bar{r}_i^1 - \bar{r}_i^0|}, \tag{3.14}$$

and

$$\bar{F}_\gamma^{i1} = \gamma_\parallel \left(\frac{\bar{r}_i^1 - \bar{r}_{i-1}^1}{|\bar{r}_i^1 - \bar{r}_{i-1}^1|} + \frac{\bar{r}_i^1 - \bar{r}_{i+1}^1}{|\bar{r}_i^1 - \bar{r}_{i+1}^1|} \right) + \gamma_\perp \frac{\bar{r}_i^0 - \bar{r}_i^1}{|\bar{r}_i^0 - \bar{r}_i^1|}. \tag{3.15}$$

To implement constraints in deformation due to the presence of the gonad on the basal side of VPCs, we assume that basal vertices $\bar{r}_i^0$ are constrained to move along the A-P axis, corresponding to the x direction in our model. Hence

$$\mu \frac{d\bar{r}_i^0}{dt} = \left[(\bar{F}_A^{i0} + \bar{F}_\gamma^{i0} + \bar{F}_{\mathrm{mig}}^{i0}) \cdot \hat{e}_x \right] \hat{e}_x, \tag{3.16}$$

where $\hat{e}_x$ is the unit vector in the x direction. Finally, we assume that the VPCs are attached to fixed outer boundaries, reflecting the constraints to movement imposed by the rest of the animal's body. This is implemented by imposing that the vertices at the outer A-P boundaries do not move, i.e.

$$\frac{d\bar{r}_0^j}{dt} = \frac{d\bar{r}_N^j}{dt} = 0. \tag{3.17}$$

Vertex model of VPC migration by attractant maximization

In tissue modeling approaches that rely on energy functions, such as vertex and cellular Potts models, cell migration in a gradient of chemoattractant is often implemented by adding a term to the energy function in equation 5.1 that decreases the energy with increasing concentration of the chemoattractant, i.e.

$$E_{\mathrm{mig}} = -\sum_\alpha \Phi_\alpha \int_{\substack{\mathrm{Basal} \\ \mathrm{surface}}} p(\bar{r}) dr, \tag{3.18}$$

where the energy is proportional to chemoattractant concentration $p(\bar{r})$ integrated over the basal surface of the VPC, and Φ_α is a coupling constant that indicates how strongly each individual cell responds to the chemoattractant signal. In such a description, cells change their shape and position to maximize the chemoattractant concentration integrated over their cell surface or volume, causing cells to move in the direction of increasing chemoattractant concentration [34]. The migration force $\bar{F}_{\mathrm{mig}}^{ij}$ on vertex $\bar{r}_i^j$

is given by $\bar{F}^{ij}_{\mathrm{mig}} = -\partial_{\bar{r}^j_i} \bar{E}_{\mathrm{mig}}$. For simplicity, we assume that the chemoattractant concentration $p(x)$ only depends on the distance x along the A-P axis, corresponding here to the x axis. In addition, we assume that migration forces are only produced on the basal surface, corresponding to the vertices $\bar{r}^0_i$. This results in

$$\bar{F}^{ij}_{\mathrm{mig}} = -\delta_{j0} \sum_\alpha \Phi_\alpha \frac{\partial}{\partial x^j_i} \int\limits_{x^j_\alpha}^{x^j_{\alpha+1}} p(x)dx \; \hat{e}_x, \qquad (3.19)$$

which reduces to the expression for the migration of force in equation 5.3. The total migration force produced by a cell α is defined as $\bar{f}_\alpha = \Phi_\alpha \delta_{\Phi_\alpha} \sum_{i,j} \bar{F}^{ij}_{\mathrm{mig}}$, giving rise to equation 3.6. Equation 5.3 shows that for the attractant maximization mechanism, movement of vertices at the interfaces between cells α and $\alpha - 1$ requires that $\Phi_{\alpha-1} \neq \Phi_\alpha$. In practice, this means that in the presence of fixed outer boundaries (equation 3.17), movement and deformation of cells only occurs if Φ_α varies between cells. In addition, equation 5.3 can be interpreted as the sum of two forces acting on vertex $\bar{r}^j_i$, one produced by cell α and one by cell $\alpha - 1$. Comparing the sign of the forces shows that they always point outward from the cell. As a consequence, if cell α responds more strongly to the chemoattractant than its neighbors ($\Phi_\alpha > \Phi_{\alpha+1}, \Phi_{\alpha+1}$), it will by definition expand along the direction of the gradient while contracting in the orthogonal direction in order to maximize the overlap between the cell surface and the attractant.

Vertex model of VPC migration by gradient sensing

An alternative approach to modeling migration in a chemoattractant gradient is gradient sensing [35]. In this picture, cell measure the external attractant gradient over the surface of the cell, e.g. by comparing attractant concentration at the front and the back of the cell. Such measurements then lead to an internal polarization of signaling proteins, ultimately giving rise to migration towards high chemoattractant concentrations. Here, we do not explicitly take into account the internal polarization machinery, but make the simplest assumption that the migratory force is proportional to the change in concentration integrated over the surface of the cell, and pointing in the direction of steepest increase in attractant [35], resulting in equation 5.4. The expression for the total migration force produced by cell α, defined as $\bar{f}_\alpha = \Phi_\alpha \delta_{\Phi_\alpha} \sum_{i,j} \bar{F}^{ij}_{\mathrm{mig}}$ is identical to that of the attractant maximization model (equation 3.6). As in the attractant maximization model, equation

5.4 shows that the force on vertex $\bar{r}_i^j$ can again be interpreted as the sum of two migration forces, produced by cells α and $\alpha - 1$. In contrast to the attractant maximization model, equation 5.4 shows that the migration force produced by each cell has the same direction and magnitude for each vertex in that cell. As a consequence, cells do not expand along the direction of the gradient in response to the chemoattractant.

Expressions for chemoattractant gradient and coupling constant

For both the attractant maximization and the gradient sensing models, we assume that the chemoattractant forms an exponential concentration gradient that depends only on the distance x to the AC along the A-P axis (equation 3.5). For the attractant maximization model, we already showed that Φ_α needs to vary between cells to result in VPC movement, even for a non-uniform attractant profile $p(x)$. In the gradient sensing model, movement also arises for constant Φ_α when $p(x)$ is non-uniform. However, to reproduce our experimental data we found that for both models we have to make Φ_α dependent on the distance to the AC (Figure S3.6). Our experiments show that the propensity to migrate depends on the presence of LIN-3/EGF (Figures 3.1F, 3.1I). Moreover, we find a correlation between VPC displacement and Notch ligand expression levels (Figures 3.4A – 3.4C), with Notch ligand expression itself being a measure of the level of LIN-3/EGF induction [21]. The simplest picture consistent with these observations is one in which $p(x)$ corresponds to the LIN-3/EGF gradient and Φ_α is proportional to the amount of Ras signaling in cell α at positon x. Specifically, we assume that $\Phi_\alpha = f_0 \phi_\alpha$, where f_0 is a parameter that describes how much force is produced for a given level of Ras activation ϕ_α. For simplicity, we assume that ϕ_α depends on the external LIN-3/EGF concentration $p(x)$ through a Hill curve (equation 3.7). We find similar dynamics when ϕ_α is proportional to the integral of $p(x)$ over the basal surface of the cell (data not shown). We incorporated Notch signaling by adding an inhibitory term to equation 3.7 that corresponds to the strength of the Notch signal received by cell α.

Parameters and simulations

We simulate $N = 9$ cells, which would in our picture correspond to P(2–10).p, with only minor deformations seen in the most distal VPCs for parameters used here. To accurately capture the shape of VPCs, we estimated the aspect ratio ρ of the cell body in the A-P and Ap-Ba directions from the limited experimental data available [52–54] and found a

value of $\rho \approx 10$, meaning the cell dimension in the A-P direction was ρ times larger than in the dimension in the Ap-Ba direction. We fixed the preferred VPC area to $A^0 = 1$. Then, the undeformed VPC length in the A-P direction L_0 is given by $L_0 = \sqrt{A^0 \rho}$. Furthermore, for the line tensions $\gamma_\perp$ and $\gamma_\parallel$ of the edges in the Ap-Ba and A-P directions respectively, we assume that $\gamma_\perp = \rho \gamma_\parallel$. This assures that VPCs have the correct aspect ratio without being stretched by their connection to the fixed outer boundary: if this connection would be severed, i.e. equation 3.17 would not hold, VPCs would maintain the correct aspect ratio in absence of a chemoattractant cue. The remaining mechanical parameters, K and $\gamma_\parallel$, were tuned to reproduce the qualitative VPC configurations in Figure 3.4C and the shape of the diagram in Figure 3.4D. In particular, we chose K so that the deviation in cell area from A^0 was less than 3% through the simulation. Otherwise, varying these parameters most strongly impacted the magnitude of the deformations upon induction.

The LIN-3/EGF level p_0 and the decay length λ play analogous roles, i.e. increasing either one of them increases the range of induction. We chose here to vary p_0 since the main difference between wild-type animals and the *lin-3* and *lin-12* mutants studied is likely the LIN-3/EGF level rather than the decay length. We chose a decay length λ comparable to the length of the VPC body along the A-P axis, which is $L_0 \approx 3.2$ for our choice of parameters. The parameters λ, K_P and n were chosen to produce a force-distance curve capable of generating the configuration of two induced VPCs equidistant to the AC (Figures 3.5, S3.6). For that, we have to assume a high degree of cooperativity, $n = 5$. However, the resulting induction profile $\phi(x)$ is consistent with that measured experimentally using Notch ligand expression as a marker of induction by LIN-3/EGF [21]. Here, for simplicity we use a Hill curve to generate this induction profile. However, qualitatively similar induction curves can be generated with lower degrees of cooperativity, e.g. by taking into account saturation of EGF receptors [21] or different shapes of the LIN-3/EGF gradient. The parameter ϕ_0 determines how much force is produced for a given amount of EGF/Ras activation and magnitude of LIN-3/EGF difference measured over the VPC surface and, together with the line tensions $\gamma_\perp$ and $\gamma_\parallel$, are the main parameters controlling the amount of VPC deformation. The Notch signaling parameters K_S and b_S were chosen so that the model dynamics reproduced that observed experimentally (Figures 3.3C – 3.3E).

At the start of the simulation, the N undeformed VPCs are defined by the vertices $\bar{r}_i^j = (L_0(i - N/2)), \rho L_0 j)$. We then calculate the AC position

x_{AC} so that $R = (x_{AC} - x_\alpha^0)/(x_{\alpha+1}^0 - x_\alpha^0)$, where R is the relative AC position and the AC is positioned between VPCs α and $\alpha+1$. We solve the differential equations using the *scipy.integrate.odeint* function in Python. For the parameters used here, the dynamics of deformation are sufficiently slow and the deformations themselves sufficiently small that no topological transitions occur during the simulations.

We generally use the same parameters for the A-M and the G-S models. However, due to the difference in cell shape dynamics between the two models, some parameters had to be chosen differently to reproduce the experimental data. Below we give an overview of all parameters values used, with those parameters in the A-M model that differ from the G-S model indicated by an asterisk.

<div align="center">Mechanical parameters</div>

Parameter	Definition	Values
N	Number of cells	9
ρ	VPC aspect ratio	10
K	Area elastic modulus	1
A^0	Preferred VPC area	1
$\gamma_\parallel$	Line tension for A-P edges	0.01
μ	Mobility coefficient	1

<div align="center">EGF/Ras induction parameters</div>

Parameter	Definition	Values
p_0	Total extreted LIN-3 level	0–1.6, 0–10*
λ	LIN-3 gradient decay length	2.5, 1.9*
K_p	Activation coefficient	0.1
n	Hill coefficient	5
f_0	Migration strength	0.15, 0.05*

Notch signaling parameters

Parameter	Definition	Values
K_S	Notch signaling strength	10^{-2}
b_S	Notch signal deactivation rate	10^{-3}

3.4.4 Two-dimensional Kolmogorov-Smirnov test by bootstrapping

To compare the two-dimensional distributions in Figures 3.1D – 3.1F, Figure 3.2A, Figures 3.2C – 3.2A, and Figures 3.6A, 3.6C between different strains, we calculated P values as follows. Given two samples $\mathbb{U} = (U_1, ..., U_N)$ and $\mathbb{V} = (V_1, ..., V_M)$ with respective sizes N and M, and whose elements consist of points defined in a two-dimensional space, e.g. relative AC position versus relative expression level, we want to test the null hypothesis that both samples were drawn from the same unknown distribution. To do this, we used the two-dimensional Kolmogorov-Smirnov (K-S) test combined with a bootstrapping strategy, following [55]. We briefly outline our approach below.

The K-S test relies on a statistic D that serves as a measure of the difference between two measured distributions $P_1(x)$ and $P_2(x)$. D is generally defined as the maximum absolute difference between their two cumulative distributions. In one dimension, the cumulative distribution G of a sample is defined as $G(x) = p(X \leq x)$, which represents the probability that a variable X drawn from the sample will have a value that is less or equal than x. Then, $D = \max(|G_1(x) - G_2(x)|)$. In two dimensions, there are four ways of defining the cumulative distribution of a sample, namely $G^1(x,y) = P(X \leq x, Y \leq y)$, $G^2(x,y) = P(X \leq x, Y \geq y)$, $G^3(x,y) = P(X \geq x, Y \leq y)$, and $G^4(x,y) = P(X \geq x, Y \geq y)$, where (X,Y) is a random variable drawn from the sample. In this case, D is defined as

$$D = \max |G_1^i(x,y) - G_2^i(x,y)|, \quad \text{for } i = 1, 2, 3, 4. \qquad (3.20)$$

Practically, we compute D for the two samples $\mathbb{U}$ and $\mathbb{V}$ as follows. For each data point $U_j = (x_j, y_j)$ in $\mathbb{U}$, we calculate $D_j^{\mathbb{U}} = \max |G_{\mathbb{U}}^i(x_j, y_j) - G_{\mathbb{V}}^i(x_j, y_j)|$ for $i = 1, 2, 3, 4$. We then calculate the maximum difference between the two cumulative distributions over all data points, $D^{\mathbb{U}} = \max D_j^{\mathbb{U}}$.

Similarly, we calculate $D_j^{\mathbb{V}}$ for each data point $V_j = (x_j, y_j)$ in $\mathbb{V}$, and subsequently the maximum value over all data points, $D^{\mathbb{V}}$. The two-dimensional K-S statistic D is now given by $D = (D^{\mathbb{U}} + D^{\mathbb{V}})/2$.

To obtain the significance level or p-value, we use the following bootstrapping strategy. We concatenated both samples to obtain a pooled data set $\mathbb{W}$ of length $N + M$, i.e. $\mathbb{W} = (U_1, ..., U_N, V_1, ..., V_M)$. We then resample $\mathbb{W}$ with replacement B times, obtaining a bootstrapped sample $\widetilde{\mathbb{W}}_b = (W_1, ..., W_{N+M})$ at iteration b. Next, $\widetilde{\mathbb{W}}_b$ is divided into two samples $\widetilde{\mathbb{W}}_{b,\mathbb{U}} = (W_1, ..., W_N)$ and $\widetilde{\mathbb{W}}_{b,\mathbb{V}} = (W_{N+1}, ..., W_{N+M})$, and we compute the respective K-S statistic $\widetilde{D}_b$ as outlined above. Then, the significance level p is given by the fraction of bootstrapping iterations in which the resulting statistic $\widetilde{D}_b$ exceeds the statistic D from the original samples. That is,

$$
p = \frac{\sum\limits_{b=1}^{B} \mathrm{H}(\widetilde{D}_b - D)}{B}, \tag{3.21}
$$

where H is the Heaviside step function. For all reported p-values, we used 10^5 bootstrap samples. The p-values reported for the comparison between Figures 3.3C – 3.3D and Figure 3.6C in the main text are calculated for the underlying distributions shown in figure Figure S3.3.

3.5   Appendix

3.5.1   Author contributions to the article

GHP and JSvZ designed and conducted the experiments. JSvZ constructed the mathematical model. **GHP** and JSvZ performed simulations. **GHP** and JSvZ wrote the manuscript. JSvZ supervised the study.

3.5.2   Additional figures
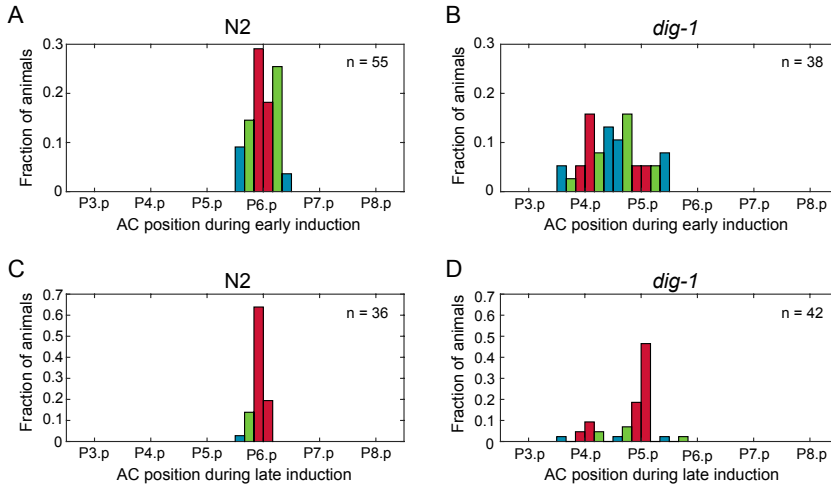
Figure S3.1 Anchor cell position.

Related to Figure 3.1

A – B Normalized AC position in N2 animals (**A**) and *dig-1* animals (**B**) for early (0–3 h) induction.

C – D Normalized AC position in N2 animals (**C**) and *dig-1* animals (**D**) for late (9–12 h) induction. The normalized AC position is defined as $R = i + (x_{AC} - x_i)/(x_{i+1} - x_i)$, where x_{AC} is the position of the AC, x_i is the position of VPC i and the index i is such that $x_i \leq x_{AC} < x_{i+1}$. The color of each bar indicates the degree of AC misplacement as defined in Figure 3.1C.
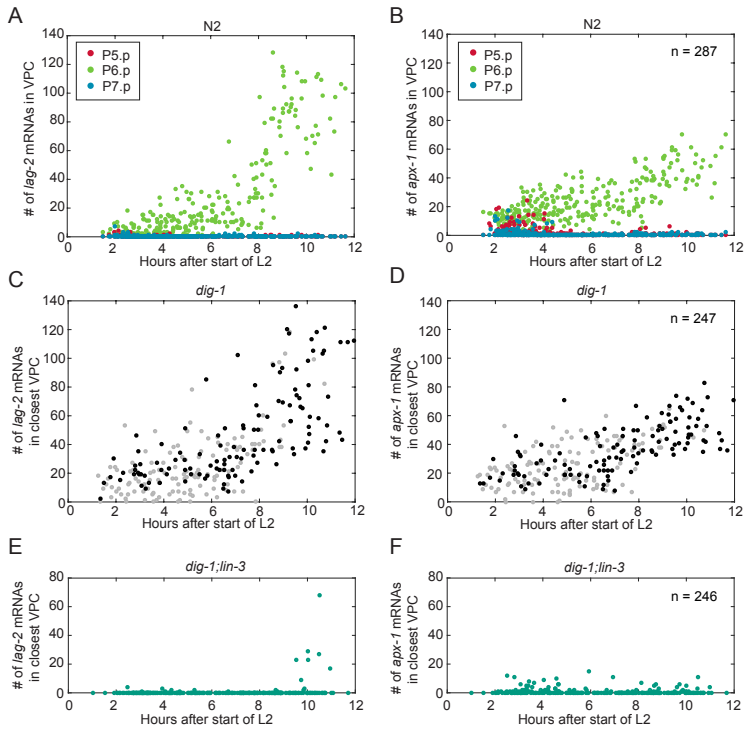
Figure S3.2 Notch ligand expression dynamics.

Related to Figures 3.2, 3.3

A – B *lag-2* (**A**) and *apx-1* (**B**) expression in wild-type animals in P5.p (red), P6.p (green), and P7.p (blue).

C – D *lag-2* (**C**) and *apx-1* (**D**) expression in *dig-1* animals in the VPC closest to the AC. Black markers correspond to animals with a properly positioned AC ($R < 0.2$, whereas gray markers correspond to animals with $R \geq 0.2$. In general, we find the expression dynamics is highly similar to that observed for N2 animals, despite being induced most often in P5.p rather than P6.p.

E – F *lag-2* (**E**) and *apx-1* (**F**) expression in *dig-1;lin-3(e1417)* animals in the VPC closest to the Ac.
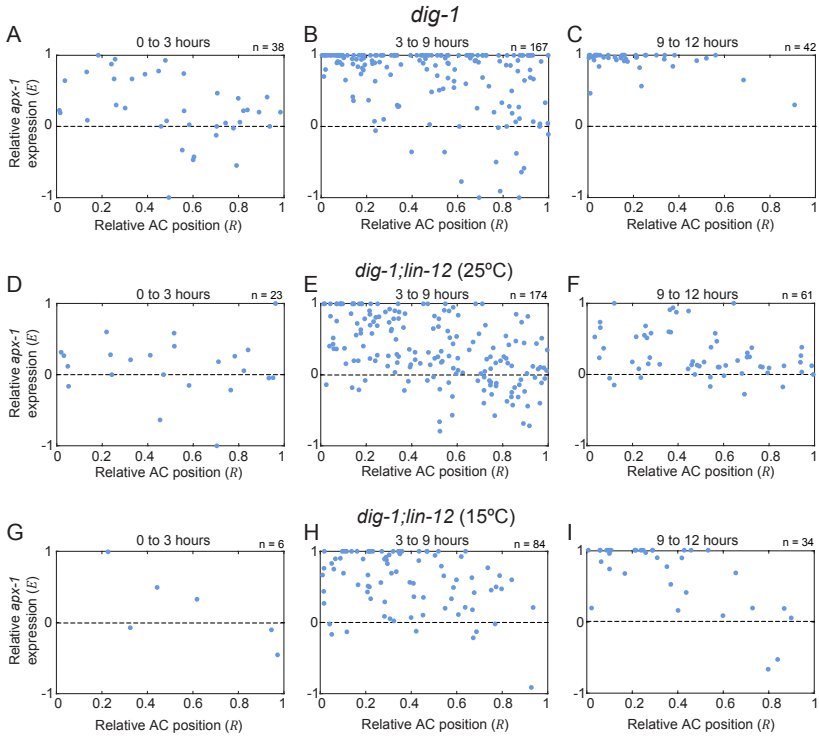
Figure S3.3 Correlation between Notch ligand expression and AC position..

Related to Figures 3.3, 3.6

A – C Relative *apx-1* level E as a function of the relative AC position R in *dig-1* animals for early (**A**, 0–3 h), middle (**B**, 3–9 h), and late (**C**, 9–12 h) induction. Each marker corresponds to a single animal.

D – F Same as **A–C** but for *dig-1;lin-12*(ts) animals at the restrictive temperature (25°C).

G – I Same as **A–C** but for *dig-1;lin-12*(ts) animals at the permissive temperature (15°C).
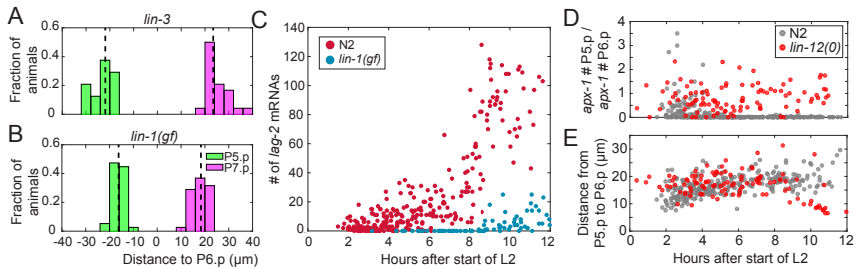
Figure S3.4 Dependence of VPC migration on 1° fate induction.

Related to Figure 3.4.

LIN-1 is a transcriptional repressor of Notch ligands that is inhibited upon activation of the Ras signaling pathway. In *lin-1(n1790gf)* mutants, all VPCs usually adopt a 3° fate and show a reduced expression of Notch ligands regardless of the presence of LIN-3. If 1° fate induction were strictly required for VPC migration, distances between VPCs in the *lin-1(gf)* mutant should resemble those in *lin-3*(e1417) mutants.

A – B Distance distributions of P5.p (green) and P7.p (magenta) to P6.p in *lin-3*(e1417) (**A**) and in *lin-1(gf)* animals (**B**). Dotted lines represent the median value of each distribution. In *lin-1(gf)* animals, P5.p and P7.p were positioned significantly closer to P6.p, indicating that the decision to migrate is made upstream of LIN-1 in the EGF/Ras pathway and, hence, can be decoupled from 1° fate induction in this particular mutant.

C *lag-2* expression in P6.p in N2 (red) and *lin-1(gf)* (blue) animals. In *lin-1(gf)*, *lag-2* expression is severely diminished, consistent with loss of 1° fate induction.

D Fraction of *apx-1* expression level in P5.p compared to P6.p for N2 (gray) and *lin-12*(0) (red) animals as a function of time.

E Distance between P5.p and P6.p for N2 (gray) and *lin-12*(0) (red) animals as a function of time. *lin-12*(0) animals already show strongly elevated expression of *apx-1* compared to wild-type animals at > 4 hours after the start of L2, whereas movement of P5.p towards P6.p (and the AC) only occurs at > 9 hours after the start of L2.

Figure S3.5 Comparison between attractant-maximization (A-M) and gradient-sensing (G-S) models.

Related to Figures 3.4, 3.5

A Definition of vertices, edges and cells for $N = 5$ cells. The position of the anchor cell is denoted by the black disk and fixed boundaries are indicated in gray. For the vertex $\bar{r}_2^1$, the different components of the area (red) and line tension (blue) forces are shown.

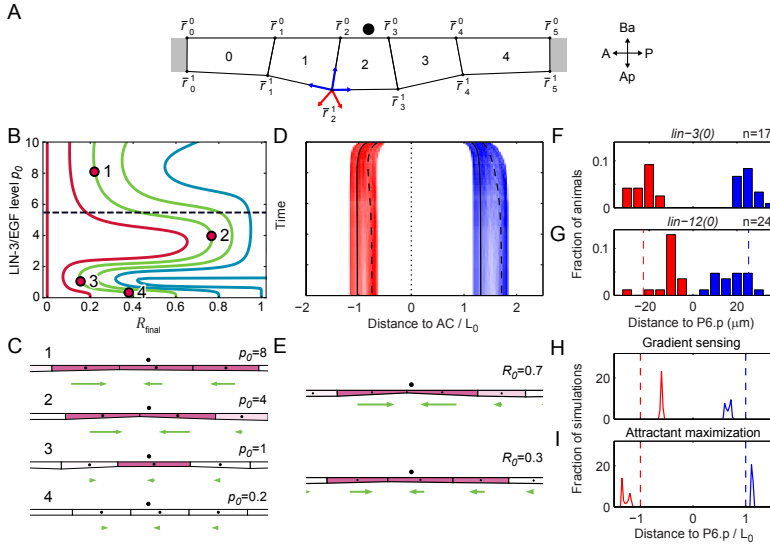**B** Diagram representing the final relative AC position R_{final} as a function of the LIN-3/EGF level p_0 for the attractant-maximization (A-M) model. Lines correspond to different initial AC positions $R_0 = 0, 0.2, 0.4, 0.6, 0.8, 1.0$ and are colored according to the initial degree of AC misplacement. Points labeled 1–4 correspond to the configurations in panel **C**. The dashed line corresponds to the value of p_0 in panels **D**, **E**, and **I**.

C Examples of different steady state configurations obtained with the model for different LIN-3/EGF levels p_0.

D Distribution of distance between P5.p (red) and P7.p (blue) to the AC as a function of time in the A-M model without Notch signaling. The distribution was calculated for $n = 1,000$ simulations with a LIN-3/EGF level of $p_0 = 1.37$ and a random initial relative AC position between $R_0 = 0$ (centered on P6.p) and $R_0 = 1$ (equidistant to P5.p and P6.p). Also shown are trajectories for individual simulations with $R_0 = 0.3$ (solid lines) and $R_0 = 0.7$ (dashed lines). Distances are given in units of the undeformed length L_0.

E Steady state model configuration for the trajectories shown in panel **D** with $R_0 = 0.3$ and $R_0 = 0.7$. Also shown are the Ac position (black circle), induction level (indicated in magenta), and the migration force (green arrow).

F – G Distribution of distances to P6.p of P5.p (red) and P7.p (blue) in the *lin-3*(e1417) (**E**) and *lin-12*(0) (**G**) mutants. The dashed lines in panel **G** indicate the average distance for P5.p (red) and P7.p (blue) in the *lin-3*(e1417) mutant.

H – I Steady state distribution distances to P6.p of P5.p (red) and P7.p (blue) for the G-S (**H**) and the A-M (**I**) models. The dashed lines indicate the distance of P5.p (red) and P7.p (blue) without induction, i.e. $p_0 = 0$.
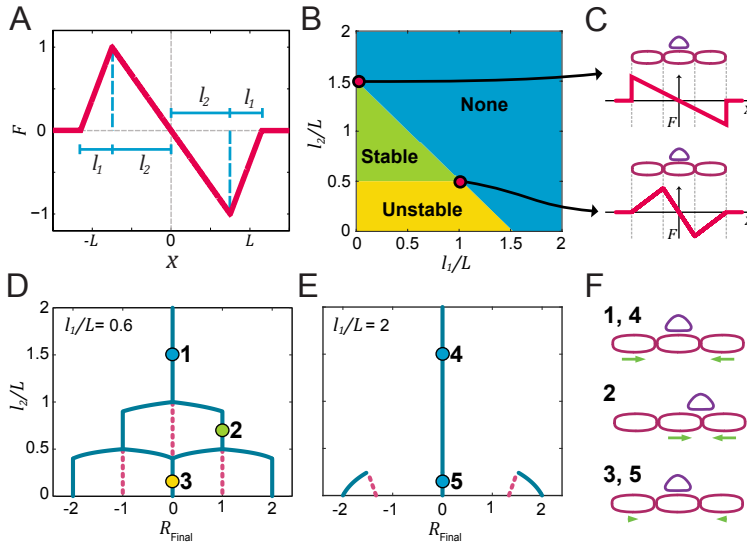
Figure S3.6 Simple model of VPC movement.

Related to Figure 3.5

A To examine what are the essential features that the force-distance curve must possess in order to reproduce the experimentally observed value $R \approx 1$ in *lin-12*(0) animals, we constructed a simplified migration model in which N undeformable cells of length L move according to a force F (red curve) consisting of a linear piecewise function defined by the parameters l_1 and l_2. This family of curves, which encompasses curves with a similar shape as that in Figure 3.5B, makes it possible to systematically examine the cell configurations generated by different force-distance curves, ranging from constant ($l_1 \gg L, l_2 = 0$) to monotonically increasing ($l_1 = 0, l_2 \gg L$). Briefly, for each cell configuration we calculate the total force by summing the individual forces for each cell, as specified by the force-distance curve. We then computationally find the fixed points at which the total force vanished, corresponding to the stable and unstable steady states of the system. Notably, for certain parameter values, the model was able to qualitatively reproduce the spatial VPC patterns observed in the vertex model, with configurations 1,2, and 3 in panel **F** being equivalent to configurations 1,2, and 3 in Figure 3.5C.

B Regions in parameter space in which $R = 1$ is either an unstable fixed point (yellow area), a stable fixed point (green area), or not a fixed point (blue area), when considering a system of three VPCs.

Figure S3.6

C Examples of force-distance curves at the limits of the parameter region where $R = 1$ is a stable fixed point (red points in panel **B**). Note that in this region, the force peaks at distances ranging from $L/2$ to $3L/2$, and the force is always null at distances larger than $3L/2$. This shows that in order to generate stable configurations with two VPCs equidistant to the AC, the force must decrease as VPCs approach the AC at distances comparable to L, and the total range over which non-zero forces are produced must be relatively narrow. The force-distance curve generated by the vertex model in Figure 3.5B fits these two criteria.

D –E Bifurcation diagrams representing the final relative AC positions R_{final} when varying l_2/L and setting l_1/L to 0.6 (**D**) and to 2 (**E**). Solid blue lines correspond to stable steady states and dashed red lines to unstable steady states. Points $1 - 5$ represent configurations obtained for different parameter regimes, with their color indicating the region of panel **B** in which they are located. In contrast to Figures 3.5D, 3.5E, the final R value does not depend on the initial AC position since VPCs are undeformable and are free to move along the A-P axis.

F Diagrams of the spatial cell configurations corresponding to points $1 - 5$ in panels **E** and **F**. Green arrows represent the forces produced by the VPCs.
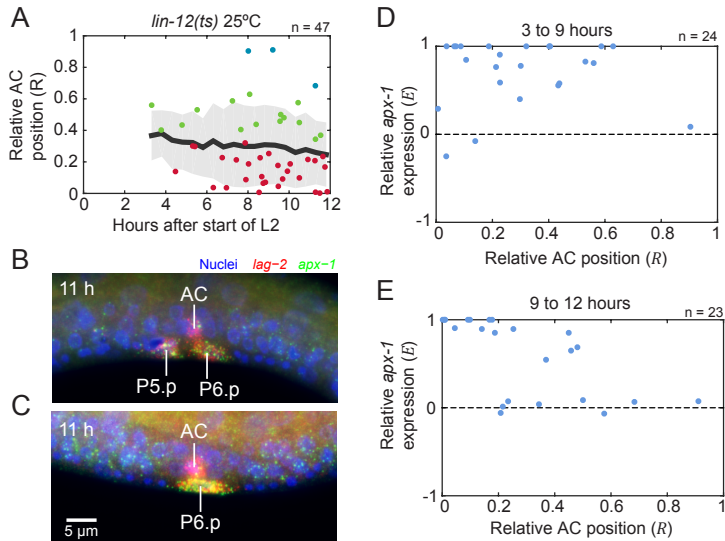
Figure S3.7 Vulva induction in the absence of Notch signaling in *lin-12(ts)*.

Related to Figure 3.6

A Relative AC position R as a function of time in the *lin-12(ts)* mutant at 25°C. In this mutant, which lacks the *dig-1* mutation, the AC is more frequently correctly positioned at the start of induction. At the end of induction, we observe animals with a severely misplaced AC ($R > 2/3$). However, we observe animals with a correctly placed AC ($R < 1/3$) more frequently than for the *dig-1;lin-12*(ts) mutants at 25°C.

B – C Examples of *dig-12(ts)* animals at 25°C in the late induction stage that show either a severely misplaced AC and two induced VPCs (**B**), or a correctly placed AC with a single induced VPC (**C**). Expression of *apx-1* (green) and *lag-2* (red) is visualized using smFISH. Nuclei (blue) are stained with DAPI.

D – E Relative *apx-1* expression level E as a function of the relative AC position R in *lin-12(ts)* animals at 25°C for middle (3–9 h, **D**) and late (9–12 h, **E**) induction. Each marker corresponds to a single animal.

Part II

Organoids as model systems for tissue renewal, homeostasis and disease

4

Introduction

Mammalian tissues and organs are highly complex structures that perform specific functions through the concerted action of multiple cells. Their large scale and their oftentimes inaccessible position within the body have posed great challenges for the study of mammalian homeostasis and disease. For decades, tissue biology has been studied through the examination of fixed tissue samples from animal models such as mice, or by the *in vitro* culture of animal- and human-derived cells. While fixed tissue allows the different cell types and the native organ architecture to be visualized, it provides little insight into the dynamics involved in organ function. In contrast, cell culture allows for real-time measurements in highly controlled environments, but usually lacks the cell type variety and spatial organization found in live tissue.

Bridging the gap between these two systems, organoids have emerged as a new tool that promises to revolutionize the future of medical and biological research. Nowadays, the term 'organoid' encompasses a wide variety of *in vitro* cultures, all sharing a common feature: being stem cell-derived three-dimensional assemblies of cells that self-renew and that recapitulate to some extent the function and architecture of an organ [56]. Therefore, organoid research exploits the ease and control that comes with *in vitro* techniques, while at the same time maintaining access to the dynamics and the complex organization of tissues. Moreover, organoids can be composed of single or multiple tissue types and can be derived from different kinds of stem cells from various animals [57], providing a flexible platform through which different aspects of organ biology, from development to adulthood, can be studied.

The organoid revolution began nearly a decade ago, when researchers
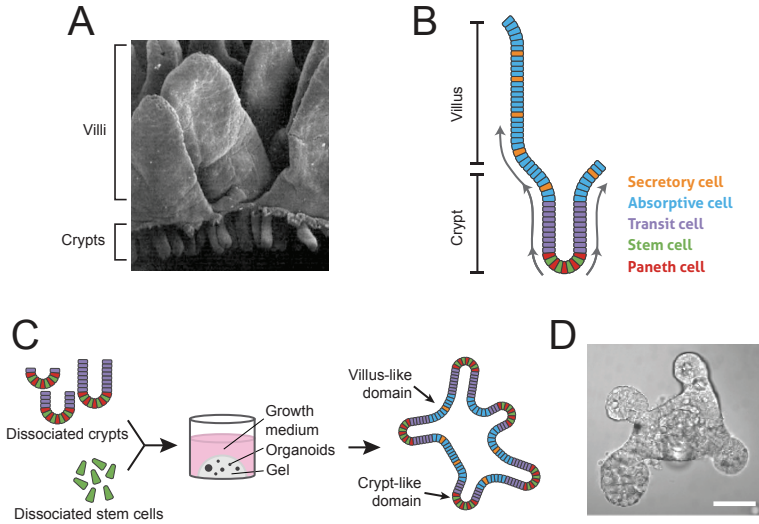
Figure 4.1 Derivation of intestinal organoids

A Scanning electron micrograph of the intestinal epithelium showing crypts and villi. Image adapted from [58].

B Cells in the intestinal epithelium are organized in a stereotypical manner. Stem and Paneth cells are localized at crypt bottoms. As stem cells divide, some of their progeny migrate upwards and enter the transit amplifying zone, where they undergo a few rounds of divisions. Then, they eventually migrate to the villus and differentiate into either absorptive or secretory cells.

C To obtain organoids, single stem cells or dissociated crypts containing stem cells obtained from intestinal tissue are seeded in a gel resembling the extracellular matrix and are overlaid with growth medium containing important growth factors to sustain stem cells. This results in the growth of three-dimensional structures that exhibit crypt- and villus-like domains and contain all cell types present in the intestine.

D Bright-field image of an intestinal organoid derived from mouse crypts. Scale bar is 50 μm.

successfully established the culture conditions for the development of murine epithelial intestinal organoids [59]. The intestinal epithelium is comprised by repetitive crypt-villus units (Figure 4.1A), with adult intestinal stem cells residing at crypt bottoms. Here, stem cells continuously divide, with some of their progeny migrating towards the villi and differentiating into the various cell types that are found in the intestine (Figure 4.1B). The continuously-cycling nature of intestinal stem cells was exploited by researchers who, upon embedding isolated stem cells or dissociated crypts in

a gel that resembles the extracellular matrix and overlaying with medium containing important signaling factors, were able to develop self-renewing organoids that mimic the crypt-villus architecture that is found in the intestine *in vivo* (Figures 4.1C, 4.1D).

Since then, organoid research has exploded, with organoid systems now available for a wide variety of tissues and with applications ranging from fundamental to applied clinical research [60]. In the next chapters, we present three studies that exemplify different ways in which organoids can be used for biological and medical research, with a special focus on the epithelial intestinal organoids described previously, and on a novel organoid system derived from human airway adult stem cells.

5

Human airway organoids to model RSV infection

Respiratory syncytial virus (RSV) is the leading cause for hospitalization due to respiratory illness; yet, effective vaccines and treatments are not available. Currently, how the epithelium of the respiratory tract responds to RSV is poorly understood. Sachs, Clevers and colleagues have developed the culture conditions that allow for the long-term expansion of airway organoids from adult human tissue and have shown that such organoids recapitulate essential aspects of RSV infection *in vivo*. Surprisingly, time-lapse images revealed that organoids become highly motile upon infection, with some of them displaying a highly coordinated rotational motion. Using a combination of single-cell tracking and mathematical modeling, we have shown that such rotational motion could be the result of an increase in cell persistence, i.e. a higher tendency for cells to maintain their direction of motion, and of cell-cell communication. Further research is necessary to confirm our hypothesis and to elucidate the potential role that such coordinated motion plays during infection.

5.1   Introduction

Respiratory syncytial virus (RSV) is the leading cause of lower respiratory tract infections among young children, accounting for 6.7% of deaths in less than one-year-old babies [61]. It is also an important cause of acute respiratory tract infections in high-risk adults, such as the elderly or immunocompromised individuals [62]. Worldwide, RSV infections represent a major burden for health systems as they are the main reason for hospitalization due to respiratory illness; yet effective vaccines have not been developed and treatment is mostly limited to supportive care [61, 63]. Palivizumab and ribavirin are two currently available medications to prevent and treat RSV infections, but their high cost and the fact that they are only recommended for use in high-risk infants greatly limits their utility [63].

Most of the current knowledge regarding the human response to RSV infection has been obtained from histological studies of lung tissue from fatal cases, as well as from immortalized respiratory epithelial cell lines and animal models [64]. Unfortunately, previously established model systems have often failed to recapitulate some important aspects of human RSV infection. It is known that RSV primarily infects ciliated airway epithelial cells, and infection results in inflammation, mucous hypersecretion, syncytia formation, increased cell apoptosis and necrosis, and apical sloughing of epithelial cells, among many other pathogenic effects [63, 64]. However, how the respiratory epithelium responds to RSV infection at the single-cell level remains poorly understood.

Recently, fetal lung organoids have been developed, and they have proven to reproduce the morphological features of RSV infection [65]. However, these organoids were not able to differentiate and mature further than the equivalent to the second trimester of human gestation even after months in culture, which raises doubts about their ability to fully recapitulate infection in infant and adult tissue. Another used model for RSV infection consists of the air-liquid interface (ALI) culture of human bronchial epithelial cells [66]. This system allows for a full differentiation of the respiratory epithelial tissue; however, the technical requirements, the limited cell expansion and the long differentiation protocols greatly reduce its utility as an efficient model system [67]. Several other approaches have been recently proposed for the development of fully differentiated lung organoids or tissue *in vitro* [68]; however, none of these currently allow for long-term clonal

expansion of the respiratory epithelium from adult humans, and moreover, none have been tested as model systems for RSV infection. Sachs, Clevers and colleagues at the Hubrecht Institute have recently established the conditions required for long-term culture of airway organoids from human adult cells, and have shown that these organoids can serve to efficiently model RSV infection. Thus, these organoids provide an ideal platform for studying the single-cell response to RSV infection as well as the assessment of potential therapeutic agents.
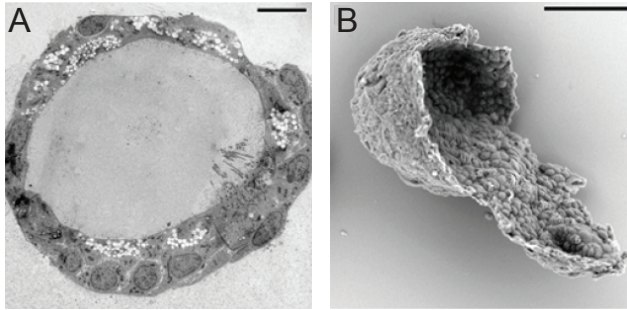
Figure 5.1 Electron micrographs of airway organoids

A Transmission electron micrograph of an airway organoid cross-section showing its polarized, pseudostratified epithelium. Scale bar is 10 μm.

B Scanning electron micrograph of a partially opened airway organoid visualizing its 3-dimensional structure. Scale bar is 50 μm.

Images obtained by Norman Sachs.

5.1.1   Establishment and infection of airway organoids

Airway organoids were developed and cultured by researchers at the Hubrecht Institute by collecting and enzymatically disrupting lung tissue from human patients, embedding isolated cells in basement membrane extract (BME), and overlaying with growth medium containing specific factors for activating or blocking signaling pathways known to be important for the airway epithelium. The organoids consisted of a polarized, pseudostratified epithelium which contained different cell types that are present in bronchiolar tissue such as basal, secretory, club, and ciliated cells (Figure 5.1). RNA sequencing and quantitative PCR revealed the presence of several airway-specific markers and confirmed that organoids retained similar

frequencies of the different cell types after more than one year in culture. Therefore, researchers concluded that the culture conditions allowed for long-term expansion of airway organoids *in vitro* while maintaining the essential characteristics of the *in vivo* epithelium.

To test whether airway organoids would serve as an *in vitro* model for RSV infection, the virus was added to a suspension of recently sheared organoids which were later seeded in BME, or alternatively, it was microinjected into individual organoids. Quantitative PCR showed an increase in RSV copies following infection, and green fluorescence was observed after a GFP-expressing virus was introduced to the culture, indicating that the virus was able to infect the organoids and to replicate (Figure 5.2A). The specificity of the host-virus interaction was confirmed since green fluorescence was not observed when organoids were pre-incubated with palivizumab, an antibody that prevents the virus from fusing to the cells (Figure 5.2B). Moreover, RSV-infected organoids recapitulated some morphological features seen after infection *in vivo*, such as actin rearrangement, apical extrusion of infected cells and syncytia formation (Figure 5.2C). Taken together, these observations suggest that airway organoids are a suitable model system to study RSV infection of lung epithelial tissue.
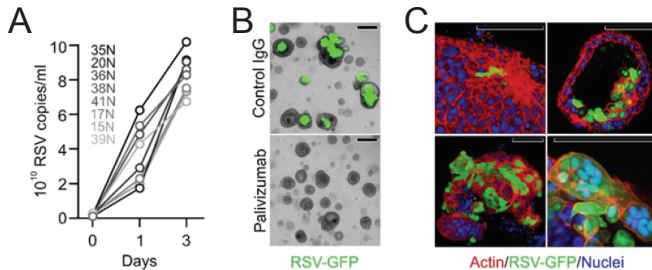
Figure 5.2 Airway organoid infection by RSV

A RSV replication kinetics for different airway organoid lines obtained by quantitative PCR.

B Phase-contrast and GFP overlays obtained five days after RSV infection. RSV-GFP is not visible after pre-incubation with palivizumab.

C Immunofluorescence images of organoids obtained three days after RSV infection showing actin rearrangments (top left), apical extrusion of infected cells (top right), organoid fusion (bottom left), and syncytia formation (bottom right.)

Data obtained by Norman Sachs.

5.1.2 Infection-induced organoid and cell motility

Time-lapse microscopy was performed in order to visualize the response to RSV infection at the level of both whole organoids and single cells. Upon infection, organoids were observed to become highly motile, with most moving rapidly through BME (Figure 5.3A), and more surprisingly, some organoids showing a strong, persistent and coordinated rotational motion (Figure 5.3B).
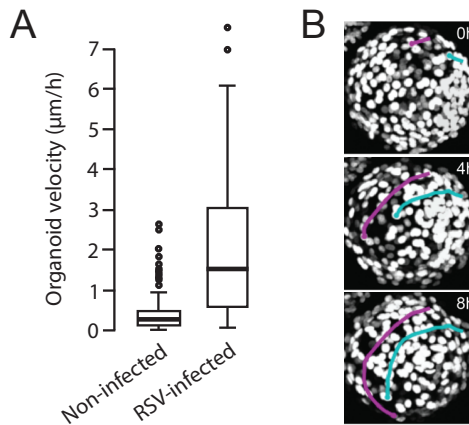
Figure 5.3 Organoid motility upon RSV infection

A Boxplot comparing organoid velocities through BME for non-infected and RSV-infected cultures. Data obtained by Norman Sachs.

B Rotational movement of an RSV-infected organoid. Tracks of two sample cells are shown through time, as obtained by cell tracking software developed by us.

Organoid and cell motility were found to be dependent on expression of the viral non-structural protein NS2. This protein has been shown to induce shedding of bronchiolar epithelial cells into the lumen *in vivo* [69], and although it is not essential for RSV replication, NS2 greatly improves virus growth in cell cultures [70]. Accordingly, an RSV variant lacking NS2 was found to replicate with low efficiencies in airway organoids. Moreover, inducible overexpression of NS2 in non-infected organoids resulted in high organoid motility comparable to that observed in RSV-infected cultures, and importantly, rotational motion of whole organoids was also detected.

Collective, coordinated cell motion is a well-studied phenomenon occurring frequently in embryonic development and cancer, and it is thought to

be triggered by external directional cues [71]. However, this idea is challenged here by the fact collective rotational movement is observed after uniform overexpression of NS2 in all cells within an organoid. It has been shown that movement of self-propelled particles can result in collective motion at larger length scales only by locally aligning their velocity [72], and when particles are constrained to move on a spherical surface, this alignment can lead to rotational motion [73]. To understand whether such a mechanism plays a role in generating collective rotational motion of RSV-infected organoids despite the absence of an external directional cue, the Zon and Tans labs at AMOLF teamed up to perform single-cell tracking and analysis, as well as mathematical modeling.

5.2   Cell tracking

To gain insight into the dynamics underlying the observed collective movement, we performed quantitative analysis on time-lapse images of RSV-infected organoids provided by researchers from the Hubrecht Institute. There, confocal microscopy was used to obtain 3D images of organoids expressing a green fluorescent marker (H2B-dendra), which allows the visualization of individual cell nuclei. Moreover, an RSV strain expressing the gene for red fluorescent protein (rrRSV) was used to inoculate the cultures, causing the cytoplasm to become fluorescent after a cell has been infected and allowing real-time tracking of the infection (Figure 5.4A, top panels).

We started by identifying two visually distinct motility categories of RSV-infected organoids in which clear, red fluorescent cells were observed. The first consisted of organoids where cell motility appeared high but was disorganized (Figure 5.4A, middle panel), while the second included those with high and coordinated cell motility that was the hallmark of rotational movement of the whole organoid (Figure 5.4A, right panel). Additionally, we defined a third category consisting of control organoids that were not inoculated with the virus (Figure 5.4A, left panel). To understand how single-cell motility correlated with whole organoid movement, we developed a custom written image analysis software that allowed us to manually track individual nuclei in 3D space and time. For each analyzed organoid, we randomly selected a few dozen cells on the initial time frame so that they uniformly covered the organoid surface. Then, we tracked each selected cell by following the center of mass of its nucleus in 3D using custom
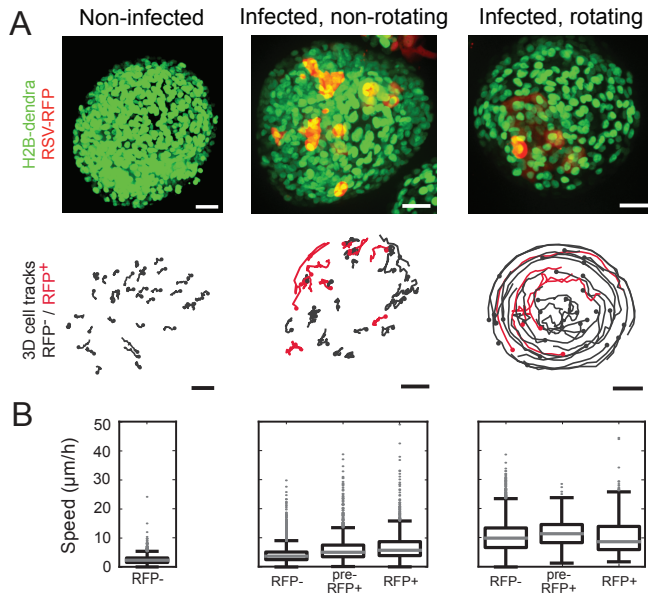
Figure 5.4 Single-cell tracking of airway organoids

A Examples of non-infected (left), RSV-infected and non-rotating (middle), and RSV-infected and rotating (right) organoids with the corresponding tracks of randomly selected nuclei (n=41,33,35 respectively). Track durations are 14 hours. Circles indicate the starting point of each track, and line color stands for either RFP$^-$ (black) or RFP$^+$ (red). Scale bars represent 25 µm.

B Boxplots of the speed distribution of every tracked nucleus at each time point for non-infected (n=3), infected but non-rotating (n=6), and infected and rotating (n=3) organoids, where 15–45 individual nuclei were tracked per organoid. For the infected organoids, nuclei were classified as RFP$^-$ when they showed no RFP signal for the duration of the track, pre-RFP$^+$ when the nuclei showed no RFP signal yet but became RFP$^+$ later, and RFP$^+$ for nuclei that showed RFP signal. In infected organoids, particularly when rotating rapidly, a small fraction of cells could not be identified between some consecutive time frames due to their fast movement, limiting our ability to track fast-moving cells. Therefore, outliers beyond 50 µm/h are likely underrepresented.

written image analysis software (Figure 5.4A, bottom panels). Cell tracks were then used to calculate cell speeds by measuring the absolute 3D displacement of each nucleus from frame to frame. To distinguish between non-infected (RFP$^-$) and infected (RFP$^+$) cells, RFP intensity was calculated by summing the pixel intensities within a disk of a radius of 5 pixels (corresponding to 2.33 μm) on the XY plane around the center of mass of the nucleus, and an intensity threshold was manually chosen so that all nuclei in non-infected organoids were categorized as RFP$^-$.

The speed distributions of cells within the three organoid categories suggested that cells are actively becoming more motile in response to RSV infection, since in general, non-infected organoids show lower speeds and less variability than infected organoids (Figure 5.4B). To explore whether RFP$^-$ and RFP$^+$ cells within infected organoids differed in motility, we classified cells at each time point as RFP$^-$ when they showed no RFP signal for the whole duration of the track, pre-RFP$^+$ when they showed no RFP signal yet but will show it later, and RFP$^+$ when they showed RFP signal (Figure 5.4B, middle and right panels). We found that the average and range of speeds in the two classes of infected organoids is similar for RFP$^-$ and RFP$^+$ cells. In addition, we found no change in average speed or in the range of speeds for cells that start to express RFP between the period when they are not yet expressing RFP (pre-RFP$^+$) and when they express it (RFP$^+$). These results suggest that cell speed does not strongly correlate with RFP expression, but rather depends on whether the organoid itself has been infected.

While the range of speeds is similar for all cell classes in both types of infected organoids, there is a slight increase in the average speed from non-rotating to rotating organoids. However, it is not clear whether such increase is the cause or rather the effect of the collective cell motion that gives rise to whole-organoid rotation.

5.3   Mathematical modeling

To understand how local interactions between single cells can give rise to collective rotational motion at the organoid level without the presence of an external cue, we built a mathematical model of migrating cells inspired by the model developed by Sknepnek and Henkes [73]. Our model assumes
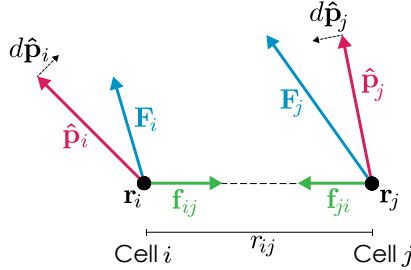
Figure 5.5 Intrinsic and adhesive forces acting on cells

Cell i, located at position $\boldsymbol{r}_i$, produces an intrinsic migratory force in the direction of its polarity vector $\hat{\boldsymbol{p}}_i$ and feels a harmonic force $\boldsymbol{f}_{ij}$ that depends on the distance r_{ij} to its neighbor, cell j. Hence, the total force $\boldsymbol{F}_i$ acting on the cell corresponds to the sum of the migratory and the adhesive forces. In addition, the cell tends to change its polarity direction to match the direction of the total force acting on it ($d\hat{\boldsymbol{p}}_i$).

that cells are point particles that move on the surface of a sphere, which mimics the organoid geometry. Each cell is a self-propelled particle with an intrinsic polarity which represents the direction of migratory force production. We assume that the polarity direction fluctuates in a stochastic manner, mimicking the random motility observed in non-infected organoids. In addition, cell movement is constrained by adhesive connections to neighboring cells, which we model as harmonic springs. Due to these adhesive constraints, the total force acting on each cell usually has a different orientation than their intrinsic polarity. Our model assumes that cells tend to change their internal polarity over time in order to align with the direction of the total force acting on them, which is crucial for neighboring cells to align their movement and result in collective motion. However, the stochastic fluctuations in the intrinsic polarity can perturb the synchronization of movement between neighboring cells.

In our model, cells are distributed uniformly over the surface of a sphere, with random orientations of their polarity vectors. The total force $\boldsymbol{F}_i$ acting on cell i is given by the sum of the migratory force in the direction of its polarity and the adhesive forces due to neighboring cells (Figure 5.5), i.e.,

$$\boldsymbol{F}_i = p_0\hat{\boldsymbol{p}}_i + \sum_j \boldsymbol{f}_{ij}, \tag{5.1}$$

where p_0 is the magnitude of the intrinsic migratory force, $\hat{\boldsymbol{p}}_i$ is a unit vector that indicates the polarity direction, and $\boldsymbol{f}_{ij}$ is the harmonic force

between cells i and j. This force is given by

$$\boldsymbol{f}_{ij} = -k(2\sigma - r_{ij})\frac{\boldsymbol{r}_j - \boldsymbol{r}_i}{r_{ij}}, \qquad (5.2)$$

where k is the spring constant, σ represents the intrinsic radius of the cell, r_{ij} is the distance between cells i and j, and $\boldsymbol{r}_i$ and $\boldsymbol{r}_j$ are their respective positions.

The model is then described fully by two sets of ordinary differential equations for the cell positions $\boldsymbol{r}_i$ and the cell polarities $\hat{\boldsymbol{p}}_i$ given by

$$\frac{d\boldsymbol{r}_i}{dt} = \mu\boldsymbol{F}_i^P, \text{ and} \qquad (5.3)$$

$$\frac{d\hat{\boldsymbol{p}}_i}{dt} = (J\delta_i + \eta\xi(t))\,(\hat{\boldsymbol{r}}_i \times \hat{\boldsymbol{p}}_i). \qquad (5.4)$$

Here, cell movement is assumed to be overdamped, with a mobility coefficient μ. $\boldsymbol{F}_i^P$ is the projection of the total force $\boldsymbol{F}_i$ onto the local plane of cell i tangent to the sphere, i.e., $\boldsymbol{F}_i^P = \boldsymbol{F}_i - (\boldsymbol{F}_i \cdot \hat{\boldsymbol{r}}_i)\hat{\boldsymbol{r}}_i$, where $\hat{\boldsymbol{r}}_i$ is the unit vector orthogonal to the surface of the sphere at $\boldsymbol{r}_i$. The polarity vector $\hat{\boldsymbol{p}}_i$ rotates with a fixed angular velocity J in the direction towards $\hat{\boldsymbol{F}}_i^P$. This direction is given by $\delta_i = \cos\theta_i/|\cos\theta_i|$, where θ_i is the angle between $\hat{\boldsymbol{p}}_i$ and $\boldsymbol{F}_i^P$. Stochastic fluctuations to the direction of the cell polarity are incorporated by the noise term $\xi(t)$, with noise strength η.

In the absence of cell-cell communication, i.e. for $J = 0$, the polarity vector $\hat{\boldsymbol{p}}_i(t)$ will undergo a random walk which will cause the polarity to deviate from its original direction over time. The correlation in polarity direction decreases in time as $\langle\hat{\boldsymbol{p}}_i(0) \cdot \hat{\boldsymbol{p}}_i(t)\rangle = \exp{-t/\tau}$, where $\tau = 2/\eta^2$ is the polarity persistence time.

5.3.1 Simulations

To generate random initial configurations of N particles distributed approximately equidistantly on a sphere, particles were first placed at random positions and then propagated using the spring force in equation 5.2 between nearest neighbors until global mechanical equilibrium was reached. At the start of each simulation, we assigned each cell i a polarity vector $\hat{\boldsymbol{p}}_i$

with a random orientation in the tangent plane of the sphere at position $\boldsymbol{r}_i$ and determined the identity of the nearest neighbors which are connected by a spring to cell i using Delauney triangulation on a sphere [74]. Equations 5.3 and 5.4 were integrated using the Euler-Maruyama method, with time step $\mu k \Delta t = 5 \times 10^{-3}$. To ensure that the position $\boldsymbol{r}_i$ and polarity vector $\hat{\boldsymbol{p}}_i$ remain well-defined throughout the simulation, after each time step we projected $\hat{\boldsymbol{p}}_i(t + \Delta t)$ onto the plane tangent to the sphere at position $\boldsymbol{r}_i(t + \Delta t)$ and normalized the position and polarity vectors. Simulations were performed on a sphere of radius $\rho = \sigma \sqrt{N/4\phi}$, where ϕ is the packing fraction, i.e. the ratio of the total area occupied by the cells to the area of the sphere. We used values of $N = 100$ and $\phi, p_0, \mu, k, \sigma = 1$, while we varied the parameters J and η.

5.3.2 Results

The model shows that when the intrinsic polarity of individual cells is persistent enough, i.e. when cells tend to maintain their direction of motion, the local alignment between neighboring cells can lead to a coordinated rotational motion at the level of the sphere (Figure 7.4A, right panels). In contrast, low and medium persistence times result in the random movement of cells with no perceptible coordinated motion, mimicking what is observed in non-infected and in infected but not rotating organoids respectively (Figure 7.4A, left and middle panels). This transition between a disorganized to an organized rotational motion upon increasing the persistence time is more notable when quantifying the total angular momentum of the cells in the spheres (Figure 7.4C and Figure 7.4D, colored markers). This transition occurs because, even though cells are producing the same force p_0, for low persistence they are often pushing in opposite directions due to the random orientation of their polarities resulting in a low overall speed, while for high persistence times, they push together in the same direction causing an increase in overall speed. The model also shows that interactions between neighboring cells are crucial for such transition to occur, even when cell motion is highly persistent (Figure 7.4C, grey line).

Interestingly, the speed distributions of particles in the model for different degrees of persistence reproduce those obtained for the three organoid motility categories analyzed previously Figure 7.4D. There is a slight increase in cell speeds between low and medium persistence times, similar to what was observed for non-infected and infected but not rotating organoids.
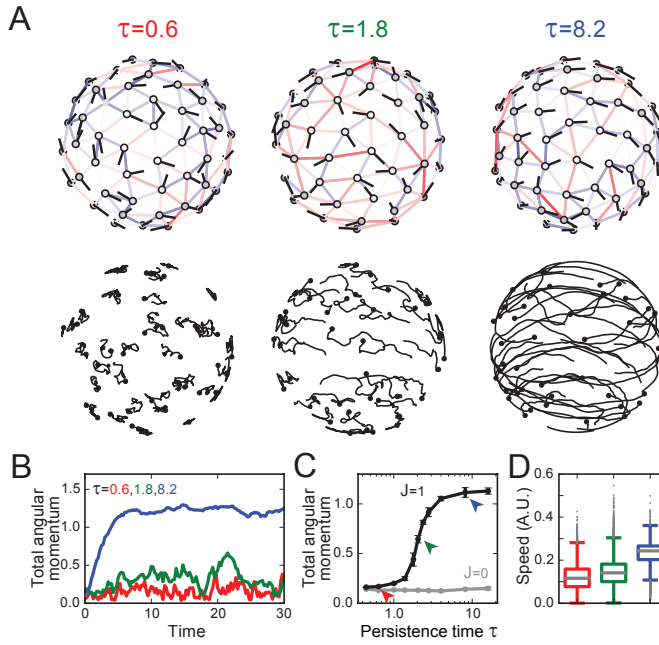
Figure 5.6 Mathematical modeling of infection-induced motility of airway organoids

A Snapshot of the cell configuration (top) and cell tracks (bottom) for simulations with N=100 cells and increasing persistence time ($\tau = 0.6, 1.8, 8.2$). The persistence time indicates the mean time over which the cell maintains its direction of polarization in the absence of cell-cell interactions. White markers represent cell centers with black lines indicating the direction of the polarization vector. Adjacent cells are connected by springs, which are shown as colored lines. Springs are red when stretched and blue when compressed. Cell tracks are shown for the same time period for all three simulations, with black circles indicating the starting position of each track.

B Total angular momentum of the cell configuration as a function of time for simulations starting with random initial distribution of polarity vectors. For sufficiently high persistence time ($\tau = 8.2$, blue line), the cells rapidly establish rotational motion.

C Total steady state angular momentum as a function of the persistence time τ for simulations with cell-cell communication ($J = 1$, black line) and without ($J = 0$, grey line). Colored arrows indicate the persistence times corresponding to the simulations in panel **B**.

C Box plots of the distribution of cell speeds for the different persistence times in panel **B**. The distribution is calculated from five independent simulations.

A higher increase in cell speeds is observed between medium and high persistence times, as is the case between infected but not rotating and infected and rotating organoids. Therefore, the model provides a potential explanation for the difference in speed between non-infected, infected but not rotating, and infected and rotating organoids, by suggesting that it results from an increase in cell persistence.

5.4   Conclusions and outlook

RSV is a leading cause of acute respiratory tract infections, causing a major burden to health systems worldwide; yet, effective vaccines and treatments have not been developed, and how epithelial cells respond to RSV is still an open question. Here, we show that the airway organoids developed in the Clevers lab provide a unique opportunity to address this question. RSV-infected organoids recapitulate important features of infection *in vivo*, and thus constitute an ideal model to study the response to RSV at the single-cell level.

We have characterized the behavior of cells in airway organoids upon RSV infection and we have developed a mathematical model that captures the essential dynamics observed in these cells. The model suggests that the different behaviors observed in non-infected and infected organoids are not due to changes in cell speed but rather due to the coordinated movement between cells that results from changes in cell-cell interactions and in cell persistence, i.e. the tendency for cells to maintain their direction of motion. However, whether RSV infection and, in particular, expression of NS2 indeed lead to stronger cell-cell interactions or to cell migration becoming more persistent is still to be determined; further research at the Zon and Tans labs will attempt to address this question. Cell migration is a process which involves the cell polarization machinery and is driven by actin polymerization [75]. Therefore, the visualization of actin and other polarity markers would allow the analysis and quantification of the migratory and polarity response of cells to infection, and could provide clues to determine whether cell persistence is increased. Moreover, the use of inhibitors for cytoskeletal and cell adhesion proteins could help uncover the essential mechanisms involved, and in particular, they could reveal whether mechanical forces are sufficient for cells to couple their movement or whether other types of interactions are required.

So far, our analysis of cells in RSV-infected organoids has been performed on time-lapse images that were started a number of days post-infection, when cell and organoid motility were already increased. Therefore, such images do not reveal the initial stages of infection, and in particular, do not show how rotation of organoids begins. In addition, due to the stochastic nature of viral infection, cells within an organoid become infected in an irregular manner and some cells might not become infected at all, which further complicates the analysis of single-cell behavior as a response to infection. Fortunately, organoid motility and rotation are also observed upon inducible overexpression of NS2 in all cells of an organoid. This provides an ideal system in which organoid motility can be triggered in a tightly controlled manner and where cell behavior can be studied before, during and after induction to reveal how the transition from uncoordinated to coordinated motion occurs and how it compares to our mathematical model.

With further research using the NS2 inducible system as well as fluorescent cytoskeletal and polarity markers, we will aim to uncover the essential mechanisms that lead to increased organoid motility as a result of RSV infection and the role that such motility plays during disease. Our results will hopefully provide a deeper understanding of the epithelial response to RSV, and will ideally offer new insights into potential treatments and preventive measures.

5.5 Appendix

5.5.1 Author contributions to the chapter

NS and colleagues from the Hubrecht Institute performed the experiments. **GHP** performed cell tracking and analysis. JSvZ and EPO constructed the mathematical model and performed simulations. **GHP** and JSvZ wrote the text. SJT and JSvZ supervised the study.

6

Effect of AFGPs on organoid survival during hypothermic storage

We studied the effects of antifreeze glycoproteins (AFGPs) on the survival of murine intestinal organoids under hypothermic conditions. We found that survival of organoids in cold conditions depends greatly on their developmental stage: mature organoids die within 24 hours of being stored at 4°C, while cystic organoids could survive for up to 48 hours. We found that in the presence of AFGPs, organoid survival was prolonged for up to 72 hours, irrespective of their developmental stage. Fluorescence microscopy experiments revealed that AFGPs predominantly localized at the cell surface and covered the cell membranes. Our findings support a mechanism in which the positive effect of AFGPs on cell survival during hypothermic storage involves the direct interaction of AFGPs with the cell membrane. Our research highlights organoids as an attractive multicellular model system for studying the action of AFGPs that bridges the gap between single-cell and whole-organ studies.

6.1   Introduction

Hypothermic preservation is a commonly-used method in which cells, tissues or organs are maintained at low temperatures (1°C – 10°C) for short-term storage situations that require distant transport. During hypothermic storage, cells encounter cold stress that affects their cell physiology, metabolic activity, and regulation of ion equilibration across membranes [76]. Much effort has been made into the optimization of storage solutions that minimize cold-induced damage and that increase the time interval that cells and organs can be cold-stored [77]. However, up to now this time interval remains limited which significantly restricts the donor organ supply, access and utility.

Numerous organisms have evolved adaptive mechanisms for their survival in fluctuating cold temperatures and icy environment [78]. Usually, these mechanisms involve the production of antifreeze proteins (AFPs) and antifreeze glycoproteins (AFGPs) [78, 79]. AF(G)Ps have the unique ability to inhibit ice recrystallization, to dynamically shape ice crystals, and to depress the freezing point of a solution in a non-colligative manner [80, 81]. In addition, several AF(G)Ps have shown promising results in applications that include the enhanced hypothermic storage of cold-sensitive cells, embryos and other biological tissues [82–85]. Rubinsky et al. showed that the fertility of bovine oocytes can be significantly improved by the addition of fish AF(G)Ps [86], and that rat livers can be stabilized at low temperatures using AF(G)Ps [87]. The effects of AF(G)Ps on hypothermic storage and cryopreservation have however been discordant and some studies have reported negligible and even adverse effects [88]. Moreover, the mechanisms by which AF(G)Ps may exert a protective effect on cells during cold storage are not understood, and a successful hypothermic storage of multicellular systems, in particular organs, is still not within reach.

So far, the mechanisms by which AF(G)Ps exert a protective action on cells during hypothermic storage is studied *in vivo*, mostly in single cells using 2D cell culture [84]. Studies on multicellular systems are typically performed on whole embryos or organs [87, 89], whose large size poses severe challenges in terms of the amount of AF(G)Ps required, and in studying the action of AF(G)Ps on the cellular and molecular level. Organoids are self-organizing three-dimensional structures that are grown from stem cells *in vitro*, which recapitulate essential features of organ architecture and function [56]. Organoids bridge the gap between traditional 2D cell

cultures and organs since they are stable cultures that allow for differentiation, cell-cell and cell-matrix interactions, and 3D organization; yet they remain easily and affordably accessible to manipulation and experimentation. Since their introduction nearly a decade ago, organoids from several tissues have been developed, starting a revolution in both the biological and medical fields. Organoids provide previously inaccessible insights into morphogenesis, stem cell biology and disease, and hold great promise for the future of personalized medicine [60, 90].

Here, we studied the survival of murine intestinal organoids under hypothermic conditions and how this survival was affected by the addition of AFGPs. We focused in AFGPs as they take up a special role among all identified AF(G)Ps. They were the first to be discovered, they have the fastest adsorption rate to ice [91], and they show a capacity to inhibit ice recrystallization that is orders of magnitude greater than any other AFP [92]. These properties make them the primary target for the development of synthetic antifreeze analogues for applications in cryopreservation [93]. In our study, we observed that AFGPs have a clear life-prolonging effect on organoids in all different developmental stages.

6.2   Results

6.2.1   Survival of intestinal organoids under hypothermic conditions

We investigated the survival rate of intestinal organoids under hypothermic conditions for different periods of time ranging from 24 to 120 hours. Individual organoids were followed and visually assessed every 24 hours to determine their viability. The visual organoid viability assessment was supported by fluorescein diacetate staining (see section 6.5). Organoids were embedded in a mixture of agarose and basement membrane extract (BME). This mixture supported growth since normal development was observed for up to three passages, and it remained solid at 4°C allowing the assessment of individual organoids over time. After the cold storage period, organoids were returned to an incubator with standard conditions (37°C and 5% CO_2) to evaluate how they recover from the hypothermic exposure. We observed considerable growth of live organoids after being rewarmed, and we used this property to distinguish between live and dead organoids. We also observed that healthy-looking crypts were able to bud
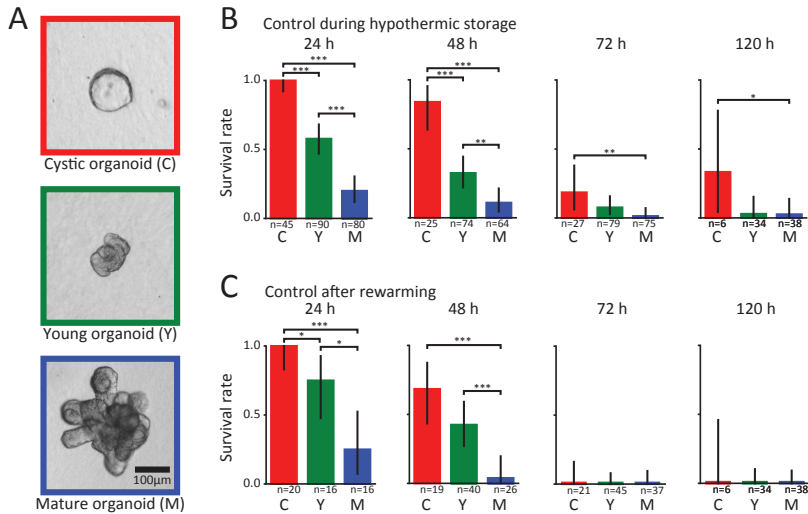
Figure 6.1 Survival of intestinal organoids under hypothermic conditions

A Classification of organoids according to their developmental stage. Cystic organoids (left panel, red) are spherical structures with a large lumen and thin walls consisting of stretched-out undifferentiated cells. Young organoids are those that are no longer spherical, have a small lumen, thick walls, and small buds rather than crypts (middle panel, green). Finally mature organoids are those in which one or more clear grown crypts are visible (right panel, blue).

B Survival rates of organoids at different developmental stages obtained from visually assessing them every 24 hours during hypothermic storage periods ranging from 24 to 120 hours. Bars show results pooled from different independent experiments.

C Corresponding survival rates obtained from a visual assessment performed two to three days after the organoids were returned to the incubator.

Asterisks denote significant differences (*: $p < 0.05$, **: $p < 0.01$, ***: $p < 0.001$).

from such organoids, suggesting that stem cells are present and would allow for organoid passaging.

Before the start of each experiment, organoids were classified according to their developmental stage as cystic, young, or mature (Figure 6.1A), in order to assess how hypothermic conditions affect each stage given that organoid complexity and composition vary greatly throughout their development. Cystic organoids are spherical structures with a large lumen and thin walls consisting of stretched-out undifferentiated cells (Figure 6.1A, left panel). Young organoids are no longer spherical, have a small lumen, thick walls and small buds without pronounced crypts (Figure 6.1A, middle

panel). Mature organoids possess one or more clear grown crypts (Figure 6.1A, right panel).

We found a remarkable dependence of developmental stage and survival in cold conditions, with most mature organoids dying within 24 hours (Figure 6.1B, blue bars) while most cystic organoids survived for up to 48 hours (Figure 6.1B, red bars). Concordantly, survival rates of young organoids were found between those of cysts and mature organoids (Figure 6.1B, green bars). Low variability between independent experiments was observed (Figure S6.3).

In most cases, assessing the survival upon return to the incubator revealed lower survival rates (Figure 6.1C), which indicated that despite being alive at 4°C, rewarming and returning to 37°C caused additional stress to the organoids.

6.2.2 AFGP increases survival of organoids under hypothermic conditions

Antifreeze proteins have been reported to protect cold-sensitive cell lines and organs from hypothermic damage. In order to evaluate whether the addition of AFGP would have an influence over organoid survival under hypothermic conditions, we repeated the previous experiments after adding 10 mg/ml of AFGP to the medium. This concentration was chosen as it had shown protective effects in previous studies on cells [84]. We also performed control experiments in which we added the non-antifreeze protein α-lactalbumin to the growth medium. We chose α-lactalbumin as the control protein as it has a similar size to AFGP, it shows no antifreeze activity, and albumins have been used as control proteins in previous AF(G)P studies [84, 94].

We found that the addition of AFGP to the medium had a beneficial effect on organoid survival at all developmental stages. Assessing viability every 24 hours during the hypothermic storage experiments revealed that 100% of organoids remained alive for up to 48 hours (Figure 6.2A, top two panels). Survival decreased slightly afterwards but remained above 80% even after 120 hours in cold conditions (Figure 6.2A, bottom panel). We also observed low variability between independent experiments (Figure S6.3).

As before, survival rates after return to the incubator were lower, reit-
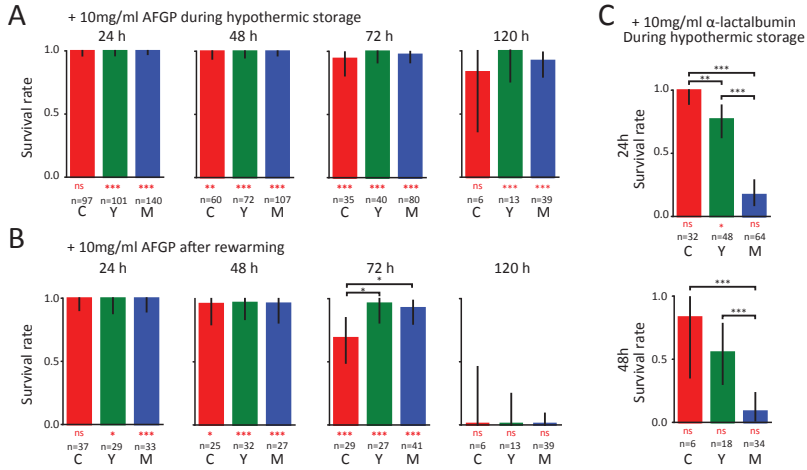
Figure 6.2 AFGP increases survival of organoids under hypothermics conditions

A Survival rates of organoids at the different developmental stages defined in Figure 6.1A when AFGP was added to the growth medium. Rates were obtained from visually assessing the organoids every 24 hours during hypothermic storage periods ranging from 24 to 120 hours. Bars show results pooled from different independent experiments.

B Corresponding survival rates obtained from a visual assessment performed two to three days after the organoids were returned to the incubator.

C Survival rates obtained from assessing organoids after 24 and 48 hours of hypothermic storage with the addition of α-lactalbumin to the growth medium.

Black asterisks denote significant differences between developmental stages and red asterisks below bars denote differences from controls in Figure 6.1 (*: $p < 0.05$,**: $p < 0.01$, ***: $p < 0.001$, ns: not significant).

erating the additional stress to which organoids are subjected when being rewarmed (Figure 6.2B). Still, 100% of organoids were alive after a cold storage period of 24 hours, and this value decreased slightly to ∼96% after 48 hours. At 72 hours, survival rates remained above 93% for young and mature organoids while the rate dropped to 69% for cystic organoids. Finally, no surviving organoids were observed after 120 hours.

In contrast to the beneficial effect of AFGPs, we found that α-lactalbumin did not provide any protection against hypothermic stress (Figure 6.2C), as survival rates were comparable to those observed with no added proteins (Figure 6.1B, top two panels).

6.2.3   AFGP localizes to cell membranes

Fluorescence microscopy was used to obtain mechanistic insights into the role of AFGP on organoid survival. We added 0.5 mg/ml of FITC-AFGP to the medium, incubated at 37°C for one hour and then imaged the organoids at room temperature. We found that the labeled AFGP was predominantly present on cell outlines (Figure 6.3A, middle panel), suggesting that AFGP preferably localizes to cell membranes. We found that washing the organoids with PBS resulted in the vanishing of the observed fluorescent pattern (Figure 6.3A, right panel). This observation suggests that AFGPs are loosely bound and are not inserted into the membrane. Control experiments using only the fluorescein dye showed no fluorescent pattern, indicating that the AFGP is responsible for the membrane localization (Figure 6.3B).

6.3   Discussion

Hypothermic storage of cells causes cold stress that affects the cell physiology, metabolic activity, and regulation of ion equilibration across membranes [76]. We observed a statistically significant dependence on organoid survival after hypothermic storage and their developmental stage, with more mature organoids showing much lower viability rates than cystic organoids. Hypothermic storage likely activates different sets of stress pathways that are cell and tissue specific. Cystic organoids are composed of cells that strongly differ from the cells in mature organoids. Cystic organoids, sometimes referred to as "enterospheres", consist of undifferentiated cells with stem-cell-like properties. These differ from mature intestinal stem cells in that they have a distinct set of gene expression patterns as well as different sets of active signaling pathways [95–97]. These characteristics suggest that cysts recapitulate some features of intestinal tissue under a state of repair after injury [95, 98]. In contrast, mature organoids are mostly composed of fully differentiated secretory and absorptive cells with a smaller percentage of stem and progenitor cells, which resemble the intestinal tissue in a homeostatic state. The distinct cell identities and functions in both cystic and mature organoids likely result in differences in their ability to respond to stress during and after hypothermic storage. Young organoids are likely to contain subsets of both cystic and mature properties, thus explaining their intermediate survival rates.
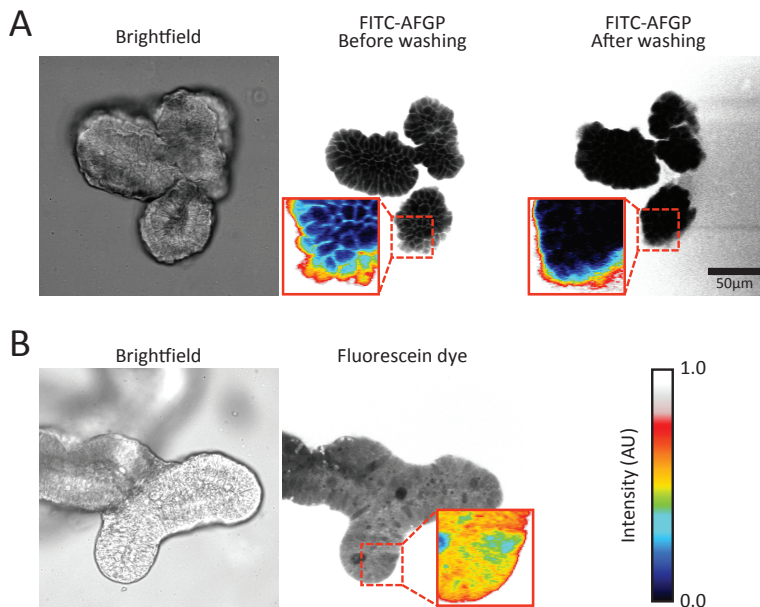
Figure 6.3 AFGP localizes to cell membranes

A Bright-field and fluorescence images of an organoid with FITC-AFGP. When imaged before washing the medium containing AFGPs (middle panel), fluorescence is observed on cell outlines. After washing the imaging wells, the fluorescence pattern is not observed (right panel).

B Bright-field and fluorescence images of an organoid with fluorescein dye. Fluorescence is not localized to cell outlines, but it is present in the cytoplasm of most cells.

Pixel intensities are colored in insets to highlight the observed fluorescence patterns. Colors represent the same intensities in all images.

The characteristic shape and behavior of cystic organoids (a round and enlarged lumen, thin walls formed by stretched-out cells, and occasional rapid contractions observed after expulsion of material from the lumen) suggest that they are under high intraluminal pressure due to accumulation of fluid within the lumen. This cystic morphology has been documented when organoids swell as a result of adding forskolin [99], or cholera toxin [100] to the medium. Furthermore, addition of the signaling factor Wnt3a results in organoids adopting a cystic morphology as well as their cells assuming an undifferentiated state [101]. In all cases, the cystic organoid morphology has been linked to an increased chloride secretion by the CFTR ion channel, which in turn causes increased fluid secretion into the lumen. This suggests that ion transport in cystic organoids is highly dynamic compared to more mature organoids. We speculate that as a result, ion leakage caused by hypothermic storage has a smaller impact on cysts in comparison to young and mature organoids, accounting for their higher survival rates.

We found that the addition of AFGPs to the medium had a statistically significant positive effect on the cold survival of organoids, which is in line with previous studies [85]. Current mechanisms that explain the positive effect of AFPs on the cold survival of cells involve the blockage or alteration of the flow of ions into cells [102, 103], and the protection of cell membranes as they pass through their phase transition temperatures [104, 105]. Tomczak et al. proposed that AFGPs may form a monolayer covering the membrane surface, thereby reducing the leakage of ions across the membrane as it is cooled through its thermal transition temperature [105]. Using fluorescence microscopy, we found strong evidence that AFGPs localize at the cell surface, suggesting that the protection mechanism of AFGPs is indeed closely connected to their interaction with the cell membranes. From the obtained fluorescence data we cannot infer whether AFGPs target specific ion channels. We observed that AFGPs loosely interact with cell membranes of the organoids and found that AFGPs do not only cover model membranes but entire multicellular systems.

Interestingly, we further observe that upon rewarming, the survival rate remains high (93%) for young and mature organoids, while it drops (69%) for cystic organoids in the presence of AFGPs after 72 hours at 4°C. Garnet et al. showed that AFGPs interact with a model membrane at both 5°C and 30°C, but that the interaction is much weaker at 30°C [106]. We speculate that the distinct cell identities in cystic and more mature organoids do not only affect their ability to respond to stress during hypothermic storage but also to stress experienced during rewarming. More mature organoids could,

for instance have a different membrane composition with more phosphate groups. Such groups could enable a better interaction with the AFGPs and a prolonged protection. Clearly, the response to rewarming stress must also be considered when investigating potential AFGP applications for the storage of cells and tissues in the cold for medical purposes.

6.4 Conclusions

In conclusion, our research shows that organoids are attractive model systems to study the action of AF(G)Ps during and after hypothermic storage. Moreover, they provide a flexible and previously inaccessible way of studying the effects of cryopreservation in multicellular systems, which could bring us a step closer to cryopreservation of entire organs. We have found clear evidence that AFGPs have a strong positive effect on the survival of organoids during and after hypothermic storage at 4°C. If this protection against hypothermia-related perturbations could be extended for even longer periods and to complete intestinal organs, then it would have enormous practical implications for the transfer and storage of organs.

6.5 Materials and methods

6.5.1 AGFP purification

Antifreeze glycoproteins were purified from the Antarctic toothfish *Dissostichus mawsoni* and fluorescently labeled using fluorescein isothiocyanate (FITC) as described previously [107].

6.5.2 Organoid culture

Intestinal organoids isolated from C57BL/6 mice were a gift from Norman Sachs (Hubrecht Institute, The Netherlands). Organoid culture was performed according to previously described protocols [108] with slight variations. In short, organoids were embedded in basement membrane

extract (BME, 3533-010-02, Trevingen) droplets and overlaid with Intes-tiCult Growth Medium (#06005, STEMCELL Technologies), which was changed every two to three days. Organoid passaging was performed by mechanically dissociating crypts using a narrowed glass pipette.

6.5.3 Hypothermic storage

For cold storage experiments, organoids were embedded in a mixture of two thirds BME and one third 0.5% agarose (438792U, VWR Chemicals). Agarose was added to prevent BME from disintegrating, as BME becomes liquid at temperatures $\sim$ 4°C. After mechanical dissociation, crypts were resuspended in cold BME. Then, molten agarose was allowed to cool down to 37°C and was added to the suspension, which was quickly mixed and immediately plated in a pre-warmed 24-well plate (time is of the essence as the agarose becomes solid very soon after coming into contact with the cold BME). The droplets were left to solidify for 25 minutes at room temperature, after which room temperature growth medium was added and the plate was moved to the incubator.

Cold storage experiments were started two to three days after plat-ing the organoids in the BME-agarose mixture. Plates were sealed with Parafilm, placed in an air-tight bag containing 5% CO_2 gas, and moved to 4°C. Organoids were stored in cold conditions for different time periods, after which the plates were returned to the 37°C incubator. The color of the growth medium was assessed throughout the procedure to make sure the pH was within a normal range and that a lack of CO_2 was not affecting the organoid viability. In the survival experiments with AFGP and α-lactalbumin we added 10 mg/ml of protein to the medium one hour before the organoids were transferred to 4°C.

The experimental design is outlined in Figure S6.1. For each condition, individual plates with organoids were prepared and each plate was left at 4°C for different periods of time ranging from 24 to 120 hours. During the cold storage period, individual organoids were followed and visually assessed every 24 hours to determine their viability. At each time point, each organoid was classified as alive or dead. Dead organoids were recog-nizable by their overall lack of structure and the presence of dark debris were the organoid was located previously as shown in Figure S6.2). Data were collected from the number of independent experiments presented in Figure S6.1. After the cold storage period, organoids were returned to

the 37°incubator and, after two to three days, their viability was visually assessed once more. After rewarming, living organoids grow considerably while dead debris remains the same, making the visual distinction between live and dead organoids straightforward.

6.5.4   Fluorescein diacetate test

Viability tests using fluorescein diacetate (FDA) were performed to test the accuracy of the visual viability assessment. FDA serves as a viability probe that measures enzymatic activity, which is obligatory to activate its fluorescence, and cell membrane integrity, which is necessary for intracellular retention of the fluorescent product [109]. FDA was chosen due to its low toxicity [110], which would allow for in situ viability assessment throughout the timespan of the experiments. The use of live/dead stains is not straightforward for organoids as the lumen of healthy organoids usually contains dead cell material because old cells are shed into the lumen, mimicking the cell shedding that occurs at the tips of the villi in the intestine [111]. As a result, stains that target dead cells are not appropriate as they would show false positives.

FDA was added to the medium at a concentration of 10 μg/ml. The medium was removed after five minutes and replaced with PBS. After 15 minutes, the wells were washed twice with PBS and the organoids were imaged using a wide-field fluorescence microscope (Axio Vert.A1, Zeiss).

FDA tests were not used to completely quantify organoid viability due to an observed inability of FDA to penetrate the BME-agarose droplets completely. The dye showed false negatives when inspecting organoids that were deeply embedded in the gel, either because the FDA was unable to fully penetrate the gel, or because it was taken up by the organoids in the periphery of the gel more rapidly than it could reach the more deeply embedded ones. As a result, fluorescence was only observed in live organoids close to the edges of the droplets, while live organoids located in central regions did not show any fluorescence that could be distinguished from the background. The visual assessment of organoids in the periphery of the gel coincided with FDA staining which supports the validity of the visual protocol.

6.5.5 Imaging FITC-AFGP and fluorescein dye

Organoids were mechanically dissociated, embedded in BME and plated in 8-well imaging chambers. Two to three days after passaging, 0.5 mg/ml of FITC-AFGP or $12.5\mu g$/ml of fluorescein salt were added to the medium and, after one hour, the plates were imaged using a fluorescence scanning confocal microscope (Eclipse Ti; Nikon) with a 40x oil immersion objective (NA = 1.30). Next, the wells were washed twice with PBS and imaged again.

6.5.6 Statistical analysis

We performed statistical analysis of the data using the two-sided Fisher's exact test. $p < 0.05$ was considered statistically significant. In all plots, the error bars represent 95% Clopper-Pearson confidence intervals. In cases for which we performed multiple independent experiments, the data were pooled and plotted together.

6.6   Appendix

6.6.1 Author contributions to the chapter

GHP and KM designed the experimental strategy. **GHP** performed the experiments and analyzed the data. ALdV provided novel reagents and labeled the AFGPs. **GHP** and KM wrote the text. HJB, JSvZ and KM supervised the study.

6.6.2 Additional figures
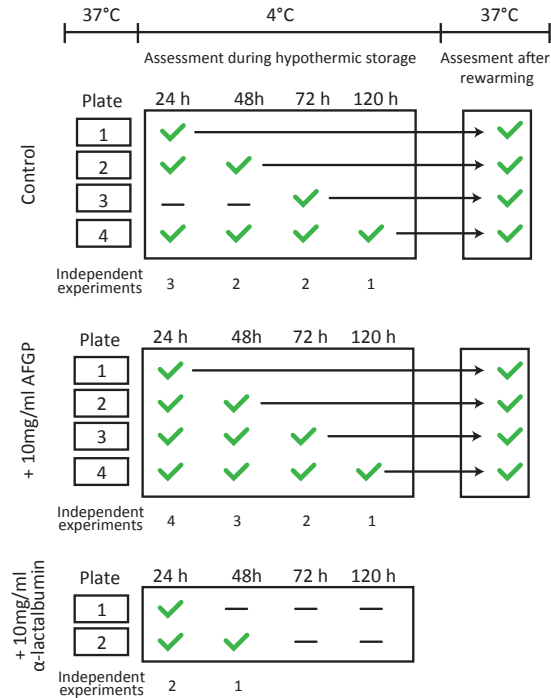
Figure S6.1 Design of hypothermic storage experiments

For each of the three conditions tested, different numbers of plates with organoids were prepared. Each plate was placed at 4°C for different periods of time during which organoid viability was assessed every 24 hours (except for control plate 3). After hypothermic storage, plates were returned to the incubator at 37°C and organoid viability was assessed again. Since assessment during hypothermic storage was performed on different plates every 24 hours, for most time points data was collected from a number of independent experiments.
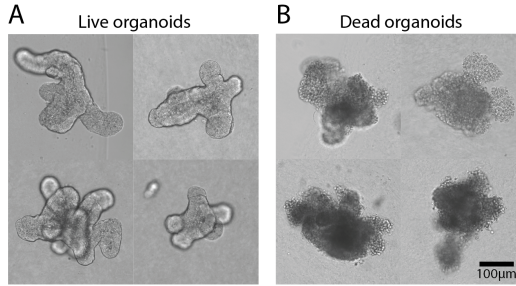
Figure S6.2 Bright-field images of live and dead organoids

Dead organoids (**B**) are visually distinguishable from live organoids (**A**) by their overall lack of structure and the presence of dark debris were an organoid was once located.
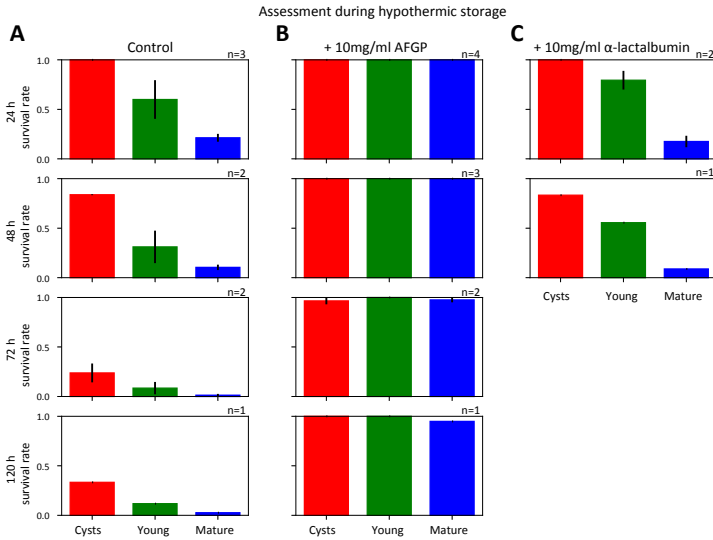
Figure S6.3 Average survival rates from independent organoid experiments

Average survival rates obtained when assessing organoid viability during hypothermic storage on different plates. Error bars represent the standard deviation. The number of independent experiments (in accordance with Figure S6.1) is shown.

7

Single-cell dynamics of growth and homeostasis in intestinal organoids

Many cells in organs are constantly renewed to replace damaged cells. New cells are generated by adult stem cells that give rise to all cell types that constitute the organ. To ensure homeostasis, stem cell proliferation and differentiation must be tightly regulated, as any imbalance would lead to disease; however, how such a tight balance is achieved in organs is still an open question. Here, we addressed this question by using intestinal organoids and computational modeling. By performing time-lapse microscopy, we were able to track individual cells in space and time in growing organoids, allowing an unprecedented view of lineage dynamics in the intestinal epithelium. We found that organoid growth is highly regulated and that cell divisions in crypts are highly symmetrical, i.e. with similar sister cell outcomes. A two-compartment computational model of dividing cells revealed that high fractions of symmetric divisions result in low variability in the number of dividing cells, suggesting that such division mode might be a mechanism in place in order to minimize fluctuations and ensure homeostasis. Our results suggest a concrete mechanism through which the intestinal epithelium and other tissues could achieve a precise balance between proliferation and differentiation.

7.1 Introduction

Adult organs are constantly losing and replacing cells through a process termed tissue renewal. Old and damaged cells are shed while younger cells take their place in order to ensure the optimal functionality of the organ. Tissue renewal is fueled by adult stem cells that have the capacity to self-renew to produce more stem cells and to differentiate to produce the various cell types that constitute the tissue. To maintain homeostasis, stem cell proliferation and differentiation must be tightly regulated as any imbalance could lead to either aberrant growth or tissue degeneration. How such a precise balance is achieved and maintained throughout the lifetime of an organism is still an unresolved question despite decades of active research into the topic.

A major challenge that has hindered the field lies in the elusive nature of adult stem cells. Based on early studies of the hematopoietic system, stem cell identity has been classically thought to be an intrinsic, hard-wired property. Such studies have also led to the conception that stem cells divide in an asymmetric fashion, with every division resulting in exactly one stem cell and one differentiated cell. However, recent findings regarding the renewal of various tissues have suggested that this view is not universal. Stem cell identity is now thought of as a plastic cellular state that can readily change as a result of internal or environmental conditions, and evidence for both symmetric and asymmetric divisions has been found [112].

Owing to its fast turnover and its simple architecture, the mammalian intestine constitutes one of the most studied organs in the context of tissue renewal. In the intestinal villi, a continuous supply of absorptive and secretory cells is provided by stem cells that sit at the base of intestinal crypts. Here, intestinal stem cells are shielded from the harsh environment found in the lumen and they are subjected to multiple environmental signals that promote their proliferative and undifferentiated status. Such signals include EGF, Wnt and Notch ligands, and are provided by both the mesenchymal tissue and adjacent epithelial Paneth cells, which together act as the intestinal stem cell niche [113]. The recent development of purely epithelial intestinal organoids, i.e. 3D cultures of intestinal tissue *in vitro*, has suggested that local signals provided by Paneth cells at crypt bottoms are sufficient for a proper crypt-villus architecture to arise, while mesenchymal-derived signals, represented by added growth factors in the culture medium, can be uniformly distributed throughout the crypt-villus axis [114, 115].

Early lineage tracing studies revealed that intestinal crypts become clonal within a few months [116]. These findings were initially interpreted under the classical stem cell definition, and thus crypt clonality was regarded as the result of a single infrequently dividing stem cell inhabiting and replenishing each crypt through asymmetric divisions that gave rise to one stem cell and one extensively dividing transit amplifying (TA) cell. It was later proposed that crypt clonality could be the result of an equipotent stem cell pool [117], where homeostasis would be achieved by balancing proliferation and differentiation at the population level. In this way, stem cells could be randomly lost through differentiation but would be replaced by proliferation of others. This idea was confirmed in later studies [118, 119], where new lineage tracing tools brought by the advent of transgenic technology revealed that intestinal stem cell divisions result in two daughter cells that have the same potential for maintaining stem cell fate. Stem cells compete for niche space at the crypt base and their fate is ultimately determined by their position, with cells near the crypt base having an advantage for retaining stemness over those closer to the niche border [120]. Cells that stochastically exit the niche enter the TA compartment and differentiate after undergoing a few rounds of division and exiting the cell cycle [113].

Niche-based stem cell systems are generally thought to be robust as they regulate the balance between proliferation and differentiation at the population level through access to a limited niche space [121]. However, how such robustness in the intestine is achieved in practice is not completely understood since the short-term dynamics of individual cells within and outside the stem cell niche have not been resolved. In addition, tissues do not only require proper cell numbers to be maintained on average, but short-term deviations from this average must also be kept to a minimum. It is currently unknown how individual cells and their progeny adapt their behavior in order to minimize fluctuations and to ensure homeostasis at different timescales.

Answers to these questions have long remained out of reach due to the technical challenges associated with visualizing cells that are deeply embedded within the body. Recent advances have allowed the use of intravital microscopy to directly observe single cells at crypt bottoms *in vivo* [120, 122], but the spatial and time resolutions that can be achieved with this technique greatly limit the ability to trace all individual cells and their progeny for long periods of time. Here, by performing time-lapse microscopy and single-cell tracking of murine organoid crypts, we have resolved for the first

time the dynamics of cell division, cell lineages and cell movement as a function of position in the crypt. We found that the number and positioning of dividing cells is highly controlled despite significant organoid growth and heterogeneity. In addition, we found a striking correlation between sister cell behaviors, suggesting that cell divisions in the intestine are mostly symmetrical, i.e. with similar sister cell outcomes. A potential explanation for such behavior was obtained through a two-compartment computational model, which revealed that variability in the numbers of dividing and differentiating cells is minimized when the fraction of symmetric divisions is maximized. This is in sharp contrast to a one-compartment model, where a highly fragile balance between proliferation and differentiation is only achieved by executing mostly asymmetric divisions. Our findings suggest a concrete mechanism through which the intestinal epithelium and other stem-cell niche systems could ensure homeostasis and minimize fluctuations.

7.2   Results

7.2.1   Time-lapse imaging allows tracking of organoid growth with single-cell resolution

Intestinal organoids grow considerably over the course of a few days (Figure 7.1A). To examine the dynamics of individual cells within crypts during such extensive growth, we used organoids with the nuclear fluorescent reporter H2B-mCherry (Figure 7.1B) and performed confocal 3D time-lapse microscopy for up to 65 hours with 12 minute time resolution. We observed multiple cell division events, which could be clearly distinguished by the apical displacement of the nucleus followed by chromosome condensation and separation, and finally, basal migration of the nuclei of the newly born cells (Figure 7.1C).

After existing automated solutions for cell tracking failed to produce reliable results, we used custom-written software to manually track every cell within organoid crypts by recording their nuclei positions in 3D space and time (Figure 7.1D), and assigning each cell a unique label. Cell labels were noted after every cell division, allowing us to reconstruct lineage trees of up to six generations (Figures 7.1G, S7.1).

To explore how cell dynamics vary as a function of position through the
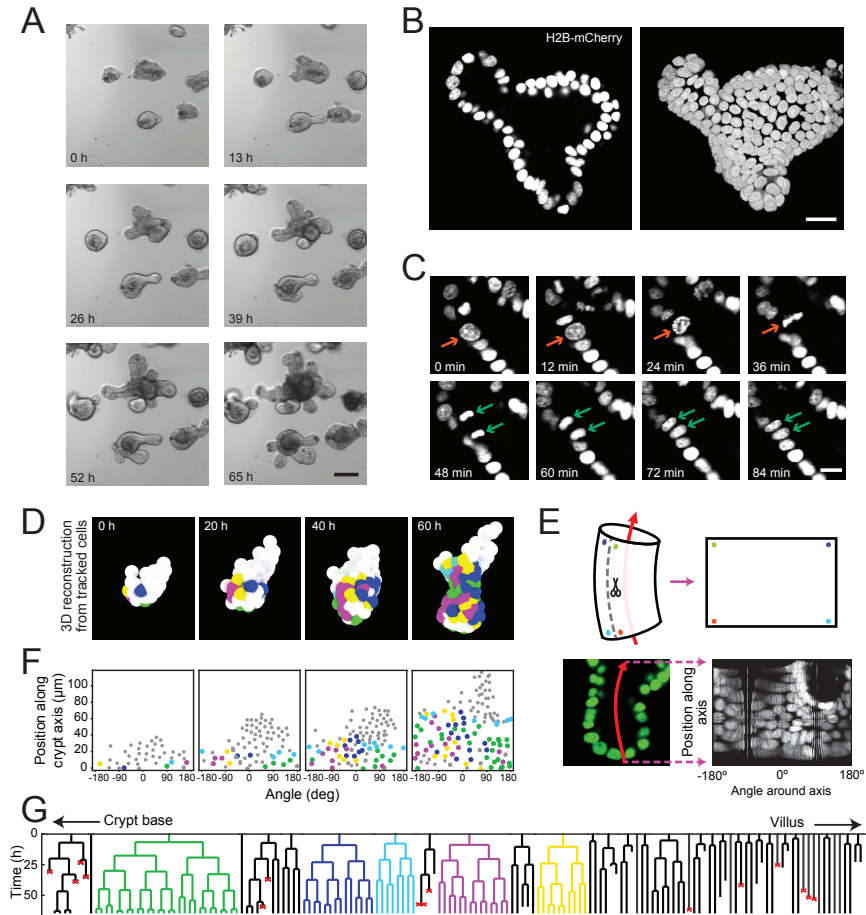
Figure 7.1 Time-lapse imaging and single-cell tracking of intestinal organoid crypts

A Bright-field time-lapse images of intestinal organoids showing considerable growth over the course of 65 hours. Scale bar is 100 μm.

B Images of an organoid expressing an H2B-mCherry reporter where individual nuclei are visible. Left image shows a confocal z-slice and right image represents a 3D reconstruction. Scale bar is 25 μm.

C Snapshots of a cell division event in a crypt. Cell divisions are distinguished by the apical migration of the nucleus followed by chromosome condensation (red arrows). After mitosis, the nuclei of the two newly born cells are displaced basally (green arrows). Scale bar is 10 μm.

Figure 7.1

D 3D reconstruction of a crypt growing in time using the positions of tracked nuclei. Colors represent cells that belong to the same lineage.

E Illustration showing the process of crypt unwrapping. After the crypt-villus axis is annotated (red arrow), tracked cell positions are projected onto the surface of a bent cylinder. The cylinder is then unfolded and its surface is mapped onto a two-dimensional plane defined by the distance along the axis and the angle around the axis.

F Unwrapped representation of the crypt in **D**, where colors represent the same lineages.

G Lineage trees of cells within the crypt in **D** and colored accordingly. Cells in the initial time point are ordered according to their distance to the crypt base. Red crosses indicate cell deaths and incomplete lines indicate cells that could not be accurately traced further due to insufficient fluorescence intensity or movement outside of the field of view.

crypt-villus axis, we manually annotated the axes of crypts at every time point. With this information, we proceeded to "unwrap" the crypts, i.e. we projected every tracked cell position onto the surface of a cylinder which we then unfolded, as exemplified by the illustration in Figure 7.1E. This allowed us to visualize dynamics through the entire surface of the crypt in a two-dimensional plane defined by two coordinates: the position along the axis and the angle around the axis (Figures 7.1E, 7.1F). By ordering cells in the initial time point according to their position along the axis, we could observe a spatial gradient in lineage dynamics (Figure 7.1G); cells closer to the crypt base produced frequently dividing progeny, while those farther away resulted in lineages with less dividing cells.

7.2.2 Cell divisions in organoid crypts are highly regulated

Even though organoids recapitulate several aspects of the intestine *in vivo* [123], it is unknown to what extent their growth is regulated and, if so, whether such regulation faithfully represents the *in vivo* situation. The intestine consists of a repetitive and regular crypt-villus architecture, with little variation in the size and organization of crypts [124]. Additionally, intestinal cells are subjected to stereotypical signaling gradients along the crypt-villus axis since stem cells are uniformly intermingled with Paneth cells strictly at crypt bottoms [115] and different signaling molecules are produced by mesenchymal cells at distinct positions along the axis [113]. In contrast, organoids are usually grown in poorly defined and highly variable artificial extracellular matrices [125]. They also vary widely in size, shape and number of crypts (Figures 7.1A, S7.2), likely due to the absence of

mesenchymal tissue, resulting in unconstrained growth and in the lack of defined signaling gradients.
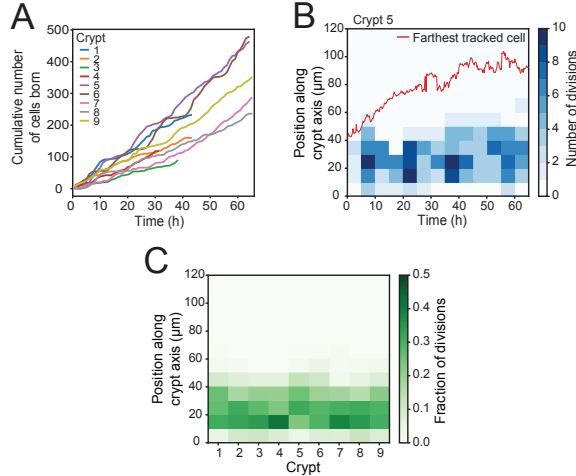
Figure 7.2 Regulation of cell divisions in intestinal organoids

A Cumulative number of cells born as a function of time for nine tracked crypts.

B Number of divisions that occurred at different positions along the crypt axis as a function of time in a single tracked crypt. Red line corresponds to the position of the farthest tracked cell from the crypt bottom at every time point. Apical displacement of the nuclei during mitosis results in few divisions occurring at less than 10 μm from the crypt base.

C Fraction of divisions that occurred at different positions along the crypt axis for nine tracked crypts. All divisions observed throughout the time-lapse sessions are included.

Furthermore, intestinal organoids grow continuously, requiring mechanical dissociation every few days to be maintained, as opposed to the intestine where size is kept constant by a precise balance between cell birth and death rates. This has led to the proposal that organoids represent a state of intestinal repair rather than actual homeostasis [126]. To differentiate between these scenarios, we quantified the cumulative number of cell births as a function of time for different crypts. In a homeostatic system, we would expect this quantity to increase linearly. This would indicate that cell division rates are kept constant in time, meaning that on average, every cell division results in the birth of one dividing and one non-dividing cell. In contrast, this quantity would increase exponentially in a regenerat-

ing system, given that dividing cells should outnumber non-dividing cells in order to replenish the tissue. Our results showed that the cumulative number of cells that are born grows linearly as a function of time (Figure 7.2A). Such observations are not consistent with a regeneration state, but they rather point to a highly regulated homeostatic system.

We then quantified the number of cell divisions as a function of the position along the crypt axis. Remarkably, even though organoids grew significantly during imaging sessions (Figure 7.1A), we found that cell divisions always occurred at less than 70 μm from the crypt base (Figure 7.2B), indicating that the size of the proliferative compartment is kept constant in time. Moreover, the proliferative zone was found to have a similar length in all the analyzed crypts (Figure 7.2C), with most divisions occurring at distances of less than 50 μm from the crypt bottom, even though crypts varied in size and cell number (Figure 7.2A). These results further support the notion that, at least at the time scale of our experiments, organoid crypt growth is highly controlled and could therefore provide valuable insights into crypt regulation *in vivo*.

7.2.3   Sister cells have similar outcomes

A visual inspection of the lineage trees we obtained for cells from various crypts (Figure S7.1) revealed a surprising common feature: sister cells often followed similar division patterns. More strikingly, when a cell within a lineage deviated from the behavior of its relatives, its sister usually followed. For instance, when most cells within a lineage followed a certain division pattern, i.e. either they divided or remained undivided, exceptions were usually found in sister pairs (Figure 7.3A, top panels). In addition, when most dividing cells within a lineage showed similar cell cycle durations, variations were again commonly found in sister cells (Figure 7.3A, bottom panels).

To further examine the similarities between sister cells, we calculated the clone size distribution for all tracked cell lineages (Figure 7.3B). This analysis revealed an enrichment of even-sized clones, supporting our observations that dividing and non-dividing phenotypes are usually displayed symmetrically between sister pairs. Moreover, we observed a strong correlation between the duration of sister cell cycles (Figure 7.3C), even though cell cycles among all tracked cells showed a broad distribution (Figure S7.3).

The strong correlations found between sisters raised the question of
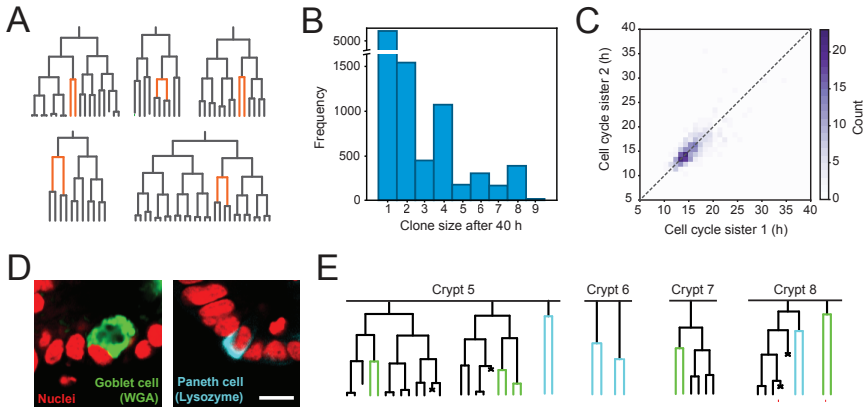
Figure 7.3 Correlation between sister cell behaviors

A Examples of lineage trees where pairs of sister cells (orange) follow a different division pattern than their relatives (gray).

B Clone size distribution obtained by sliding a window of 40 hours through all lineage trees in Figure S7.1 in steps of one hour. Note that the vertical axis is broken to account for the much higher frequency of clones of size one, corresponding to non-dividing cells.

C Duration of sister cell cycles plotted against each other for pairs in which both sisters divided. Sister labels ('1' or '2') were assigned randomly.

D Fluorescence images of fixed organoids following time-lapse experiments. Upper panel shows a Goblet cell (green) stained with wheat germ agglutinin (WGA) and lower panel shows a Paneth cell (cyan) stained with anti-lysozyme antibody. Scale bar is 10 μm.

E Lineage trees in which a cell division event was found to precede the appearance of Goblet (green) or Paneth (cyan) cells. Only cases in which both daughters could be tracked until the final time point are included.

whether similarities were only restricted to division patterns or if they might also be found in cell fate patterns. To test this hypothesis, we used fluorescently labelled cell fate markers for secretory lineages to stain organoids after the time-lapse experiments. These markers allowed us to distinguish which cells had become Paneth and Goblet cells by the end of the imaging sessions (Figure 7.3D). Remarkably, for all cases in which a cell division event preceded the appearance of a Goblet or Paneth cell and in which we were able to track both progeny until the final time point, we observed that both sisters adopted the same fate (Figure 7.3E).

Taken together, our results suggest that divisions of all cells in crypts are highly symmetric in the sense that both sisters display either a dividing

or a non-dividing behavior, and that both might also adopt the same fate.

7.2.4 One- and two-compartment models employ different strategies to ensure homeostasis

The high fraction of symmetric divisions we observed raised the question of whether such behavior could play a functional role in maintaining crypt homeostasis. To address this, we turned to a computational model of compartments, in which a set of intrinsically identical cells follow division patterns that are probabilistically dictated by the compartment in which they are in. For simplicity, our model omits aspects related to cell fate and crypt geometry, as the main goal was to understand how different division patterns in a system of otherwise identical cells affect homeostasis. With homeostasis, we specifically mean that the number of dividing cells in the system remains approximately constant through time.

In our model, each compartment is defined by its growth rate α, i.e. the change in the number of dividing cells per division, and its degree of symmetry ϕ, i.e. the relative proportion between symmetric and asymmetric divisions. We assume that cells in the model can divide symmetrically to produce two dividing cells with probability p or two non-dividing cells with probability q, as well as divide asymmetrically with probability $r = 1 - (p + q)$ (Figure 7.4A). Therefore, the growth rate can be expressed as $\alpha = p - q$ and the degree of symmetry as $\phi = p + q$. The growth rate can range between $\alpha = -1$, when all divisions lead to two non-dividing cells ($q = 1$), and $\alpha = 1$, when all divisions lead to two dividing cells ($p = 1$), respectively (Figure 7.4B, left). On the other hand, the degree of symmetry ranges from $\phi = 0$, when all divisions are asymmetric ($r = 1$), to $\phi = 1$, when all divisions are symmetric ($r = 0$) (Figure 7.4B, right). Furthermore, cell cycle times in the simulations were randomly drawn from a skew normal distribution that was fitted to our experimental data (Figure S7.3).

We started by considering a one-compartment case, i.e. when the probabilities of undergoing each of the three division types are the same for all simulated cells. For homeostasis to occur, the growth rate of the compartment must be exactly $\alpha = 0$, since $\alpha < 0$ would lead to a loss of dividing cells and $\alpha > 0$ would result in exponential growth. We performed simulations with varying values of the degree of symmetry ϕ while maintaining $\alpha = 0$, and we measured the variability in the number of dividing cells D through time by quantifying the coefficient of variation, i.e. the standard

deviation divided by the mean. Our simulations expectedly showed that fully asymmetric divisions result in the best performance (Figure 7.4C, top panel, $\phi = 0$). Here, since every division is asymmetric, the total number of dividing cells is kept perfectly constant in time resulting in a coefficient of variation of zero, and thus the system achieves perfect homeostasis as per our definition. However, simulations unexpectedly showed that adding only a small fraction of symmetric divisions results in high variability in the number of dividing cells, and such variability remains similarly high as symmetric divisions become more prominent (Figure 7.4C, top panel, $\phi > 0$). Moreover, the large fluctuations introduced by adding symmetric divisions make the system prone to depletion and to overgrowth of dividing cells, with this effect being more pronounced at higher values of the degree of symmetry ϕ (Figure 7.4C, bottom panel). Overall, the simulations suggest that a one-compartment model represents a highly fragile system that can only achieve homeostasis by executing purely asymmetric divisions.

We next turned our attention to a two-compartment model (Figure 7.4D). Here, each individual compartment has a non-zero growth rate, but homeostasis can still occur as long as the overall growth of the system is zero. For such a balance to occur, one compartment (termed the 'proliferative' compartment) must have a positive growth rate α_p, while the other (termed the 'differentiation' compartment) must have a negative growth rate α_d. We assume that the proliferative compartment has a fixed size S and the differentiation compartment has no size constraints. In this way, when a cell division occurs in the proliferative compartment and it is already full, a random cell is expelled to the differentiation compartment, where it can either remain undivided or divide according to the parameters of its new environment.

A deterministic, analytical representation of the two-compartment model (J.S. van Zon, manuscript in preparation) revealed the existence of a steady state solution where the total number of dividing cells D remains constant, which in turn results in a constant production rate of non-dividing cells. This occurs when the number of dividing cells in the proliferative compartment D_p has a value of

$$D_p^* = \alpha_p S, \tag{7.1}$$

and when the number of dividing cells in the differentiation compartment D_d is

$$D_d^* = S \ln\left(1 + \alpha_p\right) \frac{\alpha_d - \alpha_p}{\alpha_d} - \alpha_p S. \tag{7.2}$$

Then, the steady state number of dividing cells in the system can be ex-

A

Symmetric   Asymmetric

Probability: p q $r = 1 - (p + q)$

B

Growth rate
$$\alpha = p - q$$

Degree of symmetry
$$\phi = p + q$$

$\alpha \to 1$ $\phi \to 0$

$\alpha \to -1$ $\phi \to 1$

C

Coefficient of variation of D

Rate (events/1,000 h)

- Depletion
- Overgrowth

ϕ

D

Size S

Unconstrained size

Proliferative compartment
$$\phi_p$$
$$\alpha_p > 0$$

Differentiation compartment
$$\phi_d$$
$$\alpha_d < 0$$

E

Coefficient of variation of D

$\phi = 1$

α_p

α_d

$\alpha_p = -\alpha_d$

ϕ

$\alpha_p, -\alpha_d$

F

D (# of dividing cells)

Time (h)

Time

10μm
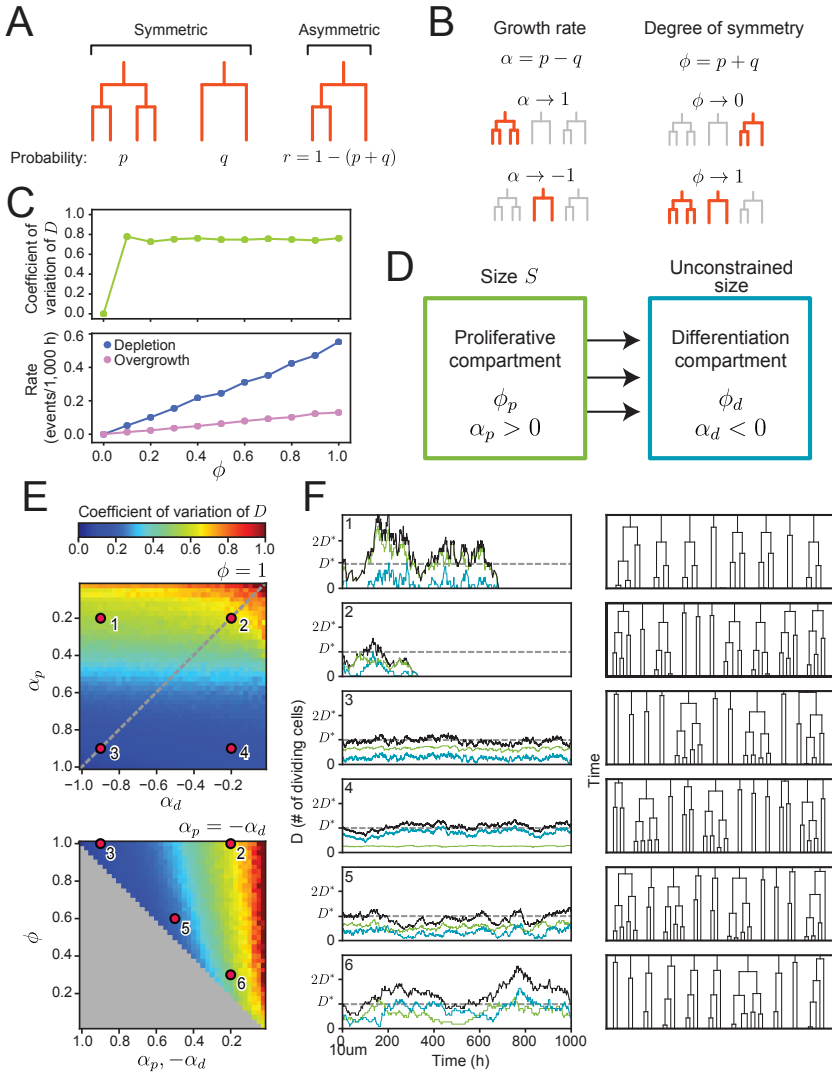
Figure 7.4 Compartmental computational model

A Types of cell divisions and their corresponding probabilities, where the type of division is defined according to the division pattern of the sister cells.

B Definition of the parameters α and ϕ used in the model. The growth rate α refers to the increase in the number of dividing cells per division while the degree of symmetry refers to the relative fraction between symmetric and asymmetric divisions.

Figure 7.4

C Results from the simulations of the one-compartment model. Top panel shows the coefficient of variation (standard deviation divided by mean) of the number of dividing cells D as a function of ϕ. Bottom panel shows the rate at which depletion (blue) or overgrowth (pink) events occurred. When the number of dividing cells in a simulation reached a value of zero (depletion event) or grew by a factor of 5 (overgrowth event), the simulation was ended and a new simulation was started until a total simulation time of 10^6 hours was reached. Thus, the rate of depletion or overgrowth refers to the number of times simulations had to be restarted for each value of ϕ divided by the total simulation time.

D Illustration of the two-compartment model.

E Coefficient of variation of the total number of dividing cells D obtained from the two-compartment model. Top panel shows the effects of varying the growth rates of both compartments when all divisions are symmetric ($\phi = 1$), and bottom panel shows the effects of varying the degree of symmetry when both compartments have opposite growth rates ($\alpha_p = -\alpha_d$, dashed line in top panel). The grey region in bottom panel corresponds to inaccessible parameter space.

F Left panels show the number of dividing cells as a function of time for the different points in parameter space shown in **E**. Green lines represent the number of dividing cells in the proliferative compartment, blue lines in the differentiation compartment and black lines represent the sum of both. The dashed line shows the steady state value of D given by Equation 7.3, around which the total number of dividing cells (black) fluctuates. Right panels represent corresponding examples of lineage trees obtained from the simulations for a time scale comparable to our time-lapse experiments (50 hours).

pressed as

$$D^* = D_p^* + D_s^* = \ S \ln \left(1 + \alpha_p \right) \frac{\alpha_d - \alpha_p}{\alpha_d}. \qquad (7.3)$$

Hence, the steady state value of D is independent of the degree of symmetry ϕ, and a solution for $D^*, D_p^*, D_d^* > 0$ exists when $\alpha_p > 0$ and $\alpha_d < 0$.

In contrast to the analytical model, our computational model has a discrete and probabilistic nature; thus, the number of dividing cells fluctuates stochastically around the steady state value given by Equation 7.3, with the extent of the fluctuations depending on the parameter values of both compartments. To determine the parameter combinations that result in the smallest fluctuations, i.e. those which are better for maintaining homeostasis, we performed simulations and, as before, measured the coefficient of variation of the number of dividing cells D. For simplicity, we assume the degree of symmetry is the same for both compartments ($\phi = \phi_p = \phi_d$), as its value has no effect on the steady state solution for D. To avoid any statistical effects that could arise from pre-steady state dynamics, we initialized all simulations with the steady state number of dividing cells in both compartments for a fixed size of the proliferative compartment S (as

defined in Equations 7.1 and 7.2).

Simulations showed that the best performing systems are those in which symmetric divisions are maximized ($\phi \rightarrow 1$), and where growth is highest in the proliferative compartment ($\alpha_p \rightarrow 1$) and lowest in the differentiation compartment ($\alpha_d \rightarrow -1$) (Figures 7.4E, 7.4F, point 3). In general, as long as α_p and ϕ are high, variation remains low and is marginally affected by changes in α_d (Figures 7.4E, 7.4F, point 4). However, high α_d values come at the expense of maintaining an excessive number of dividing cells (Figure S7.4A), as a high fraction of divisions yield two dividing cells in the differentiation compartment. In contrast, fluctuations in the system are highest when divisions are symmetric ($\phi \rightarrow 1$) but growth rates in both compartments are close to zero ($\alpha_p \rightarrow 0$, $\alpha_d \rightarrow 0$) (Figures 7.4E, 7.4F, point 2). For low α_p, variability can be slightly reduced by decreasing α_d (Figures 7.4E, 7.4F, point 1), or by decreasing ϕ (Figures 7.4E, 7.4F, point 6). However, a low growth rate in the proliferative compartment is undesirable as it frequently results in the depletion of dividing cells (Figure S7.4B). Finally, intermediate variability is observed at intermediate values of all parameters (Figures 7.4E, 7.4F, point 5).

Overall, our simulations indicate that the best approach to minimize variability in a two-compartment system consists of maximizing the growth rate in the proliferative compartment, which is achieved by maximizing the fraction of symmetric divisions that give rise to two dividing cells, and to a lower extent, by minimizing the growth rate in the differentiation compartment. This result suggests that the high fraction of symmetric divisions observed in organoid crypts could be a mechanism in place to minimize fluctuations in the number of dividing cells and ensure homeostasis.

7.2.5 Paneth cells define the proliferative compartment

To test how our two-compartment computational model results compare to our experimental data, we set out to find the equivalent of the proliferative and the differentiation compartments in organoids. Paneth cells secrete important signals that are required for maintaining stemness [115], creating short-range gradients around them [127]. Therefore, distance to Paneth cells could serve as a measure to distinguish between the proliferative and differentiation compartments.

Paneth cell-derived Notch and Wnt ligands are bound to cell membranes and are not spread by diffusion [127]. Hence, due to the curved geometry
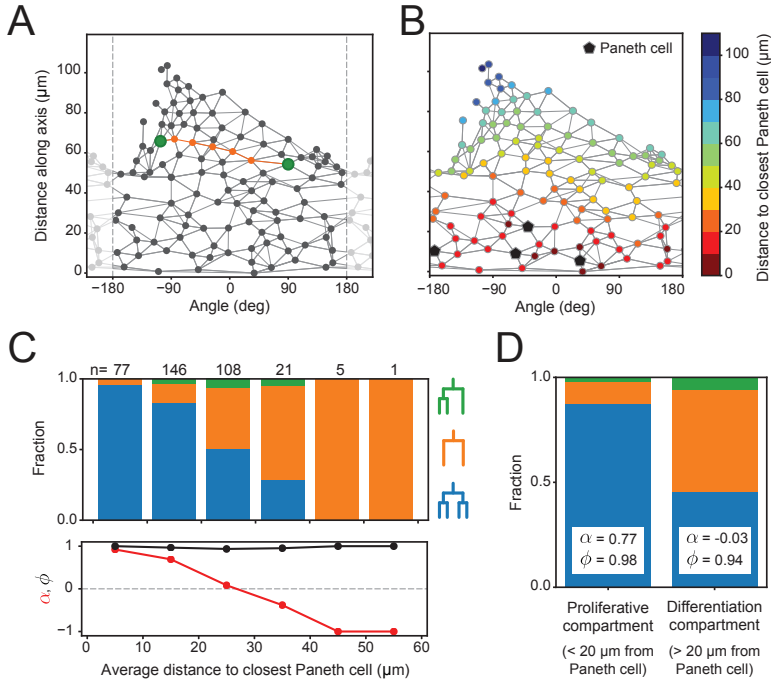
Figure 7.5 Distance to Paneth cells to define the proliferative and differentiation compartments

A Unwrapped graph representation of the crypt shown in Figure 7.1D. Cells are vertices that are connected to nearby neighbors by weighted edges, where the weight corresponds to the 3D Euclidean distance between the two connected cells. The distance between two cells (green) along the crypt surface can be approximated by finding the shortest path (orange) along the graph and summing the weight of each edge within such path.

B Graph representation of a crypt where the color of each vertex represents the distance along the graph to the closest Paneth cell. Black markers correspond to Paneth cells.

C Top panel shows the fraction of cells that divide to produce two dividing daughters (blue), two non-dividing daughters (orange), and both a dividing and a non-dividing daughter (green), as a function of distance to the closest Paneth cell. Bottom panel shows the growth rate α and degree of symmetry ϕ as a function of the distance to the closest Paneth cell. The distance to the closest Paneth cell is defined as the average distance throughout the lifetime of the cell.

D Fraction of cell division types (as defined in **C**) and corresponding values of α and ϕ for the proliferative and differentiation compartments. The proliferative compartment was defined as the area delimited by a 20 μm radius around each Paneth cell, and the differentiation compartment as the space beyond this limit.

of the crypt, directly calculating the Euclidean 3D distance between two cells would lead to inaccurate results, as the line connecting two cells would cross the crypt lumen in many cases. A more accurate measure would be obtained by connecting cells with a line along the curved epithelial surface. To approximate the crypt surface, we constructed a graph in which cells represent vertices that are connected to nearby cells by weighted edges, where the weight represents the 3D Euclidean distance between them (Figure 7.5A). With the graph representation of the crypt, we could measure distances between cells by finding the shortest paths between vertices along the graph. In this way, for each cell and at each time point, we calculated the distance to the closest Paneth cell (Figure 7.5B) and computed the average distance throughout the lifetime of the cell.

We next classified every dividing cell according to its division type as defined in Figure 7.4A, and quantified the fraction of cells belonging to each category as a function of distance to the closest Paneth cell (Figure 7.5C, top panel). This revealed that close to Paneth cells most divisions resulted in two dividing daughters (Figure 7.5C, top panel, blue bars), while farther away, they resulted in two non-dividing cells (Figure 7.5C, top panel, orange bars). We then calculated the values of the growth rate α and the degree of symmetry ϕ as a function of distance to the closest Paneth cell (Figure 7.5C, bottom panel). The value of ϕ remained high at all distances, denoting the low fraction of asymmetric divisions observed (Figure 7.5C, top panel, green bars). In contrast, the value of α was high only at short distances (< 20 µm), and decayed afterwards. Thus, we defined the proliferative compartment as the area delimited by a 20 µm radius around each Paneth cell, and the differentiation compartment as the space beyond this limit. We quantified the division types as well as the growth rate α and degree of symmetry ϕ of each compartment (Figure 7.5D). This revealed a high positive value of α in the proliferative compartment, and a slightly negative α in the differentiation compartment.

The parameter values obtained from our experimental data fall within a region of parameter space with low variability in the number of dividing cells according to the two-compartment model. However, the experimental values do not correspond to the best performing parameters of the model, especially since the growth rate α in the differentiation compartment is only slightly negative. As explained previously, low negative α values in the differentiation compartment result in elevated numbers of dividing cells (Figure S7.4A). This could well be a requirement in the intestine, where transit amplifying cells undergo multiple rounds of division in order to

produce the high amounts of differentiated cells that are necessary for its constant renewal. Nevertheless, our current definition of the proliferative and differentiation compartments in our experimental data is still preliminary; further analysis could yield a more appropriate definition and hence more accurate parameter values. Currently, we only take into account the average distance of a cell to the closest Paneth cell; however, other factors that are now omitted could have a significant impact on the division pattern of cells. For instance, a cell that is neighboring two Paneth cells is expected to receive higher amounts of Wnt and Notch ligands than a cell that is close to only one Paneth cell. In addition, Wnt and Notch signals might have distinct effects on cells at different moments during their cell cycle [128]. An updated definition of the experimental compartments that takes these factors into account could hopefully show that the system is closer to the optimal parameters obtained from our model.

7.3   Conclusions and outlook

In this chapter, we have shown that by performing long-term time-lapse microscopy of intestinal organoids we can follow all individual cells inside growing crypts, allowing an unprecedented view of lineage dynamics in the intestinal epithelium. Our tracking data suggests that organoid growth is highly regulated, as the number of dividing cells is kept constant in time. Moreover, the proliferative region in crypts does not expand in time and is of similar size between different crypts, regardless of their size or cell number. These observations unexpectedly showcase intestinal organoids as highly regulated systems, at least at the time scale of our experiments, despite the lack of an underlying mesenchymal tissue and their wide variability in shape and size.

It is generally thought that intestinal stem cells divide symmetrically as both progeny are born with equal potential to preserve stemness [118, 119]. However, symmetry in potential does not imply symmetry in outcome. Asymmetric divisions could still arise if initially identical sisters adopt different fates as a result of them becoming separated and reaching different compartments after birth, as has been suggested previously [129]. Surprisingly, we found a high correlation between sister cell division and differentiation patterns, suggesting that the outcome of cell divisions in crypts is highly symmetrical, i.e. with both sister cells dividing at similar time

points or both remaining undivided, and possibly with both adopting the same fate. Further time-lapse experiments followed by fluorescent staining for different cell fate markers could reveal if cells other than Paneth and Goblet cells are also found to be born in pairs.

The fact that sister cells can both adopt a Paneth or Goblet fate is particularly surprising given that secretory fate specification has been reported to coincide with cell cycle exit *in vivo* [130], suggesting it is unlikely that Goblet and Paneth sisters result from a mother cell that had already become committed to a secretory fate. Furthermore, most sister cells in intestinal organoids remain long-term neighbors [129]; yet, secretory fate specification in the intestine is driven by lateral inhibition through Notch signaling [113], making it unlikely for neighboring cells to both adopt a secretory fate. Thus, how pairs of Goblet and Paneth sister cells arise remains an open question.

Computational modeling revealed that a one-compartment system performs poorly at maintaining a constant number of dividing cells, with both overgrowth and cell depletion occurring frequently unless cell divisions are strictly asymmetrical. In contrast, a two-compartment model is able to maintain dividing cell numbers with low variation over a wider parameter range. This system minimizes fluctuations in the number of dividing cells, and thus is closer to homeostasis, when most divisions in the proliferative compartment are symmetrical and give rise to two dividing cells. When defining a small area surrounding Paneth cells as the proliferative compartment in our experimental data, we found that most divisions in this region are symmetrical and result in two dividing cells, consistent with parameters that result in low variability in the model. Thus, our model provides an explanation for the observed high fraction of symmetric divisions, as it suggests that this division mode might be a mechanism to ensure homeostasis.

Overall, our results suggest a concrete mechanism through which a two-compartment system can minimize fluctuations in the number of dividing cells and thus, achieve homeostasis. Whether such a mechanism extends beyond the organoid setting is still to be resolved. Organoids are grown in an unnatural and poorly characterized environment, and fluctuations in growth factor concentrations could artificially alter lineage dynamics in their crypts. Performing time-lapse microscopy and single-cell tracking *in vivo* in the same way we have done in organoids is not feasible; however, clone size distributions can be obtained by performing lineage tracing experiments in mice. In this way, an ongoing collaboration with the van

Rheenen lab from The Netherlands Cancer Institute will aim to uncover whether even-sized clones are also enriched *in vivo*, as observed in Figure 7.3B. These results will provide insights as to whether the symmetry-based regulation mechanism we have found in organoids could be translated to the intestine *in vivo*.

Finally, similarly to the intestine, stem cell niches have been described for several vertebrate and invertebrate tissues [131], where competition for space within the niche and balance at the population level have also been found [132, 133]. Our results could therefore provide a more general mechanism through which different tissues minimize fluctuations and achieve homeostasis.

7.4   Materials and methods

7.4.1   Organoid culture

H2B-mCherry murine intestinal organoids were a gift from Norman Sachs and Joep Beumer (Hubrecht Institute, The Netherlands). Organoids were cultured in basement membrane extract (BME, Trevingen) and overlaid with growth medium consisting of murine recombinant epidermal growth factor (EGF 50 ng/ml, Life Technologies), murine recombinant Noggin (100 ng/ml, Peprotech), human recombinant R-spondin 1 (500 ng/ml, Peprotech), n-Acetylcysteine (1 mM, Sigma-Aldrich), N2 supplement (1x, Life Technologies) and B27 supplement (1x, Life Technologies), Glutamax (2 mM, Life Technologies), HEPES (10mM, Life Technologies), Penicilin/Streptomycin (100 U/ml 100 µg/ml, Life Technologies) in Advanced DMEM/F-12 (Life Technologies). Organoid passaging was performed by mechanically dissociating crypts using a narrowed glass pipette.

7.4.2   Time-lapse imaging

Mechanically dissociated organoids were seeded in imaging chambers one day before the start of the time-lapse experiments. Imaging was performed using a scanning confocal microscope (Nikon A1R MP) with a 40× oil immersion objective (NA = 1.30). 30 z-slices with 2 µm step size were taken per organoid every 12 minutes. Experiments were performed at 37°C

and 5% CO_2. Small but already formed crypts that were budding perpendicularly to the objective were selected for imaging.

7.4.3 Fluorescent staining

After time-lapse imaging, organoids were fixed with 4% formaldehyde (Sigma) at room temperature for 30 minutes. Next, they were permeabilized with 0.2% Triton-X-100 (Sigma) for one hour at 4°C and blocked with 5% skim milk in TBS at room temperature for one hour. Subsequently, organoids were incubated in blocking buffer containing primary antibody (rabbit anti-lysozyme 1:800, Dako #A0099) overnight at 4°C, and then incubated with secondary antibody (anti-rabbit conjugated to Alexa Fluor© 405 1:1,000, Abcam #ab175649) at room temperature for one hour. Afterwards, they were incubated with wheat germ agglutinin (WGA) conjugated to CF©488A (5 μg/ml Biotium) at room temperature for two hours, followed by incubation with RedDot™1 Far-Red Nuclear Stain (1:200, Biotium) at room temperature for 20 minutes. Finally, organoids were overlaid with mounting medium (Electron Microscopy Sciences). The procedure was performed in the same imaging chambers used for time-lapse imaging in order to maintain organoids in the same position. Imaging was performed with the same microscope as previously described. Note that WGA stains both Paneth and Goblet cells, but the lysozyme staining allowed the unequivocal distinction between them.

7.4.4 Single-cell tracking

Cells were manually tracked by following the center of mass of their nuclei in 3D space and time using custom-written image analysis software. We started by tracking cells that were at the crypt bottom in the initial time point and progressively tracked cells positioned towards the villus region until we had covered all cells within the crypt that divided during the time-lapse recording. We then tracked at least one additional row of non-dividing cells positioned towards the villus region. Cell deaths were identified either by the extrusion of whole nuclei into the organoid lumen or by the disintegration of nuclei within the epithelial sheet. Only crypts that grew approximately perpendicularly to the imaging objective and that did not undergo crypt fission were tracked.

7.4.5   Crypt unwrapping

At every time point the crypt axis was manually annotated in the xy plane at the z position corresponding to the center of the crypt, since tracked crypts grew perpendicularly to the objective. Three to six points were marked along the axis, through which a spline curve $\boldsymbol{s}(r)$ was interpolated. Then, for each tracked cell i we determined its position along the spline by finding the value of r that minimized the distance d between the cell position $\boldsymbol{x}_i$ and the spline, i.e. $d(r_i) = \min_r |\boldsymbol{s}(r) - \boldsymbol{x}_i|$. At each time point, the bottom-most cell of the crypt, i.e. that with the lowest value of r_i, was defined as position zero. Thus, the position along the axis p_i for cell i was defined as $p_i = r_i - \min_i \{r_i\}$. To determine the angle around the axis θ_i for cell i, we considered a reference vector $\boldsymbol{u}$ pointing in the direction of the imaging objective, given by $\boldsymbol{u} = (0, 0, -1)$, and the vector $\boldsymbol{v}_i = \boldsymbol{x}_i - \boldsymbol{s}(r_i)$ defined by the position of the cell $\boldsymbol{x}_i$ and the position of minimum distance along the spline $\boldsymbol{s}(r_i)$. Then, the angle is given by $\theta_i = \mathrm{acos}(\frac{\boldsymbol{u} \cdot \boldsymbol{v}_i}{uv})$.

7.4.6   Distance to Paneth cells

To create the connections in the graph representation of the crypt, for each cell we found the five closest cells within a 15 μm radius, as a visual inspection revealed an average nucleus size of 10 μm and an average of five neighbors per cell (data not shown). To calculate distances between cells, we used Dijkstra's algorithm to find the shortest path along the graph and then summed the weight of each edge within the path, given that the edge weights correspond to 3D distances between cells.

To classify cells according to their division pattern (as defined in Figure 7.4A), we first classified cells as either dividing or non-dividing. Defining dividing cells was straightforward, as their division could be directly observed. As for non-dividing cells, we applied two criteria. First, cells should have been tracked for at least 30 hours without dividing. Otherwise, if we were unable to track a cell for 30 hours, either because it went out of the field of view or because it was born soon before the end of the time-lapse experiment, we defined it as non-dividing if its last recorded position along the crypt axis was higher than 60 μm, as almost no divisions were observed beyond this distance (Figure 7.2C). All other cells were classified as undetermined and were not included in the analysis. Dying cells were also excluded from the analysis.

7.4.7   Computational model

Simulations were initialized by generating a collection of dividing cells, each belonging to either the proliferative or the differentiation compartment. For each parameter combination, the initial number of dividing cells assigned to each compartment was obtained by rounding to the closest integer the values given by Equations 7.1 and 7.2. When the initial number of dividing cells in the proliferative compartment was lower than the compartment size S, non-dividing cells were generated in order to fill the compartment, and the number of dividing and non-dividing cells in each compartment was recorded. Each dividing cell c that was generated was assigned a current age A_c and a cell cycle time C_c, i.e. the age at which the cell will eventually divide. The current age was obtained by randomly drawing a number from an interval ranging from 0 hours to the mean cell cycle time (16.15 hours) obtained from experimental data, while the cell cycle was obtained by drawing a random number from a skew normal distribution, which was fitted to the experimental distribution of cell cycle times as shown in Figure S7.3.

Simulations were performed by iterating the following routine over time, until a total simulation time T was reached. At each iteration i, we found the cell c_i that was due to divide next, and a time step Δt_i was defined by the time remaining for this cell to divide, i.e. $\Delta t_i = \min_c(C_c - A_c)$. Then, the ages of all dividing cells were updated and the division of cell c_i was executed. This was done by randomly choosing one of the three division modes defined in Figure 7.4A, according to the probabilities determined by the parameters α and ϕ of the compartment to which the cell belonged. Any dividing daughters that were born were initialized with age zero and a random cell cycle time drawn as described before. If the dividing cell belonged to the proliferative compartment, a random cell within the compartment was chosen and was transferred to the differentiation compartment. Finally, the number of dividing and non-dividing cells in each compartment was updated accordingly.

For some parameter values, simulations were ended earlier than the total time T. This occurred when no dividing cells were left in either compartment (defined as a depletion event), or when the number of dividing cells reached an arbitrarily set maximum limit of five times its initial value (defined as an overgrowth event, occurring only in the one-compartment model). In these cases, simulations were restarted until a total simulation time T was reached, and the total number of events was recorded.

The same routine was used for both the one- and the two-compartment models, as the two-compartment case reduces to the one-compartment condition when the parameter values of both compartments are equal. However, for the one compartment model, the initial number of dividing cells was given a fixed value, since Equation 7.3 has no solution when $\alpha_d = 0$.

To obtain statistics regarding fluctuations in the number of dividing cells D through time, at each iteration i we kept track of the number of dividing cells in the proliferative compartment d_i^p and in the differentiation compartment d_i^d. With these quantities, we could compute the standard deviation σ of D according to

$$\sigma^2 = \langle D^2 \rangle - \langle D \rangle^2. \tag{7.4}$$

Given that $D = D_p + D_d$, where D_p and D_d are the number of dividing cells in the proliferative and differentiation compartments, σ can be expressed as

$$\sigma^2 = \langle D_p^2 \rangle - \langle D_p \rangle^2 + \langle D_d^2 \rangle - \langle D_d \rangle^2 + 2\langle D_p D_d \rangle - 2\langle D_p \rangle \langle D_d \rangle, \tag{7.5}$$

where

$$\langle D_{p,d} \rangle = \sum_i \frac{d_i^{p,d} \Delta t_i}{T}, \tag{7.6}$$

$$\langle D_{p,d}^2 \rangle = \sum_i \frac{(d_i^{p,d})^2 \Delta t_i}{T}, \text{ and} \tag{7.7}$$

$$\langle D_p D_d \rangle = \sum_i \frac{d_i^p d_i^d \Delta t_i}{T}. \tag{7.8}$$

Finally, the coefficient of variation CV of D was given by

$$CV_D = \frac{\sigma}{\langle D \rangle}. \tag{7.9}$$

An overview of the parameters used in the simulations is given below.

One-compartment model

Parameter	Definition	Values
D_0	Initial number of dividing cells	30
α	Growth rate	0
T	Total simulation time	10^6 h
ϕ	Degree of symmetry	$\in [0, 1]$

Two-compartment model

Parameter	Definition	Values
S	Size of proliferative compartment	30
T	Total simulation time	10^5 h
α_p	Growth rate of proliferative compartment	$\in (0, 1]$
α_d	Growth rate of differentiation compartment	$\in [-1, 0)$
ϕ	Degree of symmetry of both compartments	$\in [0, 1]$

7.5   Appendix

7.5.1   Author contributions to the chapter

GHP, SJT and JSvZ designed the experimental strategy. **GHP** performed the experiments. **GHP**, YJG and RNUK performed single-cell tracking. **GHP**, RNUK and XZ analyzed tracking data. JSvZ constructed the computational model. **GHP** and JSvZ performed simulations and model analysis. **GHP** wrote the text. SJT and JSvZ supervised the study.

7.5.2   Additional figures
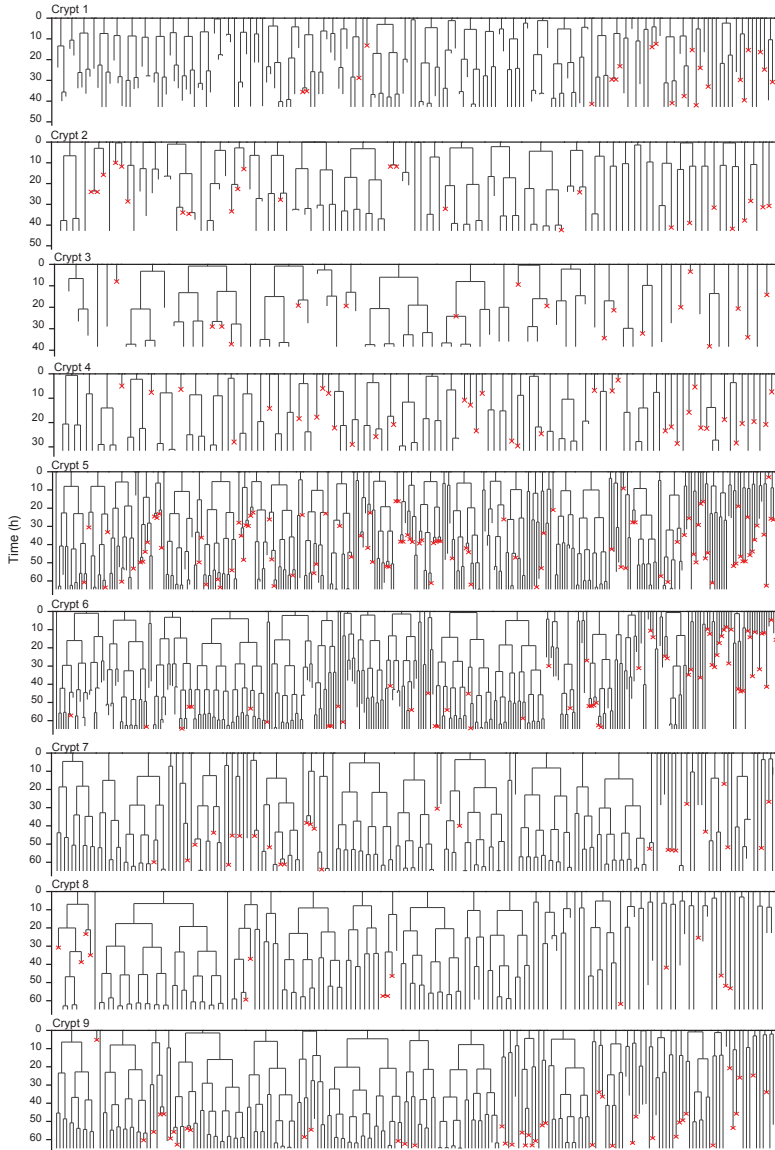
Figure S7.1 Lineage trees of all tracked cells

Lineage trees of cells tracked in nine different crypts. Cells in the initial time point are ordered according to their distance to the crypt base. Red crosses indicate cell deaths and incomplete lines indicate cells that could not be accurately traced further due to insufficient fluorescence intensity or movement outside of the field of view.
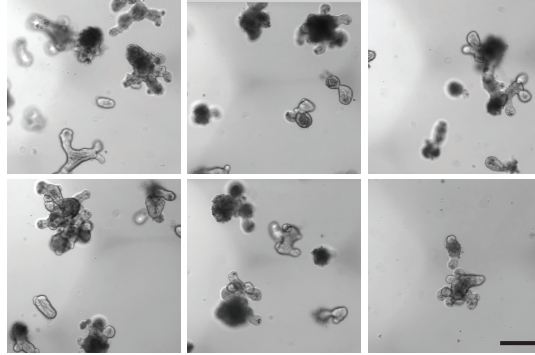
Figure S7.2 Intestinal organoid heterogeneity

Sample bright-field images of murine intestinal organoids showcasing their wide variability in size, shape and number of crypts. Scale bar is 200 µm.
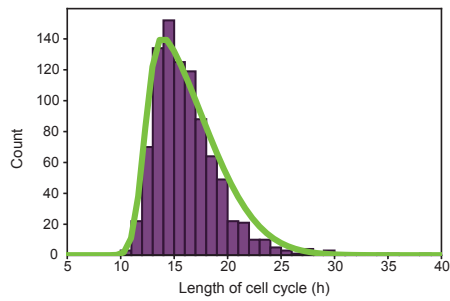
Figure S7.3 Cell cycle distribution

Histogram of cell cycle times of all tracked dividing cells. Green line represents a skew normal distribution fitted to the data, with parameters: shape = 6.1, location = 12.2 h, and scale = 5.2 h.
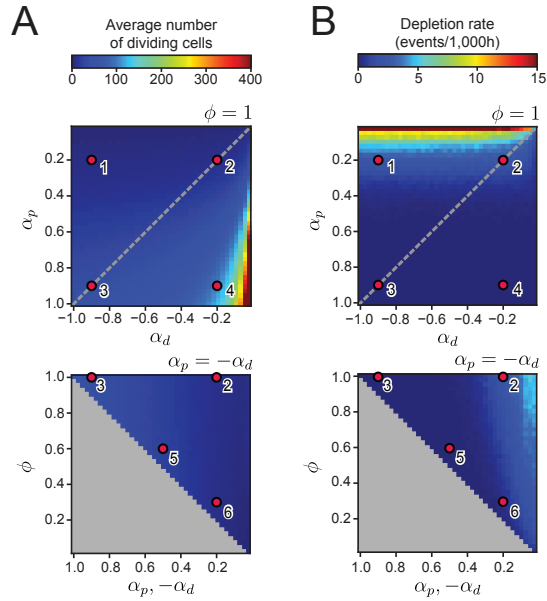
Figure S7.4 Two-compartment model

A Average number of dividing cells D obtained from the two-compartment model. Top panel shows the effects of varying the growth rates of both compartments when all divisions are symmetric ($\phi = 1$), and bottom panel shows the effects of varying the degree of symmetry when both compartments have opposite growth rates ($\alpha_p = -\alpha_d$, dashed line in top panel). The grey region in bottom panel corresponds to inaccessible parameter space.

B Rate at which dividing cells were depleted. Every time a simulation ended due to depletion, a new simulation was started until a total simulation time of 10^6 hours was reached. Thus, the rate refers to the number of times simulations had to be restarted for each value of the parameters divided by the total simulation time.

8

Implications for society

Scientific and technical advances of society are never the result of a single endeavor; instead, they usually come as the result of a series of efforts, some big and some small, that build upon each other to create and to innovate. While individually, each effort might be of little use or have no apparent application, their worth becomes evident only later, when they help lay the foundations for new perspectives. In this thesis, we have explored four tiny of such efforts, some with clear and some with not-so-clear implications for society. Nonetheless, they all add valuable knowledge towards our general understanding of animal biology, which is in turn the basis for any advancement in medicine and healthcare.

In Chapter 3, we proposed a mechanism through which the development of the *C. elegans* vulva progresses in a highly reproducible manner regardless of strong animal-to-animal variability. Despite the evident anatomical differences between these worms and higher species, the mechanisms that cells use to communicate with each other and their surroundings during development, namely Ras and Notch signaling, are remarkably similar among animals. Thus, our findings bring us a step closer to understanding animal development in general, as our proposed mechanism might also be exploited by other animals when they are faced with variable conditions during their development. Ultimately, advances in our understanding of animal development are of paramount importance as they hold the key for novel therapeutic strategies for tissue repair and regeneration.

In Chapter 5, we studied the effects that the respiratory syncytial virus (RSV) has on epithelial cells of the human airway. RSV infections are a major burden for healthcare systems worldwide since they are the main reason for hospitalization due to respiratory illness, with potentially fatal

consequences in infants and immunocompromised individuals. Effective vaccines and treatments are not available, partly due to a lack of understanding of the epithelial response to infection. Our research showed that airway organoids are an ideal model system to study RSV infection at the single-cell level. We propose that infection might cause changes in the migratory behavior of cells, which in turn result in collective motion arising at larger scales. Further research in our lab will build upon these results with the aim of elucidating the mechanisms that lead to such migratory changes and the role they play during disease. This research will hopefully expand our knowledge about the airway response to RSV infection and offer new insights into potential treatments and preventive measures.

In Chapter 6, we showed that antifreeze glycoproteins (AFGPs) offer considerable protection to intestinal organoids upon storage under hypothermic conditions, and that such protective action could be the result of a direct interaction between AFGPs and cell membranes. Our results highlight organoids as an attractive model to study the effects of AFGPs and other antifreeze proteins in multicellular systems when stored in cold conditions. Further research combining organoids and AFGPs could aid in the development of novel protocols for hypothermic storage of large multicellular assemblies, which could eventually lead to successful long-term storage of whole organs. Transplantation is sometimes the most appropriate treatment in cases of organ dysfunction; however, donor organ supply is greatly limited by the short time scales that organs remain viable after a donor is deceased. Therefore, the development of any technique that can prolong organ storage by even a few hours could have a massive impact on the health of the numerous people who are in need of a new organ.

Finally, in Chapter 7 we looked at how homeostasis is achieved in intestinal organoids. Our results suggest that high fractions of symmetric divisions could be a mechanism in place to minimize fluctuations in the number of dividing cells, and therefore maintain a proper balance between cell proliferation and differentiation. Moreover, upcoming results from an ongoing collaboration with the van Rheenen lab will reveal if such a mechanism is also present in the intestine *in vivo*. This study expands on our knowledge regarding our currently incomplete view of how adult tissues maintain homeostasis despite high cellular turnover rates. Disease is commonly the result of an imbalance between cell proliferation and differentiation; in particular, cancer can be associated with excessive proliferation resulting in aberrant growth of tissues, while aging can be associated with tissue degeneration that comes as a consequence of decreasing proliferation

rates. Insights into the mechanisms that allow such a balance to be achieved in healthy tissues could provide clues about their fragilities and how they lead to disease, which in turn could be exploited for the development of novel therapeutic approaches.

References

[1] S. Brenner, "The genetics of behaviour," *British medical bulletin*, vol. 29, no. 3, pp. 269–271, 1973.

[2] D. L. Riddle, T. Blumenthal, B. J. Meyer, and J. R. Priess, "Introduction to c. elegans–c. elegans ii," 1997.

[3] A. K. Corsi, B. Wightman, and M. Chalfie, "A transparent window into biology: a primer on caenorhabditis elegans," *Genetics*, vol. 200, no. 2, pp. 387–407, 2015.

[4] Z. Altun and D. Hall, "Introduction to c. elegans anatomy," *In WormAtlas*, 2009.

[5] J. E. Sulston, E. Schierenberg, J. G. White, and J. Thomson, "The embryonic cell lineage of the nematode caenorhabditis elegans," *Developmental biology*, vol. 100, no. 1, pp. 64–119, 1983.

[6] A. Raj and A. van Oudenaarden, "Nature, nurture, or chance: stochastic gene expression and its consequences," *Cell*, vol. 135, no. 2, pp. 216–226, 2008.

[7] M. L. Begasse and A. A. Hyman, "The first cell cycle of the caenorhabditis elegans embryo: Spatial and temporal control of an asymmetric cell division," *Cell Cycle in Development*, pp. 109–133, 2011.

[8] P. W. Sternberg, "Vulval development," *WormBook*, vol. 25, pp. 1–28, 2005.

[9] C. H. WADDINGTON, "Canalization of development and the inheritance of acquired characters," *Nature*, vol. 150, pp. 563–565, Nov 1942.

[10] C. H. Waddington *et al.*, "The strategy of the genes. a discussion of some aspects of theoretical biology. with an appendix by h. kacser.," *The strategy of the genes. A discussion of some aspects of theoretical biology. With an appendix by H. Kacser.*, 1957.

[11] J. Stelling, U. Sauer, Z. Szallasi, F. J. Doyle III, and J. Doyle, "Robustness of cellular functions," *Cell*, vol. 118, no. 6, pp. 675–685, 2004.

[12] J. E. Ferrell Jr, "Bistability, bifurcations, and waddington's epigenetic landscape," *Current biology*, vol. 22, no. 11, pp. R458–R466, 2012.

[13] S. Huang, "The molecular and mathematical basis of waddington's epigenetic landscape: A framework for post-darwinian biology?,"

BioEssays, vol. 34, pp. 149–157, Nov 2011.

[14] M. Manu, S. Surkova, A. V. Spirov, V. Gursky, H. Janssens, A.-R. Kim, O. Radulescu, C. E. Vanario-Alonso, D. H. Sharp, M. Samsonova, *et al.*, "Canalization of gene expression and domain shifts in the drosophila blastoderm by dynamical attractors," *PLoS Computational Biology*, vol. 5, p. 3, 2009.

[15] S. Surkova, A. V. Spirov, V. V. Gursky, H. Janssens, A.-R. Kim, O. Radulescu, C. E. Vanario-Alonso, D. H. Sharp, M. Samsonova, J. Reinitz, *et al.*, "Canalization of gene expression in the drosophila blastoderm by gap gene cross regulation," *PLoS biology*, vol. 7, no. 3, p. e1000049, 2009.

[16] J. Gavin-Smyth, Y.-C. Wang, I. Butler, and E. L. Ferguson, "A genetic network conferring canalization to a bistable patterning system in drosophila," *Current Biology*, vol. 23, no. 22, pp. 2296–2302, 2013.

[17] C. Braendle and M.-A. Félix, "Plasticity and errors of a robust developmental system in different environments," *Developmental Cell*, vol. 15, no. 5, pp. 714 – 724, 2008.

[18] S. Grimbert and C. Braendle, "Cryptic genetic variation uncovers evolution of environmentally sensitive parameters incaenorhabditisvulval development," *Evolution and Development*, vol. 16, pp. 278–291, Aug 2014.

[19] M.-A. Félix and M. Barkoulas, "Robustness and flexibility in nematode vulva development," *Trends in Genetics*, vol. 28, no. 4, pp. 185–195, 2012.

[20] A. S. Yoo, "Crosstalk between the egfr and lin-12/notch pathways in c. elegans vulval development," *Science*, vol. 303, pp. 663–666, Jan 2004.

[21] J. S. van Zon, S. Kienle, G. Huelsz-Prince, M. Barkoulas, and A. van Oudenaarden, "Cells change their sensitivity to an egf morphogen gradient to control egf-induced gene expression," *Nature Communications*, vol. 6, May 2015.

[22] J. Kimble and D. Hirsh, "The postembryonic cell lineages of the hermaphrodite and male gonads in caenorhabditis elegans," *Developmental biology*, vol. 70, no. 2, pp. 396–417, 1979.

[23] S. Grimbert, K. Tietze, M. Barkoulas, P. W. Sternberg, M.-A. Félix, and C. Braendle, "Anchor cell signaling and vulval precursor cell positioning establish a reproducible spatial context during c. elegans

vulval induction," *Developmental Biology*, vol. 416, no. 1, pp. 123 – 135, 2016.

[24] N. Chen and I. Greenwald, "The lateral signal for lin-12/notch in c. elegans vulval development comprises redundant secreted and transmembrane dsl proteins," *Developmental cell*, vol. 6, no. 2, pp. 183–192, 2004.

[25] X. Zhang and I. Greenwald, "Spatial regulation oflag-2transcription during vulval precursor cell fate patterning incaenorhabditiseleganslag-2," *Genetics*, vol. 188, pp. 847–858, May 2011.

[26] A. Raj, P. Van Den Bogaard, S. A. Rifkin, A. Van Oudenaarden, and S. Tyagi, "Imaging individual mrna molecules using multiple singly labeled probes," *Nature methods*, vol. 5, no. 10, p. 877, 2008.

[27] N. Ji and A. Van Oudenaarden, "Single molecule fluorescent in situ hybridization (smfish) of c. elegans worms and embryos," WormBook, 2012.

[28] J. H. Thomas, M. J. Stern, and H. Horvitz, "Cell interactions coordinate the development of the c. elegans egg-laying system," *Cell*, vol. 62, no. 6, pp. 1041 – 1052, 1990.

[29] B. J. Hwang and P. W. Sternberg, "A cell-specific enhancer that specifies lin-3 expression in the c. elegans anchor cell for vulval development," *Development*, vol. 131, no. 1, pp. 143–151, 2004.

[30] I. S. Greenwald, P. W. Sternberg, and H. R. Horvitz, "The lin-12 locus specifies cell fates in caenorhabditis elegans," *Cell*, vol. 34, no. 2, pp. 435–444, 1983.

[31] P. W. Sternberg and H. Horvitz, "The combined action of two intercellular signaling pathways specifies three cell fates during vulval induction in c. elegans," *Cell*, vol. 58, no. 4, pp. 679 – 693, 1989.

[32] P. W. Sternberg and H. Horvitz, "Pattern formation during vulval development in c. elegans," *Cell*, vol. 44, no. 5, pp. 761 – 772, 1986.

[33] A. G. Fletcher, M. Osterfield, R. E. Baker, and S. Y. Shvartsman, "Vertex models of epithelial morphogenesis," *Biophysical journal*, vol. 106, no. 11, pp. 2291–2304, 2014.

[34] N. J. Savill and P. Hogeweg, "Modelling morphogenesis: from single cells to crawling slugs," *Journal of theoretical biology*, vol. 184, no. 3, pp. 229–235, 1997.

[35] A. Szabó, R. Ünnep, E. Méhes, W. O. Twal, W. S. Argraves, Y. Cao,

and A. Czirók, "Collective cell motion in endothelial monolayers," *Physical Biology*, vol. 7, p. 046007, Nov 2010.

[36] M. Sundaram and I. Greenwald, "Genetic and phenotypic studies of hypomorphic lin-12 mutants in caenorhabditis elegans.," *Genetics*, vol. 135, no. 3, pp. 755–763, 1993.

[37] M. Wang and P. W. Sternberg, "Patterning of the c. elegans 1 degrees vulval lineage by ras and wnt pathways," *Development*, vol. 127, no. 23, pp. 5047–5058, 2000.

[38] J. L. Green, T. Inoue, and P. W. Sternberg, "Opposing wnt pathways orient cell polarity during organogenesis," *Cell*, vol. 134, no. 4, pp. 646–656, 2008.

[39] A. P. Newman, J. G. White, and P. W. Sternberg, "Morphogenesis of the c. elegans hermaphrodite uterus," *Development*, vol. 122, no. 11, pp. 3617–3626, 1996.

[40] D. R. Sherwood and P. W. Sternberg, "Anchor cell invasion into the vulval epithelium in c. elegans," *Developmental cell*, vol. 5, no. 1, pp. 21–31, 2003.

[41] M.-A. Félix and P. W. Sternberg, "Two nested gonadal inductions of the vulva in nematodes," *Development*, vol. 124, no. 1, pp. 253–259, 1997.

[42] M.-A. Félix, P. De Ley, R. J. Sommer, L. Frisse, S. A. Nadler, W. K. Thomas, J. Vanfleteren, and P. W. Sternberg, "Evolution of vulva development in the cephalobina (nematoda)," *Developmental biology*, vol. 221, no. 1, pp. 68–86, 2000.

[43] D. Sutherland, C. Samakovlis, and M. A. Krasnow, "branchless encodes a drosophila fgf homolog that controls tracheal cell migration and the pattern of branching," *Cell*, vol. 87, no. 6, pp. 1091 – 1101, 1996.

[44] T. Ikeya and S. Hayashi, "Interplay of notch and fgf signaling restricts cell fate and mapk activation in the drosophila trachea," *Development*, vol. 126, no. 20, pp. 4455–4463, 1999.

[45] A. S. Ghabrial and M. A. Krasnow, "Social interactions among epithelial cells during tracheal branching morphogenesis," *Nature*, vol. 441, no. 7094, p. 746, 2006.

[46] A. Ochoa-Espinosa and M. Affolter, "Branching morphogenesis: from cells to organs and back," *Cold Spring Harbor perspectives in biology*, p. a008243, 2012.

[47] J. S. Simske and S. K. Kirn, "Sequential signalling during caenorhabditis elegans vulval induction," *Nature*, vol. 375, no. 6527, pp. 142–146, 1995.

[48] D. Jacobs, G. J. Beitel, S. G. Clark, H. R. Horvitz, and K. Kornfeld, "Gain-of-function mutations in the caenorhabditis elegans lin-1 ets gene identify a c-terminal regulatory domain phosphorylated by erk map kinase," *Genetics*, vol. 149, no. 4, pp. 1809–1822, 1998.

[49] S. Brenner, "The genetics of caenorhabditis elegans," *Genetics*, vol. 77, no. 1, pp. 71–94, 1974.

[50] A. D. Edelstein, M. A. Tsuchida, N. Amodaj, H. Pinkard, R. D. Vale, and N. Stuurman, "Advanced methods of microscope control using µmanager software," *Journal of biological methods*, vol. 1, no. 2, 2014.

[51] T. Berset, E. F. Hoier, G. Battu, S. Canevascini, and A. Hajnal, "Notch inhibition of ras signaling through map kinase phosphatase lip-1 during c. elegans vulval development," *Science*, vol. 291, no. 5506, pp. 1055–1058, 2001.

[52] C. W. Whitfield, C. Bénard, T. Barnes, S. Hekimi, and S. K. Kim, "Basolateral localization of the caenorhabditis elegans epidermal growth factor receptor in epithelial cells by the pdz protein lin-10," *Molecular Biology of the Cell*, vol. 10, pp. 2087–2100, Jun 1999.

[53] O. Skorobogata, J. M. Escobar-Restrepo, and C. E. Rocheleau, "An agef-1/arf gtpase/ap-1 ensemble antagonizes let-23 egfr basolateral localization and signaling during c. elegans vulva induction," *PLoS genetics*, vol. 10, no. 10, p. e1004728, 2014.

[54] A. Haag, P. Gutierrez, A. Bühler, M. Walser, Q. Yang, M. Langouët, D. Kradolfer, E. Fröhli, C. J. Herrmann, A. Hajnal, and et al., "An in vivo egf receptor localization screen in c. elegans identifies the ezrin homolog erm-1 as a temporal regulator of signaling," *PLoS Genetics*, vol. 10, p. e1004341, May 2014.

[55] W. H. Press, S. A. Teukolsky, W. T. Vetterling, and B. P. Flannery, *Numerical Recipes in C*. Cambridge University Press, second ed., 1996.

[56] N. M. editorial, "Method of the year 2017: Organoids," *Nature Methods*, vol. 15, pp. 1–1, Jan 2018.

[57] J. R. Spence, "Taming the wild west of organoids, enteroids, and mini-guts," *Cellular and molecular gastroenterology and hepatology*, vol. 5, no. 2, pp. 159–160, 2018.

[58] J. Magney, S. Erlandsen, M. L. Bjerknes, and H. Cheng, "Scanning electron microscopy of isolated epithelium of the murine gastrointestinal tract: Morphology of the basal surface and evidence for paracrine-like cells," *American journal of anatomy*, vol. 177, no. 1, pp. 43–53, 1986.

[59] T. Sato, R. G. Vries, H. J. Snippert, M. Van De Wetering, N. Barker, D. E. Stange, J. H. Van Es, A. Abo, P. Kujala, P. J. Peters, *et al.*, "Single lgr5 stem cells build crypt–villus structures in vitro without a mesenchymal niche," *Nature*, vol. 459, no. 7244, p. 262, 2009.

[60] A. Fatehullah, S. H. Tan, and N. Barker, "Organoids as an in vitro model of human development and disease," *Nature Cell Biology*, vol. 18, pp. 246–254, Mar 2016.

[61] S. A. Taleb, A. A. Al Thani, K. Al Ansari, and H. M. Yassine, "Human respiratory syncytial virus: pathogenesis, immune responses, and current vaccine approaches," *European Journal of Clinical Microbiology & Infectious Diseases*, pp. 1–11, 2018.

[62] A. R. Falsey, P. A. Hennessey, M. A. Formica, C. Cox, and E. E. Walsh, "Respiratory syncytial virus infection in elderly and high-risk adults," *New England Journal of Medicine*, vol. 352, no. 17, pp. 1749–1759, 2005.

[63] M. K. Lay, P. A. González, M. A. León, P. F. Céspedes, S. M. Bueno, C. A. Riedel, and A. M. Kalergis, "Advances in understanding respiratory syncytial virus infection in airway epithelial cells and consequential effects on the immune response," *Microbes and infection*, vol. 15, no. 3, pp. 230–242, 2013.

[64] A. T. Borchers, C. Chang, M. E. Gershwin, and L. J. Gershwin, "Respiratory syncytial virusa comprehensive review," *Clinical reviews in allergy & immunology*, vol. 45, no. 3, pp. 331–379, 2013.

[65] Y.-W. Chen, S. X. Huang, A. L. R. T. De Carvalho, S.-H. Ho, M. N. Islam, S. Volpi, L. D. Notarangelo, M. Ciancanelli, J.-L. Casanova, J. Bhattacharya, *et al.*, "A three-dimensional model of human lung development and disease from pluripotent stem cells," *Nature cell biology*, vol. 19, no. 5, p. 542, 2017.

[66] B. D. Persson, A. B. Jaffe, R. Fearns, and H. Danahay, "Respiratory syncytial virus can infect basal cells and alter human airway epithelial differentiation," *PloS one*, vol. 9, no. 7, p. e102368, 2014.

[67] M. L. Fulcher, S. Gabriel, K. A. Burns, J. R. Yankaskas, and S. H. Randell, "Well-differentiated human airway epithelial cell cultures,"

in *Human Cell Culture Protocols*, pp. 183–206, Springer, 2005.

[68] C. E. Barkauskas, M.-I. Chung, B. Fioret, X. Gao, H. Katsura, and B. L. Hogan, "Lung organoids: current uses and future promise," *Development*, vol. 144, no. 6, pp. 986–997, 2017.

[69] R. M. Liesman, U. J. Buchholz, C. L. Luongo, L. Yang, A. D. Proia, J. P. DeVincenzo, P. L. Collins, and R. J. Pickles, "Rsv-encoded ns2 promotes epithelial cell shedding and distal airway obstruction," *Journal of Clinical Investigation*, vol. 124, pp. 2219–2233, Apr 2014.

[70] M. Teng and P. Collins, "Altered growth characteristics of recombinant respiratory syncytial viruses which do not produce ns2 protein," *Journal of Virology*, vol. 73, no. 1, pp. 466–473, 1999.

[71] P. Rørth, "Collective cell migration," *Annual Review of Cell and Developmental Biology*, vol. 25, pp. 407–429, Nov 2009.

[72] T. Vicsek, "Novel type of phase transition in a system of self-driven particles," *Physical Review Letters*, vol. 75, no. 6, pp. 1226–1229, 1995.

[73] R. Sknepnek, "Active swarms on a sphere," *Physical Review E*, vol. 91, no. 2, 2015.

[74] R. J. Renka, "Algorithm 772: Stripack: Delaunay triangulation and voronoi diagram on the surface of a sphere," *ACM Transactions on Mathematical Software (TOMS)*, vol. 23, no. 3, pp. 416–434, 1997.

[75] A. Ridley, M. Schwartz, K. Burridge, R. Firtel, M. Ginsberg, G. Borisy, J. Parsons, and A. Horwitz, "Cell migration: Integrating signals from front to back," *Science*, vol. 302, no. 5651, pp. 1704–1709, 2003.

[76] B. Rubinsky, "Principles of low temperature cell preservation," *Heart Failure Reviews*, vol. 8, pp. 277–284, Jul 2003.

[77] A. J. Mathew, J. M. Baust, R. G. Van Buskirk, and J. G. Baust, "Cell preservation in reparative and regenerative medicine: Evolution of individualized solution composition," *Tissue Engineering*, vol. 10, pp. 1662–1671, Nov 2004.

[78] A. L. DeVries and D. E. Wohlschlag, "Freezing resistance in some antarctic fishes," *Science*, vol. 163, pp. 1073–1075, Mar 1969.

[79] J. G. Duman, "Antifreeze and ice nucleator proteins in terrestrial arthropods," *Annual Review of Physiology*, vol. 63, pp. 327–357, Mar 2001.

[80] L. L. C. Olijve, K. Meister, A. L. DeVries, J. G. Duman, S. Guo, H. J.

Bakker, and I. K. Voets, "Blocking rapid ice crystal growth through nonbasal plane adsorption of antifreeze proteins," *Proceedings of the National Academy of Sciences*, vol. 113, pp. 3740–3745, Mar 2016.

[81] J. A. Raymond and A. L. DeVries, "Adsorption inhibition as a mechanism of freezing resistance in polar fishes.," *Proceedings of the National Academy of Sciences*, vol. 74, pp. 2589–2593, Jun 1977.

[82] G. Amir, L. Horowitz, B. Rubinsky, B. S. Yousif, J. Lavee, and A. K. Smolinsky, "Subzero nonfreezing cryopresevation of rat hearts using antifreeze protein I and antifreeze protein III," *Cryobiology*, vol. 48, no. 3, pp. 273 – 282, 2004.

[83] H. H. Lee, H. J. Lee, H. J. Kim, J. H. Lee, Y. Ko, S. M. Kim, J. R. Lee, C. S. Suh, and S. H. Kim, "Effects of antifreeze proteins on the vitrification of mouse oocytes: comparison of three different antifreeze proteins," *Human Reproduction*, vol. 30, pp. 2110–2119, Jul 2015.

[84] T. Kamijima, M. Sakashita, A. Miura, Y. Nishimiya, and S. Tsuda, "Antifreeze protein prolongs the life-time of insulinoma cells during hypothermic preservation," *PLoS ONE*, vol. 8, p. e73643, Sep 2013.

[85] F. Tablin, A. E. Oliver, N. J. Walker, L. M. Crowe, and J. H. Crowe, "Membrane phase transition of intact human platelets: Correlation with cold-induced activation," *Journal of Cellular Physiology*, vol. 168, pp. 305–313, Aug 1996.

[86] B. Rubinsky, A. Arav, and G. Fletcher, "Hypothermic protection — a fundamental property of "antifreeze" proteins," *Biochemical and Biophysical Research Communications*, vol. 180, no. 2, pp. 566 – 571, 1991.

[87] B. Rubinsky, A. Arav, J. Hong, and C. Lee, "Freezing of mammalian livers with glycerol and antifreeze proteins," *Biochemical and Biophysical Research Communications*, vol. 200, no. 2, pp. 732 – 741, 1994.

[88] T. Wang, Q. Zhu, X. Yang, J. R. Layne, and A. L. Devries, "Antifreeze glycoproteins from antarctic notothenioid fishes fail to protect the rat cardiac explant during hypothermic and freezing preservation," *Cryobiology*, vol. 31, no. 2, pp. 185 – 192, 1994.

[89] S. Martínez-Páramo, V. Barbosa, S. Pérez-Cerezales, V. Robles, and M. Herráez, "Cryoprotective effects of antifreeze proteins delivered into zebrafish embryos," *Cryobiology*, vol. 58, no. 2, pp. 128 – 133, 2009.

[90] K. Kretzschmar and H. Clevers, "Organoids: modeling development and the stem cell niche in a dish," *Developmental cell*, vol. 38, no. 6, pp. 590–600, 2016.

[91] K. Meister, A. L. DeVries, H. J. Bakker, and R. Drori, "Antifreeze glycoproteins bind irreversibly to ice," *Journal of the American Chemical Society*, vol. 140, no. 30, pp. 9365–9368, 2018.

[92] C. Budke, A. Dreyer, J. Jaeger, K. Gimpel, T. Berkemeier, A. S. Bonin, L. Nagel, C. Plattner, A. L. DeVries, N. Sewald, *et al.*, "Quantitative efficacy classification of ice recrystallization inhibition agents," *Crystal Growth & Design*, vol. 14, no. 9, pp. 4285–4294, 2014.

[93] C. I. Biggs, T. L. Bailey, C. Stubbs, A. Fayter, M. I. Gibson, *et al.*, "Polymer mimics of biomacromolecular antifreezes," *Nature communications*, vol. 8, no. 1, p. 1546, 2017.

[94] C. C. Groot, K. Meister, A. L. DeVries, and H. J. Bakker, "Dynamics of the hydration water of antifreeze glycoproteins," *The journal of physical chemistry letters*, vol. 7, no. 23, pp. 4836–4840, 2016.

[95] S. Yui, L. Azzolin, M. Maimets, M. T. Pedersen, R. P. Fordham, S. L. Hansen, H. L. Larsen, J. Guiu, M. R. Alves, C. F. Rundsten, J. V. Johansen, Y. Li, C. D. Madsen, T. Nakamura, M. Watanabe, O. H. Nielsen, P. J. Schweiger, S. Piccolo, and K. B. Jensen, "Yap/taz-dependent reprogramming of colonic epithelium links ecm remodeling to tissue regeneration," *Cell Stem Cell*, vol. 22, no. 1, pp. 35 – 49.e7, 2018.

[96] N. Gjorevski, N. Sachs, A. Manfrin, S. Giger, M. E. Bragina, P. Ordóñez-Morán, H. Clevers, and M. P. Lutolf, "Designer matrices for intestinal stem cell and organoid culture," *Nature*, vol. 539, pp. 560–564, Nov 2016.

[97] N. R. Smith, J. R. Swain, P. S. Davies, A. C. Gallagher, M. S. Parappilly, C. Z. Beach, P. R. Streeter, I. A. Williamson, S. T. Magness, and M. H. Wong, "Monoclonal antibodies reveal dynamic plasticity between lgr5- and bmi1-expressing intestinal cell populations," *Cellular and Molecular Gastroenterology and Hepatology*, vol. 6, no. 1, pp. 79 – 96, 2018.

[98] A. Gregorieff, Y. Liu, M. R. Inanlou, Y. Khomchuk, and J. L. Wrana, "Yap-dependent reprogramming of lgr5+ stem cells drives intestinal regeneration and cancer," *Nature*, vol. 526, pp. 715–718, Oct 2015.

[99] J. F. Dekkers, C. L. Wiegerinck, H. R. de Jonge, I. Bronsveld, H. M.

Janssens, K. M. de Winter-de Groot, A. M. Brandsma, N. W. M. de Jong, M. J. C. Bijvelds, B. J. Scholte, and et al., "A functional CFTR assay using primary cystic fibrosis intestinal organoids," *Nature Medicine*, vol. 19, pp. 939–945, Jun 2013.

[100] D. D. Zomer-van Ommen, A. V. Pukin, O. Fu, L. H. Quarles van Ufford, H. M. Janssens, J. M. Beekman, and R. J. Pieters, "Functional characterization of cholera toxin inhibitors using human intestinal organoids," *Journal of medicinal chemistry*, vol. 59, no. 14, pp. 6968–6972, 2016.

[101] A. M. Strubberg, J. Liu, N. M. Walker, C. D. Stefanski, R. J. MacLeod, S. T. Magness, and L. L. Clarke, "Cftr modulates wnt/-catenin signaling and stem cell proliferation in murine intestine," *Cellular and Molecular Gastroenterology and Hepatology*, vol. 5, no. 3, pp. 253 – 271, 2018.

[102] B. Rubinsky, M. Mattioli, A. Arav, B. Barboni, and G. Fletcher, "Inhibition of ca2+ and k+ currents by" antifreeze" proteins," *American Journal of Physiology-Regulatory, Integrative and Comparative Physiology*, vol. 262, no. 3, pp. R542–R545, 1992.

[103] B. Rubinsky, A. Arav, M. Mattioli, and A. L. Devries, "The effect of antifreeze glycopeptides on membrane potential changes at hypothermic temperatures," *Biochemical and biophysical research communications*, vol. 173, no. 3, pp. 1369–1374, 1990.

[104] L. M. Hays, R. E. Feeney, L. M. Crowe, J. H. Crowe, and A. E. Oliver, "Antifreeze glycoproteins inhibit leakage from liposomes during thermotropic phase transitions," *Proceedings of the National Academy of Sciences*, vol. 93, no. 13, pp. 6835–6840, 1996.

[105] M. M. Tomczak, D. K. Hincha, S. D. Estrada, W. F. Wolkers, L. M. Crowe, R. E. Feeney, F. Tablin, and J. H. Crowe, "A mechanism for stabilization of membranes at low temperatures by an antifreeze protein," *Biophysical journal*, vol. 82, no. 2, pp. 874–881, 2002.

[106] J. Garner, S. R. Inglis, J. Hook, F. Separovic, and M. M. Harding, "A solid-state nmr study of the interaction of fish antifreeze proteins with phospholipid membranes," *European Biophysics Journal*, vol. 37, no. 6, pp. 1031–1038, 2008.

[107] C. W. Evans, V. Gubala, R. Nooney, D. E. Williams, M. A. Brimble, and A. L. Devries, "How do antarctic notothenioid fishes cope with internal ice? a novel function for antifreeze glycoproteins," *Antarctic Science*, vol. 23, pp. 57–64, Sep 2010.

138

[108] M. M. Mahe, E. Aihara, M. A. Schumacher, Y. Zavros, M. H. Montrose, M. A. Helmrath, T. Sato, and N. F. Shroyer, "Establishment of gastrointestinal epithelial organoids," *Current Protocols in Mouse Biology*, pp. 217–240, Dec 2013.

[109] J. M. Widholm, "The use of fluorescein diacetate and phenosafranine for determining viability of cultured plant cells," *Stain Technology*, vol. 47, pp. 189–194, Jan 1972.

[110] R. W. Hoppe and B. D. Bavister, "Evaluation of the fluorescein diacetate (fda) vital dye viability test with hamster and bovine embryos," *Animal Reproduction Science*, vol. 6, no. 4, pp. 323–335, 1984.

[111] T. Grabinger, L. Luks, F. Kostadinova, C. Zimberlin, J. P. Medema, M. Leist, and T. Brunner, "Ex vivo culture of intestinal crypt organoids as a model system for assessing cell death induction in intestinal epithelial cells and enteropathy," *Cell death & disease*, vol. 5, no. 5, p. e1228, 2014.

[112] H. Clevers and F. M. Watt, "Defining adult stem cells by function, not by phenotype," *Annual Review of Biochemistry*, vol. 87, pp. 1015–1027, Jun 2018.

[113] H. Gehart and H. Clevers, "Tales from the crypt: new insights into intestinal stem cells," *Nature Reviews Gastroenterology and Hepatology*, vol. 16, pp. 19–34, Nov 2018.

[114] T. Sato, R. G. Vries, H. J. Snippert, M. van de Wetering, N. Barker, D. E. Stange, J. H. van Es, A. Abo, P. Kujala, P. J. Peters, and et al., "Single lgr5 stem cells build crypt-villus structures in vitro without a mesenchymal niche," *Nature*, vol. 459, pp. 262–265, Mar 2009.

[115] T. Sato, J. H. van Es, H. J. Snippert, D. E. Stange, R. G. Vries, M. van den Born, N. Barker, N. F. Shroyer, M. van de Wetering, and H. Clevers, "Paneth cells constitute the niche for lgr5 stem cells in intestinal crypts," *Nature*, vol. 469, pp. 415–418, Nov 2010.

[116] P. B. Winton DJ, "Stem-cell organization in mouse small intestine," *Proceedings of the Royal Society of London. Series B: Biological Sciences*, vol. 241, pp. 13–18, Jul 1990.

[117] E. D Williams, A. P Lowes, D. Williams, and G. T Williams, "A stem cell niche theory of intestinal crypt maintenance based on somatic mutation in colonic mucosa," *The American journal of pathology*, vol. 141, pp. 773–6, 11 1992.

[118] C. Lopez-Garcia, A. Klein, B. Simons, and D. Winton, "Intestinal

stem cell replacement follows a pattern of neutral drift," *Science*, vol. 330, no. 6005, pp. 822–825, 2010.

[119] H. J. Snippert, L. G. van der Flier, T. Sato, J. H. van Es, M. van den Born, C. Kroon-Veenboer, N. Barker, A. M. Klein, J. van Rheenen, B. D. Simons, and H. Clevers, "Intestinal crypt homeostasis results from neutral competition between symmetrically dividing lgr5 stem cells," *Cell*, vol. 143, no. 1, pp. 134 – 144, 2010.

[120] L. Ritsma, S. I. J. Ellenbroek, A. Zomer, H. J. Snippert, F. J. de Sauvage, B. D. Simons, H. Clevers, and J. van Rheenen, "Intestinal crypt homeostasis revealed at single-stem-cell level by in vivo live imaging," *Nature*, vol. 507, pp. 362–365, Feb 2014.

[121] B. D. Simons and H. Clevers, "Strategies for homeostatic stem cell self-renewal in adult tissues," *Cell*, vol. 145, no. 6, pp. 851 – 862, 2011.

[122] L. Ritsma, E. J. Steller, E. Beerling, C. J. Loomans, A. Zomer, C. Gerlach, N. Vrisekoop, D. Seinstra, L. van Gurp, R. Schäfer, *et al.*, "Intravital microscopy through an abdominal imaging window reveals a pre-micrometastasis stage during liver metastasis," *Science translational medicine*, vol. 4, no. 158, pp. 158ra145–158ra145, 2012.

[123] S. Date and T. Sato, "Mini-gut organoids: Reconstitution of the stem cell niche," *Annual Review of Cell and Developmental Biology*, vol. 31, pp. 269–289, Nov 2015.

[124] S. Itzkovitz, I. C. Blat, T. Jacks, H. Clevers, and A. van Oudenaarden, "Optimality in the development of intestinal crypts," *Cell*, vol. 148, no. 3, pp. 608 – 619, 2012.

[125] C. S. Hughes, L. M. Postovit, and G. A. Lajoie, "Matrigel: A complex protein mixture required for optimal growth of cell culture," *PROTEOMICS*, vol. 10, pp. 1886–1890, Feb 2010.

[126] N. Gjorevski and P. Ordóñez-Morán, "Intestinal stem cell niche insights gathered from both in vivo and novel in vitro models," *Stem Cells International*, vol. 2017, pp. 1–10, 2017.

[127] H. F. Farin, I. Jordens, M. H. Mosa, O. Basak, J. Korving, D. V. F. Tauriello, K. de Punder, S. Angers, P. J. Peters, M. M. Maurice, and et al., "Visualization of a short-range wnt gradient in the intestinal stem-cell niche," *Nature*, vol. 530, pp. 340–343, Feb 2016.

[128] S.-J. Dunn, J. Osborne, P. Appleton, and I. Näthke, "Combined changes in wnt signaling response and contact inhibition induce al-

tered proliferation in radiation-treated intestinal crypts," *Molecular biology of the cell*, vol. 27, no. 11, pp. 1863–1874, 2016.

[129] T. Carroll, A. Langlands, J. Osborne, I. Newton, P. Appleton, and I. Näthke, "Interkinetic nuclear migration and basal tethering facilitates post-mitotic daughter separation in intestinal organoids," *Journal of Cell Science*, vol. 130, no. 22, pp. 3862–3877, 2017.

[130] D. Stamataki, M. Holder, C. Hodgetts, R. Jeffery, E. Nye, B. Spencer-Dene, D. J. Winton, and J. Lewis, "Delta1 expression, cell cycle exit, and commitment to a specific secretory fate coincide within a few hours in the mouse intestinal stem cell system," *PLoS One*, vol. 6, no. 9, p. e24484, 2011.

[131] F. Ferraro, C. L. Celso, and D. Scadden, "Adult stem cells and their niches," *The Cell Biology of Stem Cells*, pp. 155–168, 2010.

[132] R. R. Stine and E. L. Matunis, "Stem cell competition: finding balance in the niche," *Trends in Cell Biology*, vol. 23, no. 8, pp. 357 – 364, 2013.

[133] A. Klein and B. Simons, "Universal patterns of stem cell fate in cycling adult tissues," *Development*, vol. 138, no. 15, pp. 3103–3111, 2011.

Summary

Throughout their lifetime, animals face a wide variety of biological challenges. Starting out as single cells, their first challenge is to undergo development and become fully grown and functional adults. Remarkably, this incredibly complex process occurs in a highly reproducible manner despite the huge variability in environmental, genetic and molecular fluctuations they encounter during their journey through development. However, the challenges do not end here; once animals become adults, their tissues are constantly subject to damage, either by external sources such as disease, or due to intrinsic causes such as cellular aging. Thus, adult tissues are constantly renewing themselves, and must do so in a tightly controlled manner in order to maintain homeostasis. In this thesis, we explore how animals cope with a few of such challenges with the help of two model systems, *C. elegans* worms and stem cell-derived organoids.

In the first part, we use *C. elegans* to study how development occurs in such a reproducible manner. We particularly focus on the formation of the worms' vulva, an essential component of their reproductive system. Here, the so called 'anchor cell' secretes an inductive signal that tells a set of six stem cell-like cells to differentiate according to the amount of signal they receive. Stem cells that are located closer to the anchor cell receive a high signal and become part of the vulva, while those farther away receive less input and become part of the skin. Surprisingly, we found that the position of the anchor cell within the body of different animals was highly variable, which in turn caused the stem cells to receive diverging signal levels; yet, most worms were able to develop an invariant vulva. To investigate how such an invariant outcome could result from highly variable initial configurations, we combined experimental analysis of gene expression dynamics and mathematical modeling. Our results indicated that for an invariant vulva to arise, stem cells must not only receive a signal from the anchor cell, but should also communicate with one another and migrate to find their optimal position with respect to the anchor cell. Finally, our results propose a mechanism that could provide robustness to other developmental systems in which the source of an inductive signal might show similar positional variability.

In the second part, we turn our attention organoids: stem cell-derived

three-dimensional assemblies of cells that are grown *in vitro* and recapitulate essential features of organs. In Chapter 5, we use human airway organoids to study how the airway epithelium responds to infection by the respiratory syncytial virus (RSV). RSV is a leading cause of acute respiratory illness and, unfortunately, effective vaccines and treatments are lacking. How RSV infection affects the epithelium at the single-cell level is poorly understood. Here, we show that airway organoids provide an ideal platform to address this question. Time-lapse images revealed that organoids become highly motile upon RSV infection, with some of them surprisingly showing a coordinated rotational motion. Combining single-cell tracking and mathematical modeling, we show that such motion could result from an increase in cell persistence, i.e. a higher tendency for cells to maintain their direction of motion, and of cell-cell communication. Further research in our labs aims to confirm this hypothesis and to unravel the essential mechanisms that lead to such organoid motility. These results will hopefully provide novel insights into the airway response to RSV and into potential treatments.

In Chapter 6, we study the effects of antifreeze glycoproteins (AFGPs) on the preservation of intestinal organoids at cold temperatures. AFGPs have evolved as an adaptation in numerous animals living in cold and icy environments, preventing them from freezing at subzero temperatures by inhibiting ice formation. Recent research has surprisingly revealed that AFGPs can also protect mammalian cells and organs when stored at low temperatures, allowing them to survive for considerable periods of time. However, the mechanisms by which AFGPs exert such protective action are still unknown. In our study, we found that intestinal organoids could be stored for longer time periods under hypothermic conditions when AFGPs were present, and that AGFPs primarily localized to cell outlines, suggesting a protective action of AFGPs that could result from their direct interaction with cell membranes. Our research shows that organoids provide a flexible and previously inaccessible way of studying the effects of AFGPs in multicellular systems, which could bring us a step closer to successful cryopreservation of entire organs.

Finally, in Chapter 7, we investigate adult tissue renewal and homeostasis. Many adult organs are constantly replacing old and damaged cells through continuously-dividing stem cells. Proliferation and differentiation of these cells must be tightly regulated as any imbalance would lead to aberrant growth or to tissue degeneration. However, how such a tight balance is achieved in organs is still a fundamental open question. To address

this question, we combine experiments on mouse intestinal organoids with computational modeling. Time-lapse microscopy and single-cell tracking in growing organoids allowed us an unprecedented view of lineage dynamics in the intestinal epithelium. This revealed that organoid growth is highly regulated and that cell divisions in crypts are mostly symmetrical, i.e. with similar sister cell outcomes. A computational model provided a potential explanation the high degree of symmetry observed, as it showed that high fractions of symmetric divisions resulted in the smallest fluctuations in the number of dividing cells. Hence, such symmetry might be a mechanism in place to minimize variability and ensure homeostasis. Our results suggest a concrete mechanism through which the intestinal epithelium and other tissues might achieve a tight balance between proliferation and differentiation.

Samenvatting

Om te overleven moeten dieren verschillende uitdagingen overwinnen. De eerste uitdaging is om zich te ontwikkelen van slechts n cel tot een volgroeid en functionerend wezen. Opmerkelijk genoeg verloopt dit uiterst ingewikkelde proces elke keer op exact dezelfde wijze, ondanks dat er enorme variatie zit in de omgeving, de genen en de moleculen. Echter, ook zodra dieren volwassen zijn houden de uitdagingen nog niet op. Het dierenweefsel staat nog altijd bloot aan schade, ofwel veroorzaakt door externe oorzaken zoals ziektes, ofwel door intrinsieke oorzaken zoals de veroudering van cellen. Hierdoor moeten volgroeide weefsels zichzelf constant hernieuwen. Om voor homeostase te zorgen moet dit op een streng gereguleerde manier gebeuren. In dit proefschrift kijken we hoe dieren omgaan met een paar van dit soort uitdagingen. We doen dit aan de hand van twee modelsystemen, de worm *C. elegans* en de uit stamcellen afgeleide organoden.

In het eerste deel gebruiken we *C. elegans* om te bestuderen hoe hun ontwikkeling iedere keer op exact dezelfde manier gebeurt. We richten ons in het bijzonder op de vorming van de vulva van de wormen, een essentieel component voor hun voortplantingssysteem. Hier scheidt de zogenaamde ankercel een inductiesignaal af dat zes stamcelachtige cellen opdraagt om zich op een bepaalde manier te differentiren, afhankelijk van hoeveel signaal ze ontvangen. Stamcellen dichtbij de ankercel ontvangen een sterk signaal en worden hierdoor onderdeel van de vulva. Stamcellen verder weg ontvangen daarentegen een minder sterk signaal en worden daarom onderdeel van de huid. Verrassend genoeg bleken ankercellen in verschillende dieren een nogal verschillende plek in het lichaam te hebben, wat er dan ook voor zorgde dat de stamcellen varirende signaalsterktes ontvingen; desondanks ontwikkelden de meeste wormen een gelijksoortige vulva. Om uit te zoeken hoe zon onveranderlijk uitkomst toch kan ontstaan uit de zeer variabele beginsituaties hebben we experimentele analyse van de genexpressiedynamica gecombineerd met wiskundig modelleren. Onze resultaten wijzen uit dat voor een onveranderlijke vulva stamcellen niet alleen moeten luisteren naar het signaal van de ankercel, maar ook naar elkaar. Daarnaast moeten de stamcellen zich verplaatsen om zo een ideale plek te vinden ten opzichte van de ankercel. Tot slot suggereren onze resultaten een mechanisme waarop ook andere ontwikkelingsprocessen robuust kunnen verlopen, ondanks dat de positie van het noodzakelijke signaal variabel is.

In het tweede deel richten we ons op organoden: driedimensionale cel-structuren ontwikkeld uit stamcellen die vervolgens in vitro kunnen groeien. Deze structuren vertonen de essentile functies van het orgaan waar ze uit afgeleid zijn. In hoofdstuk 5 gebruiken we organoden uit de menselijke luchtweg om te bestuderen hoe het epitheel van de luchtweg reageert op een infectie van het zogeheten Respiratoir Syncytieel virus (RS-virus). Het RS-virus is een belangrijke oorzaak van luchtwegaandoeningen en bestaande vaccins en behandelingen schieten jammerlijk genoeg nog tekort. Hoe infecties van het RS-virus het epitheel benvloeden op celniveau wordt momenteel slecht begrepen. In dit proefschrift laten we zijn dat luchtwegorganoden een ideaal systeem vormen om deze vraag te beantwoorden. Uit versneld afgespeelde microscopievideos bleek dat organoden zeer beweeglijk werden na infectie door het RS-virus, waarbij enkele organoden een gecordineerde draaiende beweging maakten. Door het volgen van individuele cellen en door wiskundig modelleren tonen we aan dat die beweging veroorzaakt kan worden door een verhoging van de zogeheten celpersistentie (dit houdt in dat cellen meer geneigd zijn hun beweegrichting te behouden) en van de cel-celcommunicatie. Verder onderzoek in ons lab moet deze hypothese bevestigen en moet de essentile mechanismes die tot zulke beweeglijkheid leiden ontvouwen. De resultaten hier dragen hopelijk bij aan nieuwe inzichten over reactie van de luchtwegen op het RS-virus en aan een mogelijke behandeling.

In hoofdstuk 6 kijken we naar de effecten van de antivries-glycoeiwitten tijdens het bewaren van darmorganoden bij koude temperaturen. Deze eiwitten zijn door evolutie ontstaan in veel diersoorten die in koude en ijsachtige gebieden leven. De eiwitten voorkomen dat ijs gevormd wordt, wat ervoor zorgt dat de dieren niet doodvriezen bij temperaturen onder nul. Recent onderzoek heeft verrassend genoeg aangetoond dat de glycoeiwitten ook zoogdiercellen en organen kunnen beschermen wanneer deze op lage temperaturen worden opgeslagen, want ervoor zorgt dat ze voor langere tijd kunnen overleven. Echter, de mechanismes waarmee het glycoeiwit deze beschermende acties uitvoert zijn nog steeds onbekend. In onze studie hebben we gevonden dat darmorganoden voor een langere tijd kunnen worden opgeslagen onder hypothermische omstandigheden wanneer de glycoeiwitten aanwezig waren. Daarnaast vonden we dat de glycoeiwitten primair gelokaliseerd waren aan de randen van de cel, wat suggereert dat de eiwitten de membranen beschermen door middel van directe interacties. Ons onderzoek laat zien dat organoden een flexibel en voorheen ontoegankelijke manier bieden om de effecten van de glycoeiwitten te bestuderen in multicellulaire systemen, wat ons een stap dichtbij kan brengen bij het succesvol

bewaren van volledige organen in koude omstandigheden.

Tot slot onderzoeken we in hoofdstuk 7 de hernieuwing en de homeostase van volgroeid weefsel. Veel organen in volwassen dieren vervangen continu oude en beschadigde cellen door middel van voortdurend delende stamcellen. Deling en differentiatie van deze cellen moet echter streng gereguleerd worden: iedere onbalans hier leidt tot woekergroei of weefseldegeneratie. Echter, hoe dit wankele evenwicht in stand gehouden wordt in organen is nog altijd een fundamentele open vraag. Om dit te onderzoeken hebben we experimenten in muizendarmorganoden gecombineerd met het gebruik van rekenmodellen. Het maken van microscopievideos en het daarin volgen van cellen in groeiende organoden gaf ons een niet eerder vertoond beeld van de stamboomdynamica in het darmepitheel. Dit onderzoek liet ons zien dat organodengroei sterk gereguleerd is en dat celdelingen in crypten vooral symmetrisch zijn, wat wil zeggen dat zustercellen een gelijksoortig lot hebben. Een rekenmodel gaf een mogelijke uitleg voor deze hoge graad van symmetrie: het model liet zien dat een hoog aandeel symmetrische celdelingen resulteerde in de kleinst mogelijke fluctuatie in het aantal delende cellen. Hieruit volgt dat symmetrie bij celdelingen een mechanisme kan zijn om deze variabiliteit te minimaliseren en dus te zorgen voor homeostase. Onze resultaten suggereren een hiermee concreet mechanisme waarmee niet alleen het darmepitheel, maar ook andere weefsels het wankele evenwicht kunnen behouden tussen proliferatie en differentiatie.

Acknowledgments

I would like to start by thanking Jeroen for taking a chance on me, first as a master's student with little lab experience, and later as a PhD student who would start a completely new research direction in the group. Thanks for everything you have taught me over the past six years, both scientifically and personally. I truly admire your optimism, your passion for science and your outstanding ability to come up with random science facts that can relate to almost any topic of conversation. I will surely miss the many fun and sometimes weird conversations we had during lunch and group outings.

Next, I would like to thank Sander for the many useful discussions we had during our meetings. Thanks for always offering different and challenging perspectives that were certainly useful for thinking more critically about my projects.

I am also grateful to the committee members for the time and effort spent in evaluating this thesis.

Thanks to all the current and former members of the Quantitative Developmental Biology group. Yvonne, I am truly grateful that we ended up working so much together while going through the ups and downs of figuring out how to culture and do something useful with our organoids. I not only gained a great colleague, but also a good friend. Keep up your enthusiasm for trying out new things even when most of them keep failing. To the founding members of the group, Nicola, Simone and Kim, thanks for making my first years at AMOLF so much fun. To the new organoid people, Xuan and Rutger, thanks for all the valuable help you have provided towards finalizing my project. Take good care of the organoids for me. And Rutger, thanks again for the quick translation of my thesis's summary. Jason, I am glad we got to share an office for a few years; thanks for all the nice and useful conversations we had about life and about work. Joleen, I think most our conversations revolved around cats, how nice! Good luck with finishing you PhD, and greetings to your two furry friends. Olga, you are brave to embark into motherhood during the final stages of your PhD. I wish you all the best and I hope the happiness that little Ariadna brings you will be a source of inspiration and motivation for the hard work to come. Finally, a big thanks to the many the students who have joined the

group over the past years, you have all contributed towards keeping a fresh and dynamic atmosphere in the group.

Simone, too bad we became closer only towards the end of my time at AMOLF. Thanks for all the useful mom tips and advice, it's been great having someone to share both my baby joys and frustrations. Also, thanks for the fresh and pragmatic perspectives you offered during so many of our daily conversations.

I am grateful to the many people who have passed through office 1.39 over the past years. Special thanks to Hemant, Tom, Tjado, Niels, Theresa, Gopika, Galja, Jason, Rashel, and Gitta for keeping a sometimes calm, sometimes chaotic, but most importantly, always welcoming atmosphere.

Thanks to all the people who have in one way or another made my days at AMOLF happier and/or more productive: Marliek, Jeffrey, Jessica, Ana, Zubayda, Konrad, Bart, Yuval, Agata, Michele, Steffen, Mario, Marco, Vanda, Eleonora, Celine, Federica, Lucia, Harmen, Stephen, Mathijs, Rob, Juliette, Anders, Viktoria, Zuzana, Sebastian, Wiebe, Maga, Cristina, Norman, Joep, Marko, Henk-Jan, Jan Bonne, Hinco, Clyde...

Finally, a big thanks to my family. Mom, Dad, Adriana, Paco, Fernando and Bruno, you were the source of strength and motivation during this exhausting but rewarding roller-coaster ride.

Curriculum Vitae

Guizela Huelsz Prince

28-01-1988   Born in Mexico City, Mexico

Education

2007–2012   BSc Physics
                National Autonomous University of Mexico
                Mexico

2012–2014   MSc Physics of Life and Health
                University of Amsterdam
                The Netherlands

2014–2019   PhD Research
                AMOLF
                The Netherlands

List of Publications

7. **G Huelsz-Prince**, YJ Goos, RNU Kok, X Zheng, SJ Tans, and JS van Zon. *Single-cell dynamics of growth and homeostasis in intestinal organoids.* In preparation.

6. **G Huelsz-Prince**, AL de Vries, HJ Bakker, JS van Zon, K Meister. *Effect of antifreeze glycoproteins on organoid survival during and after hypothermic storage.* Biomolecules. 9(3),110, 2019

5. L Hartl, **G Huelsz-Prince**, JS van Zon, SJ Tans. *Apical constriction is necessary for crypt formation in small intestinal organoids.* Developmental Biology. pii: S0012-1606(18)30474-3, 2019

4. N Sachs, DD Zomer-van Ommen, A Papaspyropoulos, I Heo, L Bottinger, D Klay, F Weeber, **G Huelsz-Prince**, N Iakobachvili, MC Viveen, A Lyubimova, L Teeven, S Derakhshan, J Korving, H Begthel, K Kumawat, E Ramos, MFM van Oosterhout, EP Olimpio, J de Ligt, KK Dijkstra, EF Smit, M van der Linden, EE Voest, CHM van Moorsel, CK van der Ent, E Cuppen, A van Oudenaarden, FE Coenjaerts, L Meyaard, LJ Bont, PJ Peters, SJ Tans, JS van Zon, SF Boj, RG Vries, JM Beekman, H Clevers (2019) *Long-term expanding human airway organoids for disease modeling.* EMBO J. 38(4). pii: e100300, 2019

3. **G Huelsz-Prince**, JS van Zon. *Canalization of C. elegans vulva induction against anatomical variability.* Cell systems 4 (2), 219-230. e6, 2017

2. JS van Zon, S Kienle, **G Huelsz-Prince**, M Barkoulas, A van Oudenaarden. *Cells change their sensitivity to an EGF morphogen gradient to control EGF-induced gene expression.* Nature Communications. 11;6:7053, 2015

1. **G Huelsz-Prince**, AM Belkin, E vanBavel, ENTP Bakker. *Activation of extracellular transglutaminase 2 by mechanical force in the arterial wall.* Journal of Vascular Research. 2013;50(5):383-95, 2013